SYNTHESIS, STRUCTURE AND MAGNETIC PROPERTIES OF

LANTHANIDE CLUSTER COMPOUNDS

A Dissertation

by

LUCAS EDWARD SWEET

Submitted to the Office of Graduate Studies of
Texas A&M University
in partial fulfillment of the requirements for the degree of

DOCTOR OF PHILOSOPHY

December 2008

Major Subject: Chemistry

SYNTHESIS, STRUCTURE AND MAGNETIC PROPERTIES OF

LANTHANIDE CLUSTER COMPOUNDS

A Dissertation

by

LUCAS EDWARD SWEET

Submitted to the Office of Graduate Studies of
Texas A&M University
in partial fulfillment of the requirements for the degree of

DOCTOR OF PHILOSOPHY

Approved by:

Chair of Committee,	Timothy Hughbanks
Committee Members,	Kim Dunbar
	Joe Ross
	Abraham Clearfield
Head of Department,	David Russell

December 2008

Major Subject: Chemistry

ABSTRACT

Synthesis, Structure and Magnetic Properties of Lanthanide Cluster Compounds.

(December 2008)

Lucas Edward Sweet, B.A., Lake Forest College

Chair of Advisory Committee: Dr. Timothy Hughbanks

This dissertation focuses on the exploratory synthesis of compounds that contain R_6ZI_{12} (R= Ce, Gd, Er; Z=Mn, Fe, Co, C_2) clusters with the goal of finding magnetically interesting compounds. Several new compounds were made via high temperature, solid state methods and structurally characterized using x-ray diffraction. Compounds that contain isolated clusters were studied in order to understand the magnetic coupling between lanthanide atoms.

The exploration of transition metal centered clusters resulted in the discovery of two new structure types, $CsR(R_6CoI_{12})_2$ (R=Gd and Er) and $(CeI)_{0.26}(Ce_6MnI_9)_2$. The x-ray crystal structure of $CsEr(Er_6CoI_{12})_2$ was solved in the $Pa\overline{3}$ space group with the cell length 18.063(2) Å at 250K (Z = 4, R_1 [I>2σ(I)] = 0.0459). $(CeI)_{0.26}(Ce_6MnI_9)_2$ was made by combining KI, CeI_3, MnI_2 and Ce metal and heating to 850°C for 500 hrs. The single crystal x-ray structure for $(CeI)_{0.26}(Ce_6MnI_9)_2$ was solved in the trigonal, $P\overline{3}$ space group with lattice parameters of a = 11.695(1) Å c = 10.8591(2) Å (Z = 2, R_1 [I>2σ(I)] = 0.0895).

The magnetic susceptibilities of hexanuclear gadolinium clusters in the compounds $Gd(Gd_6ZI_{12})$ (Z = Co, Fe or Mn), $Ca_xGd_{1-x}(Gd_6MnI_{12})$ and $CsGd(Gd_6CoI_{12})_2$ are reported. The single-crystal structure of $Gd(Gd_6CoI_{12})$ and $Ca_xGd_{1-x}(Gd_6MnI_{12})$ are reported here as well. The compound with a closed shell of cluster bonding electrons,

$Gd(Gd_6CoI_{12})$, exhibits the effects of antiferromagnetic coupling over the entire range of temperatures measured (4 - 300 K). Clusters with unpaired, delocalized cluster bonding electrons (CBEs) exhibit enhanced susceptibilities consistent with strong ferromagnetic coupling, except at lower temperatures (less than 30 K) where intercluster antiferromagnetic coupling suppresses the susceptibilities.

Four new compounds containing Gd_6C_2 clusters have been found: $Gd_6C_2I_{11}$, $Gd(Gd_6C_2I_{12})$, $CsGd(Gd_6C_2I_{12})_2$ and $Cs(Gd_6C_2I_{12})$. $Gd_6C_2I_{11}$ and $Cs(Gd_6C_2I_{12})$ crystallized in the $P\bar{1}$ space group while $Gd(Gd_6C_2I_{12})$ and $CsGd(Gd_6C_2I_{12})_2$ crystallized in the $R\bar{3}$ and $Pa\bar{3}$ space groups respectively. The magnetic susceptibility data for $Cs(Gd_6C_2I_{12})$ indicate strong intracluster ferromagnetic coupling, but antiferromagnetic coupling suppresses the susceptibility below 150 K. DFT calculations on $CsGd_6C_2I_{12}$ and molecular models indicate that the magnetic coupling between the basal Gd atoms is stronger than the magnetic coupling involving the axial Gd atoms in the distorted clusters.

ACKNOWLEDGEMENTS

NOMENCLATURE

CBE	Cluster bonding electron
DFT	Density functional theory
DOS	Density of states
EH	Extended Hückel
HOMO	Highest-occupied molecular orbital
LUMO	Lowest-unoccupied molecular orbital
R	Rare earth
SMM	Single molecule magnet
SOMO	Singly-occupied molecular orbital

TABLE OF CONTENTS

LIST OF FIGURES

FIGURE   Page

LIST OF TABLES

CHAPTER I

INTRODUCTION[*]

The study of high spin molecules, especially those which behave as single molecule magnets, started about 15 years ago and continues to be a hot topic today. [1-12] This field became an intense interest with the discovery of the magnetic properties of $Mn_{12}O_{12}(CH_3COO)_{16}(H_2O)_4 \cdot CH_3COOH \cdot 3H_2O$.[1] Due to magnetic anisotropy, this molecule has two energetically favored spin states, $M_s=10$ and $M_s=-10$, and there is an energetic barrier to interconverting them. This energy barrier to spin flipping is often described using a double well potential diagram shown in Figure 1.1. The idea is that in order for a molecule to convert from $M_s=10$ to $M_s=-10$ there must be enough energy to transverse though each spin state. The magnitude of the energy barrier to interconversion is equal to DS^2 where D is the zero field splitting, a measure of magnetic anisotropy, and S is the net spin for the cluster. Much effort has been expended trying to find molecules with large values of S and positive D values in order to achieve a high "blocking temperature" (the temperature below which thermally activated spin flipping is slow). In practice, the observed barriers to spin flipping are less than DS^2 due to other mechanisms that don't involve traversing all of the higher energy spin states.
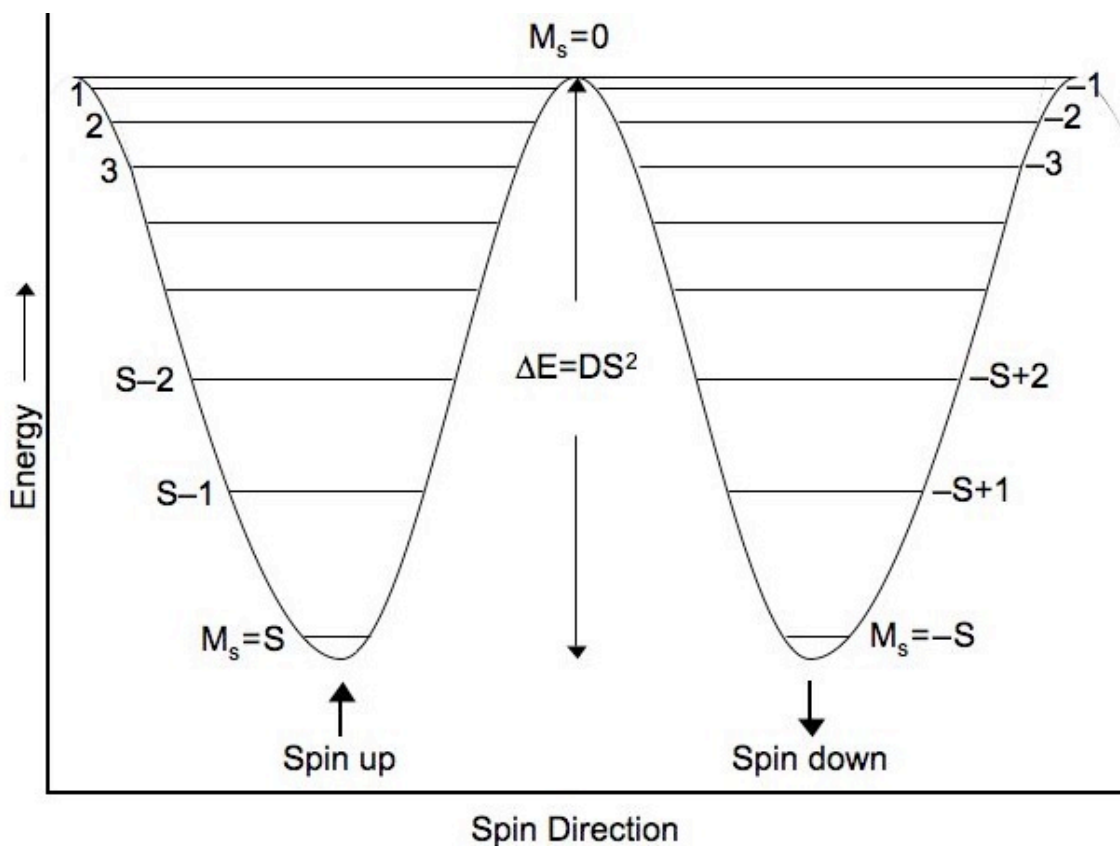
Figure 1.1. The double well potential demonstrates the energy barrier to changing S states.

Ishikawa et. al. have shown that lanthanide based molecules can exhibit marked SMM behavior the origin of which is quite different than in transition metal molecules.[13-20] This group has studied $[(PC)_2Ln]^-$ TBA^+ (PC = phthalocyaninato, Ln = lanthanide and $TBA^+=N(C_4H_9)_4^+$) complexes, depicted in Figure 1.2. Since the 4f orbitals of the lanthanides are core-like, the relative magnitude of effects that influence their electronic structure and magnetism is different than for the d orbitals of transition metals. Electron-electron repulsions and spin-orbit coupling are larger than crystal field splitting for the 4f electrons. The double well potential of incrementally laddered spin only states does not apply to these lanthanide complexes. Nevertheless, the $[(PC)_2Ln]^-$

complexes do exhibit SMM behavior, i.e., there *is* a barrier to magnetic moment inversion. The energy difference between the ground state and the first excited states is an order of magnitude larger than the difference between the SMM spin states of transition metal clusters. As with transition metal SMMs, there are mechanisms in which the conversion between degenerate spin states occurs through an alternant path, which is lower in energy than incremental m_J steps, for lanthanide SMMs. The largest effective barrier to spin inversion for the lanthanide complex $(PC)_2Tb$ was $550cm^{-1}$.[20] The current record holder for the largest effective energy barrier for spin inversion for transition metal based SMMs is the $[Mn^{III}_6O_2(Et\text{-}sao)_6(O_2CPh(Me)_2)_2(EtOH)_6]$ complex with a barrier to spin inversion of $60 \ cm^{-1}$.[21] Based on these findings, lanthanide cluster molecules appear to be promising for magnets with high blocking temperatures, but there are very few examples.
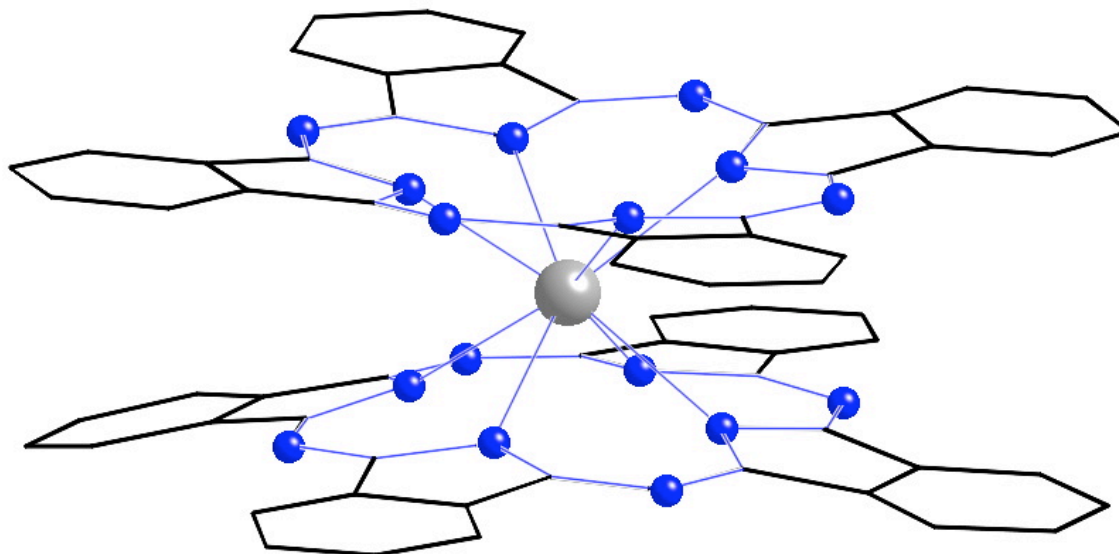
Figure 1.2. Structure of a $Ln(PC)_2$ complex (Ln and N shown as large gray and small blue spheres respectively).[22]

We have posed the question: if the moments of several lanthanide centers can be ferromagnetically coupled, might we achieve an increase the magnitude of the energy barrier to spin inversion? Unfortunately, when lanthanides are present in compounds they are usually in a 3+ oxidation state and have no appreciable electronic communication with surrounding atoms. The 4f orbitals are contracted (see Figure 1.3) and are not used in bonding. Since there is no bonding involving the 4f orbitals, compounds that only contain lanthanides in 3+ oxidation states are not beneficial to our goal of finding high spin clusters.

Rules for coupling the moments of gadolinium atoms are being developed in our group.[23-26] Atomic spectra for Gd ($[Xe]4f^7 5d^1 6s^2$)[27] show a large exchange energy difference between the states in which the 5d electron is aligned with (^9D) and against (^7D) the seven electrons in the 4f orbitals, as indicated in Figure 1.4. This fact leads one to conclude that in order to couple the spins of the electrons in the 4f orbitals of neighboring Gd atoms, a molecule must contain Gd aotms that have electrons in its bonding d orbitals. It follows that we should focus on compounds containing lanthanides in reduced oxidation state than 3+. Since the 4f orbitals of Gd are half filled there is no spin orbit coupling. With the absence of complexities that can arise from spin orbit coupling the spin-spin coupling in Gd clusters can be observed more clearly, of course this puts aside for the time being a study of effects due to on-site magnetic anisotropy since there is no orbital contribution to Gd magnetic moments.
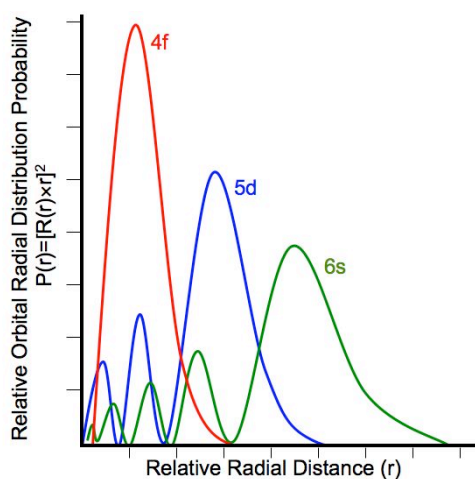
Figure 1.3. The orbital radial distribution of hydrogenic wave functions, as a function of distance from the nucleus.
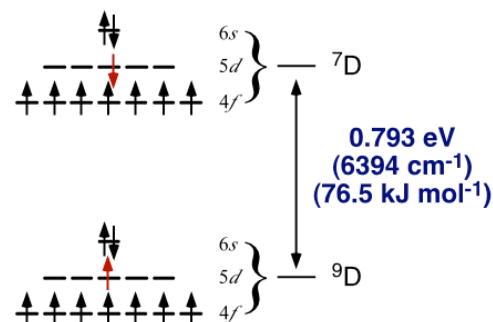
Figure 1.4. The relative energies of having the electron in the 5d orbitals spin aligned or apposed with the spins of the electrons in the 4f orbitals for a Gd atom.

The focus of this project was to study the magnetic properties of rare-earth cluster compounds, which contain reduced cluster units similar to that shown in Figure 1.5. There are several different structure types known that contain R_6 clusters and in all of them, the clusters are linked into network solids (see Tables on pg 7 and 11). The structure type with the most-isolated clusters that can be made in quantitative yields with Gd, and consequently the starting point for the magnetic studies, was $Gd(Gd_6MI_{12})$ (M = Mn, Fe, Co). The clusters are cross-linked such that half the edge-bridging iodine atoms of one cluster serve as axial capping ligands on neighboring clusters. There is an additional Gd^{3+} ion that resides in a trigonal antiprismatic site formed by edge bridging iodine atoms not used in cross linking the cluster network.

Schäfer and Schnering notation[28] is used to indicate how the clusters are cross linked by bridging iodine atoms. The symbol I^{i-a} (i stands for inner (edge bridged) and a stands for ausser (axial)) indicates that the edge bridging iodine atom on the cluster being described is axial on the neighboring cluster. To represent the opposite scenario,

the symbol I^{a-i} is used to indicate the axial iodine atom on the cluster being described is an inner (edge bridged) iodine atom on the neighboring cluster. For iodine atoms that do not participate in intercluster bridging the symbols I^i and I^a are used. These labels are applied to the structure $Gd(Gd_6CoI_{12})$ in Figure 1.5.
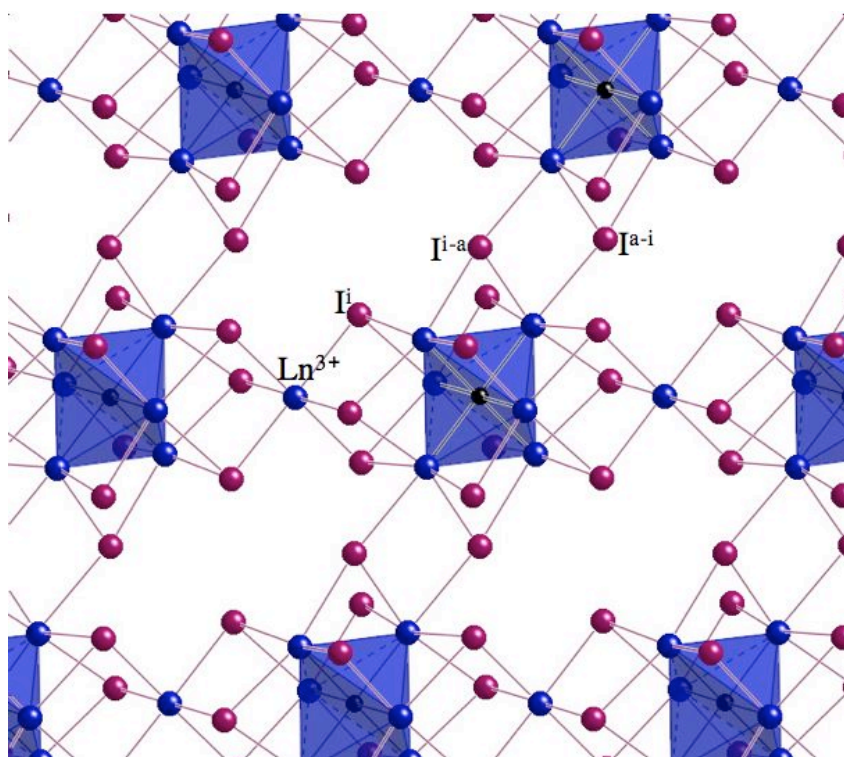
Figure 1.5. Depicted is the 110 plane of $Ln[(Ln_6M)I_{12}]$ (Ln = Gd and Er; M = Mn, Fe and Co). The Gd_6M units are depicted as the blue octahedra. The purple, blue and black spheres represent I, Ln and M respectively. Some of the iodine atoms are labeled with Schäfer and Schnering notation[28] to indicated the connectivity with respect to the central cluster.

We have embarked on a search for new compounds containing discrete lanthanide clusters, spurred by our predictions concerning the effect that *d–f* exchange interactions have on the magnetic properties of these clusters.[26] However, synthetic

challenges must be overcome before we can formulate trends in the properties of these compounds; we currently lack sufficient synthetic control to exploit these compounds' promising magnetic properties. The approach taken here has been to modify reaction conditions for making known compounds in order to expand our inventory of cluster compounds with known (or new) structure types. The emphasis was placed on finding conditions and compositions that may yield discrete clusters so that structural isolation will enable us to study the magnetic properties of isolated polynuclear lanthanide clusters. Prior to this project there were 14 known structure types for lanthanide iodide compounds that contain uncondensed Ln_6 clusters. These structure types are listed in Table 1.1.

Table 1.1. Known structure types for lanthanide iodide compounds that contain R_6 clusters

Compound Formula or General Formula	Schäfer and Schnering Notation[28]	Reference
$R_{12}Z_2I_{17}$ (R=La, Ce, Pr; Z=Fe, Mn)	$(R_6M)I^{i-i}_{7/2}I^{a-i}_{4/2}I^{i-a}_{4/2}I^{a-a-i}_{2/3}I^{i-a-a}_{1/3}$	29,30
R_6ZI_{10}	$(R_6Z)I^i_2I^{i-i}_{4/2}I^{i-a}_{6/2}I^{a-i}_{6/2}$	31-33
$R_6C_2I_{10}$ (R=La, Ce)	$(R_6C_2)I^i_2I^{i-i}_{4/2}I^{i-a}_{6/2}I^{a-i}_{6/2}$	34
$A(R_6ZI_{10})$	$A(R_6Z)I^i_2I^{i-i}_{4/2}I^{i-a}_{6/2}I^{a-i}_{6/2}$	35
$Sc_6C_2I_{11}$	$(Sc_6C_2)I^i_4I^{i-i}_{2/2}I^{i-a}_{6/2}I^{a-i}_{6/2}$	36
$A_xR_{1-x}(R_6ZI_{12})$	$A_xR_{1-x}(R_6Z)I^i_6I^{i-a}_{6/2}I^{a-i}_{6/2}$	37-47
$Rb(Pr_6C_2I_{12})$	$Rb(Pr_6C_2)I^i_6I^{i-a}_{6/2}I^{a-i}_{6/2}$	48
$Cs(Er_6CI_{12})$	$Cs(Er_6C)I^i_6I^{i-a}_{6/2}I^{a-i}_{6/2}$	49,50
$K_2(La_6OsI_{12})$	$K_2(La_6Os)I^i_6I^{i-a}_{6/2}I^{a-i}_{6/2}$	51
$Cs_2(Pr_6C_2I_{12})$	$Cs_2(Pr_6C_2)I^i_6I^{i-a}_{6/2}I^{a-i}_{6/2}$	52
$Cs_4(R_6ZI_{13})$ (R=Ce, Pr; Z=Co, Os)	$Cs_4(R_6Z)I^i_8I^{i-a}_{4/2}I^{a-i}_{4/2}I^{a-a}_{2/2}$	53
$Cs_4(Pr_6C_2I_{13})$	$Cs_4(Pr_6C_2)I^i_8I^{i-a}_{4/2}I^{a-i}_{4/2}I^{a-a}_{2/2}$	54
$\beta-K_4La_6OsI_{14}$	$(K_4I)(La_6Os)I^i_8I^{i-a}_{4/2}I^{a-i}_{4/2}I^{a-a}_{2/2}$	55
$\alpha-K_4(La_6OsI_{14})$	$K_4[La_6Os]I^i_8I^{i-a}_{4/2}I^{a-i}_{4/2}I^a_2$	56

General formulas are used here when more than one analog has been reported. A= alkali or alkaline earth element, R = rare earth element, Z=transition metal or main group element excluding C_2.

The approach to finding new clusters has been to vary stoichiometries of alkali and or alkali earth iodides in reactions as outlined below.

$$\text{QI or } Q'I_2 + LnI_3 + MI_2 + Ln \xrightarrow[850°C]{16 \text{ days}} Q_wQ'_xLn_y[(Ln_6M)I_{12+z}]$$
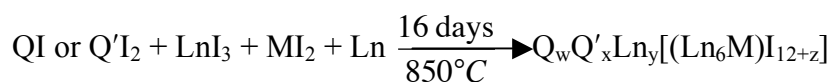
Q and Q′ = alkali and alkaline earth metals

The idea is that large cations like Cs will "prop open" the structures and increase the I:Gd ratio of the products so that the anionic clusters are more structurally isolated. An alternative approach was to attempt to incorporate a larger number of smaller cations, which might result in more isolated clusters. Figure 1.6 illustrates how increasing the I:Gd ratio will decrease the number of shared iodine atoms and therefore reduce the amount of cross linking between the clusters. The clusters that are less cross linked in extended network compounds should also be more amenable to subsequent excision into molecular units via dissolution.

A factor kept in mind when choosing ratios of reactants for reactions intended to target new transition metal centered cluster compounds is the electron count on the target compound. The known compounds that contain transition metal centered R_6 clusters have 15-18 electrons in cluster bonding orbitals. The details of the cluster electronic structure will be discussed in Chapter IV. Typically loading ratios of reactants were chosen to target compounds that would contain clusters with 15-18 electrons in cluster bonding orbitals.

6-12
Sr(La$_6$OsI$_{12}$)

6-14
α-K$_4$(Pr$_6$OsI$_{14}$)

6-18
CsLu(Lu$_6$CCl$_{18}$)
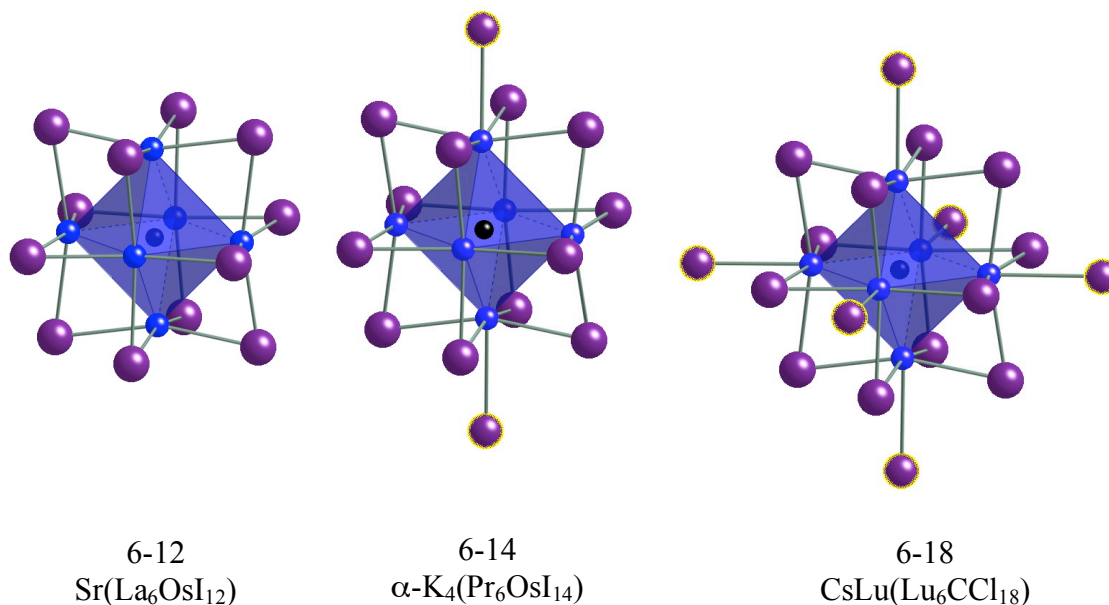
Figure 1.6. The cluster units of examples of structure types that have a lanthanide to iodide rations of 6:12, 6:14 and 6:18 are shown. The iodine atoms that are highlighted in yellow are I^a and therefore not involved in intercluster bridging.

Another important factor for making these clusters better candidates for subsequent excision is to increase the lanthanide to axial iodide bond distance. Zirconium cluster compounds, which have similar structure types to the ones being discussed here, have been observed to be more stable after being excised when a smaller interstitial is used.[57-59] Most of the structure types described here can be viewed as a cubic closest packing of iodine atoms but some of the iodide atoms are replaced with a Gd$_6$M cluster. The radius of M affects the size of the octahedral cage but the iodine spacing remains nearly the same as it would if the structure was just a cubic close packing of iodine. By having a smaller Gd$_6$ cage the axial Gd–I^a distances are lengthened and possibly more susceptible to breaking by dissolution. The cage to halide size ratio is indicated by the ∠I^i–Gd–I^i bond angle. The more acute this bond angle is, the larger the halide to metal cage size ratio is. The interatomic metrics that are

compared to indicate the contraction of the Gd_6 cages are, the I^i–Gd–I^i angle, the Gd–M distance and the Gd–I^a distance. These distances and angles are shown in Figure 1.7.
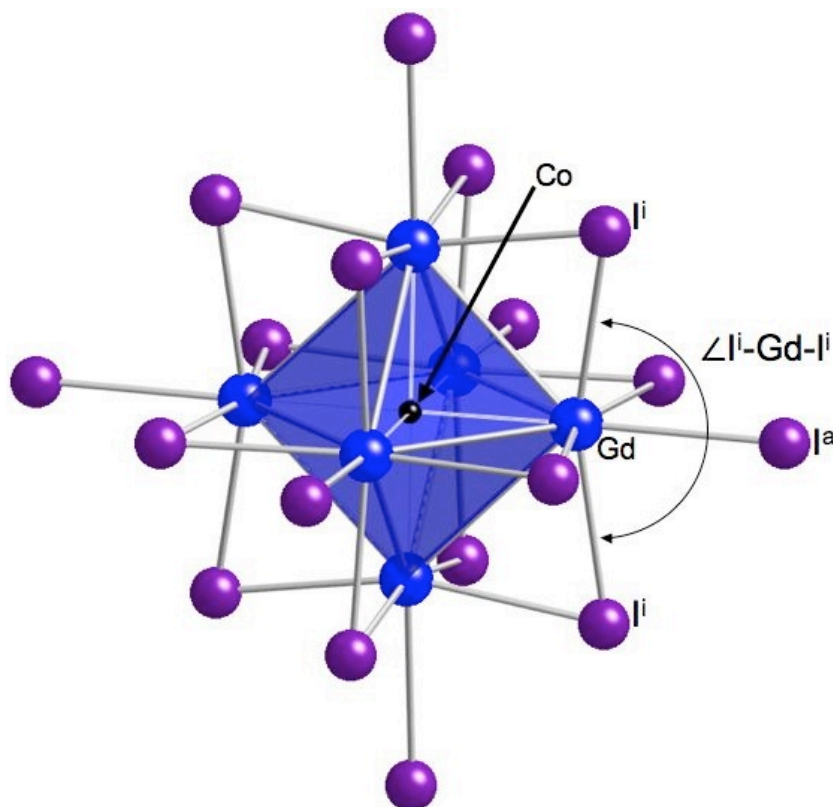
Figure 1.7. A single cluster of $Gd(Gd_6CoI_{12})$ is shown with labels to illustrate the interatomic metrics of interest (I^i–Gd–I^i angle, Gd–Co distance, and Gd–I^a).

The trend of stable, excised, zirconium clusters provided our motivation for exploring the carbon-centered gadolinium cluster compounds. The only compound that contains isolated Gd_6C clusters mentioned in the literature is $Gd(Gd_6CI_{12})$. There have been scattered references that mention the existence of $Gd(Gd_6CI_{12})$,[45,60] however, this compound is usually sited as being "unpublished results."[61] While there is little evidence of isolated Gd_6C clusters, there have been several carbon-centered clusters of other rare earths (see Table 1.2).

Table 1.2. Known compounds that contain isolated carbon centered Ln_6 clusters

Compound Formula or General Formula	Schäfer and Schnering notation[28]	Reference
$Cs_2Lu(Lu_6CCl_{18})$	$Cs_2Lu(Lu_6C)Cl^i_{12}Cl^a_6$	49
$Cs_4(Sc_6CCl_{13})$	$Cs_4(Sc_6C)Cl^i_8Cl^{i\text{-}a}_{4/2}Cl^{a\text{-}i}_{4/2}Cl^{a\text{-}a}_{2/2}$	54
$Cs_4(Pr_6C_2I_{13})$	$Cs_4(Pr_6C_2)I^i_8I^{i\text{-}a}_{4/2}I^{a\text{-}i}_{4/2}I^{a\text{-}a}_{2/2}$	54
$Cs_2(Pr_6C_2I_{12})$	$Cs_2(Pr_6C_2)I^i_6I^{i\text{-}a}_{6/2}I^{a\text{-}i}_{6/2}$	52
$Rb(Pr_6C_2I_{12})$	$Rb(Pr_6C_2)I^i_6I^{i\text{-}a}_{6/2}I^{a\text{-}i}_{6/2}$	48
$Cs(Er_6CI_{12})$	$Cs(Er_6C)I^i_6I^{i\text{-}a}_{6/2}I^{a\text{-}i}_{6/2}$	49,50
$R(R_6CI_{12})$ (R=Sc, La, Ce, Pr, Gd, Tb, Er)	$R(R_6C)I^i_6I^{i\text{-}a}_{6/2}I^{a\text{-}i}_{6/2}$	45,46
$Sc_6C_2I_{11}$	$(Sc_6C_2)I^i_4I^{i\text{-}i}_{2/2}I^{i\text{-}a}_{6/2}I^{a\text{-}i}_{6/2}$	36
$R_6C_2I_{10}$ (R=La, Ce)	$(La_6C_2)I^i_2I^{i\text{-}i}_{4/2}I^{i\text{-}a}_{6/2}I^{a\text{-}i}_{6/2}$	34

Unlike the transition metal centered clusters, the carbon centered clusters compounds also exist structure types that contain bioctahedral cluster shape (shown in Figure 1.8). The compounds that contain bioctahedral clusters are primarily chlorides and bromides. The intercluster connectivity of these bioctahedral clusters is similar to the inner-ausser halide linkages of the single octahedral cluster compounds. Typically when the lanthanide atoms in a bioctahedral cluster are in a formal oxidation state of less than 3+, the Ln-Ln distance between the two atoms that form the shared edge is shorter than the other Ln-Ln distances. Do to this apparent localization of electrons the bioctahedral clusters are less promising candidates for coupling the spins of the electrons in the 4f orbitals via exchange interactions with the electrons in more delocalized Ln-Ln bonding orbitals.
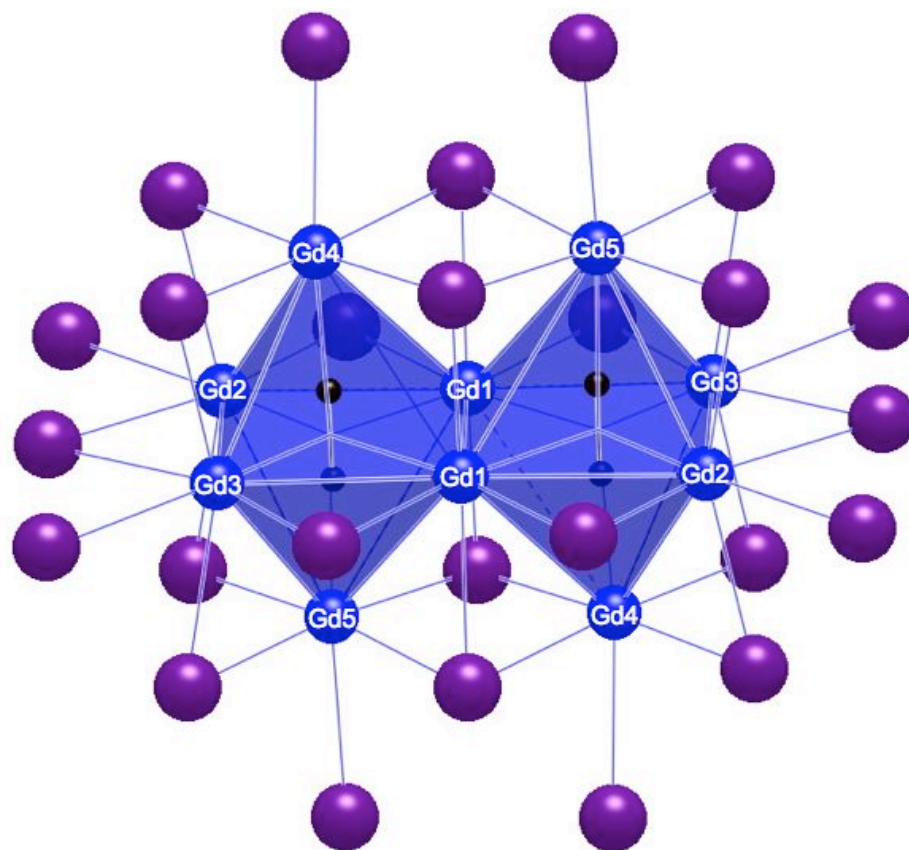
Figure 1.8. Bioctaherdral cluster that is part of the extended network of $Cs(Gd_{10}C_4I_{18})$ (Gd1-Gd1 distance is 3.2509(7), Gd2-Gd3 distance is 3.5171(5) Å).

A very narrow search for new carbon centered Gd_6 clusters was conducted. The goal was to try to make $Gd(Gd_6CI_{12})$ and a Gd analogue of $Cs(Er_6CI_{12})$. While the search for carbon centered compounds was more fruitful than the transition metal centered cluster compound search, the number of structural characterization difficulties was greater.

CHAPTER II

EXPERIMENTAL

Materials

A few different grades of the elemental lanthanides were used in various stages of our synthetic investigations. There were three sources of Gd metal. Gd metal from Research Chemicals was only used for making GdI_3. Gd metal from Stanford Materials (99.95% metals basis) was used for making GdI_3 and for most of the exploratory synthesis. For investigations of compounds for which reaction conditions have been established that produce quantitative yields (i.e. those for which magnetic susceptibility measurements were desired), Gd metal from Ames Lab (99.999% including all elements) was used. Ce metal from Research Chemicals was used to make CeI_3. Ce metal from Stanford Materials (99.9% REM) was used to run reactions targeted to make cluster compounds. Er metal from Stanford Materials (99.9%, metals basis) was the only source of Er used in the reactions reported here. The Gd, Er, Ce metals from Stanford Materials and the Gd metal from Ames Lab were supplied in the form of ingots. The ingots were drilled in a N_2 filled dry box to get turnings, which were used in reactions. A separate tungsten carbide drill bit was used for each metal.

The rare earth triiodides were prepared by oxidation of the rare earth elements with HgI_2, as described in the literature,[62] and purified in at least three vacuum sublimations.[63] The HgI_2 (Strem 98+%, Fisher Scientific 99.5%) was used as received. A two segment borosilicate reaction tube was made with a diameter restricted region between the two segments (shown in Figure 2.1 A). The first segment was typically 7cm long with a 4 cm OD and was closed at one end. The other end of the first segment was narrowed and attached to a 2 cm long piece of 1 cm OD thick wall borosilicate tube.

The second segment was 5 cm long with a 2.5cm OD. Both ends of the second segment were narrowed with one end attached to the thick wall tube that is linked to the first segment and the other end is attached to a ball joint. The thick wall tube that linked the two segments was bent about 30º from being straight. The HgI_2 and Ln metal were loaded into the reaction tube so that they sit in the first segment. The reactants are loaded stoichiometrically according to the following reaction.

$$2GdI_3 + 3HgI_2 \rightarrow 2GdI_3 + 3Hg$$
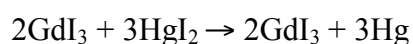
The procedure reported in the literature recommended the use of 20% excess HgI_2 but it was found that when loading to make 20g of product or more, the excess HgI_2 was not necessary. The reaction tube was heated in an electric tube furnace to 350º C and soaked at that temperature for two days. A reaction tube loaded to make CeI_3 should not be heated any faster than 1º C/min to avoid a potential explosion. After the two day soak period, the second segment was pulled outside of the furnace. The first segment remained in the furnace and was parallel to the bench top and the second segment pointed down towards the bench top. The first segment was left in the furnace for another two days. By pulling the second segment out, Hg and unreacted HgI_2 collect in the cooler second segment. Once in the glove box the two segments were separated and the product was collected. The crude LnI_3 product was then sublimed under dynamic vacuum three times. The sublimation setup is shown in Figure 2.1.
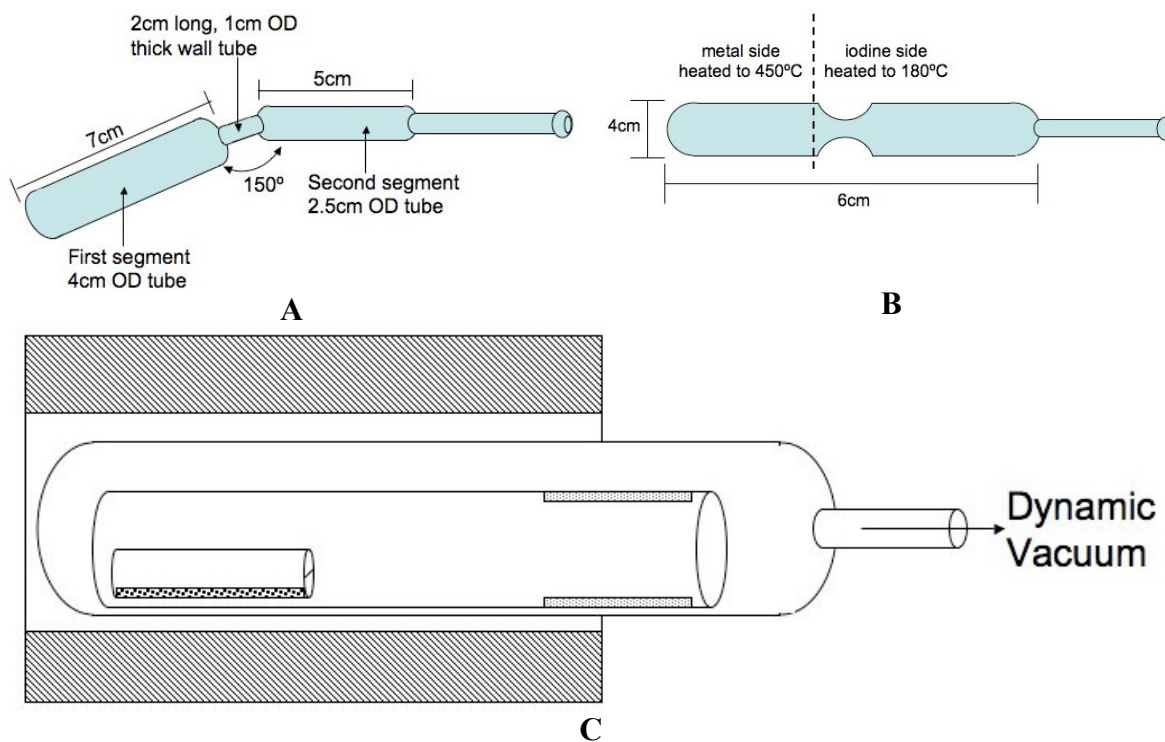
Figure 2.1. **A** shows a schematic drawing of a reaction tube used in the synthesis of RI_3. **B** shows a schematic drawing of a reaction tube used in the synthesis of MI_2. **C** shows a schematic drawing of a sublimation apparatus.

The transition metal iodides were made by heating the elements together in a sealed two segment reaction tube (shown in Figure 2.1 B). The transition metal powders Co (Alfa Aesar 99.998%), Fe (Alfa Aesar 99.998%), and Mn (Morton Thiokol 99%) in addition to the iodine (J. T. Baker 99.9%) were used as received. The reaction tubes used were about 6 cm long with a 4 cm OD and had a diameter restriction to about 0.5 cm ID in the center of the tube thus creating the two segments. The metal and iodine were loaded into the tube so that they rest at the back end of the tube. The tube was then sealed off under vacuum. The back end of the tube was then placed in an electric furnace and heated to 80°C for about 12 hours, causing the iodine to sublime to the opposite end of the tube. The segment with the metal powder is placed in one furnace, which is heated to 450° C and the segment with iodine is placed in a separate furnace,

which is heated to 180º C. The reaction vessel is typically heated at this temperature for 20 days. The MI_2 will condense just before the diameter restricted region of the tube, which is located at the interface between the two furnaces. If the metal powder sits in a pool of liquid iodine during the reaction the surface of the metal gets blocked and the formation of MI_2 stops. This is why the iodine is initially separated from the metal powder. The diameter restriction in the tube also prevents the liquid iodine from rolling into the metal segment. The MI_2, which is hygroscopic, is collected in a dry box and then sublimed. MnI_2 and FeI_2 can be sublimed in the same manner as RI_3, but CoI_2 needs be sublimed in a static vacuum. The sublimed MI_2 was stored in sealed evacuated glass ampoules until use.

CsI (Alfa Aesar 99%) and KI (Fisher Scientific 99.95%) were sublimed once and then stored in sealed, evacuated ampoules before being used in reactions. The sublimation apparatus used for the alkali halides was similar to the one used to sublime RI_3. Graphitic carbon (Alfa Aesar 99.9%) was heated under vacuum at 900ºC for 24 hours and then stored in a sealed, evacuated ampoule prior to use.

Synthetic Techniques

Aside from the initial loading of iodine and transition metal powder to make MI_2, the handling of all other materials was done in a N_2 filled glove box, vacuum line or evacuated glass ampoules in order to avoid contact with air and moisture. Nb tubes were used as containers for the reactions carried out to make reduced Ln compounds. The Nb tubes were cut into pieces that were approximately 6 cm long. The Nb tubes were washed with soap and water, rinsed, then etched with an acid solution consisting of 55% H_2SO_4 (16M), 30% HNO_3 (18 M) and 15% HF (24 M) (by volume). One end of the tubes were crimped and then welded with an arc welder under argon (~500 Torr). After

the Nb tubes were loaded with reactants, the other end was crimped and welded. The Nb tubes are then sealed in evacuated fused silica ampoules. The ampoules are then placed in an electric tube furnace and heated to 800-900º C for 15-20 days.

Powder X-Ray Diffraction

Powder x-ray diffraction patterns were collected for each product for phase identification. A Bruker AXS D8 powder x-ray diffractometer equipped with graphite monochromated Cu K_α (λ=1.5418 Å) x-ray source was used with an airtight sample holder in order to obtain powder diffraction patterns of the samples. Three types of hermetically sealed sample holders were used (Figure 2.2). Holder C in Figure 2.2 remained air free during the data acquisition time (typically 12 hours) most consistently and was therefore most favorable as the project proceeded. Holder A was primarily used in the acquisition of diffraction patterns of compounds of the Gd_7MI_{12} (M = Mn, Fe, Co) type. Sample holder B was used when $CsR(R_6CoI_{12})_2$ (R = Gd or Er) and $(CeI)_{0.26}(Ce_6MnI_9)$ were discovered. Sample holder C was used when the carbon centered Gd cluster compounds were discovered. Each of these sample holders require about 100mg of sample. 15 mg of Si powder is added to the sample powder for an internal standard. A quick scan from 20-40º 2θ and a scan rate of 10º/min is acquired first for a sample. The peak height and width are evaluated from the diffraction pattern collected from the quick scan to get an idea of the step size and exposure time that will result in the best pattern. Highly crystalline samples of these cluster compounds typically require a scan step size of 0.02º and an exposure time of 10 seconds per step. Powder Cell[64] or Crystal Diffract[65] software was used to compare the diffraction patterns of the samples with those of known phases. Powder patterns of known phases were

calculated with input of a cif file obtained from the Inorganic Crystal Structure Database[66] or unit cell parameters and atom coordinates that were manually entered.

| A | B | C |
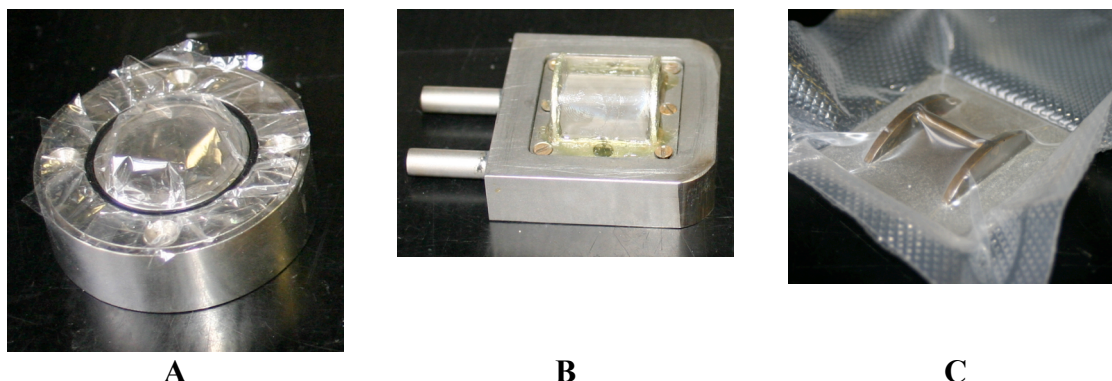
Figure 2.2. The first sample holder for air sensitive samples (**A**) was designed by Dr. Nattamai Bhuvanesh and uses an o-ring over 0.6 μm thick Polyethylene terephthalate (PET) film to seal the window. The second design is shown in **B** has a PET film window that is glued onto stainless steal semicircles. The third design is shown in **C** and is sealed in a FoodSaver[®] vacuum bag using a FoodSaver[®] vacuum sealer.

Single Crystal X-Ray Diffraction

Structural information was collected using single crystal x-ray diffraction. Since the products were air sensitive, crystals of appropriate size and shape were picked out of the products with the aid of a microscope in a dry box. Crystals were mounted on nylon loops attached to a metal pins, which could be attached to a goniometer head. Once a crystal was mounted on a nylon loop using Apeazon® N grease the pin is sealed in a N_2 filled vial for transfer to the diffractometer. A Bruker SMART 1000, Bruker APEX or Bruker APEX II diffractometer equipped with a CCD detector and a graphite monochromated Mo K_α (λ=0.7069 Å) x-ray source was used. All of the diffractometers were equipped with N_2 cold streams, which were capable of cooling the crystal to 110 K and maintaining an inert atmosphere. A rotation photograph and small sets of frame

data, called matrix runs, were collected to check the quality of the crystal. The frame

data from the matrix runs could be indexed so that the unit cell parameters could be

compared to those of known compounds.   After it was established that a crystal could be

indexed accurately from the matrix run and the quality of the diffraction pattern seemed

satisfactory, a hemisphere of data was collected. A typical data collection strategy

consisted of collecting reflections in a 2θ range of 3-56º while scanning ω (180º scan

using a 0.3º step size and 10 second exposure time per step) at 3-4 different ϕ angles (0º,

90º, 180º and 270º) and then the process was repeated to collect data in a 2θ range of 14-

70º. Frame data was indexed using SMART[67] or APEX2[68] software and the peak

intensities were integrated using SAINT software.[69]   Absorption corrections were made

using SADABS software.[70] The SHELXTL version 6.10 software package[71] was used as

an interface to the SHELX-97 suite of programs,[72] which was used to implement

structure solutions by direct methods and full-matrix least-squares structural refinements

on F^2.

Magnetic Measurements

Magnetic susceptibility measurements were performed on some samples using a

SQUID (Quantum Design MPMSXL) magnetometer.[73] Samples were prepared by

placing 10-30 mg of sample in a plastic bag of known weight and placing the bag in a

plastic straw. All manipulations of the samples were done with plastic weight boats and

Teflon® coated spatulas and tweezers. Magnetic susceptibilities were measured as a

function of temperature by setting the applied field to 0.1 Tesla and sweeping the

temperature from 300º C to 10º C. This process was repeated for DC applied fields of

0.5, 1.0, 2.0, 3.0 and 3.5 Tesla. Occasionally, saturation magnetization measurements

were performed by holding the temperature at 5ºC and sweeping the DC applied field

from 0-7.0 Tesla. All data were corrected for the sample holder and the intrinsic

diamagnetic contributions of the sample.[74]

CHAPTER III

CsR(R$_6$CoI$_{12}$)$_2$ (R= Gd, Er) AND (CeI)$_{0.26}$(Ce$_6$MnI$_9$)$_2$: TWO NEW STRUCTURE TYPES FEATURING R$_6$Z CLUSTERS[*]

Introduction

      In the search for new compounds that contain reduced transition metal centered Ln$_6$ cluster compounds two structure types were discovered. The discovery of CsR(R$_6$CoI$_{12}$)$_2$ and (CeI)$_{0.26}$(Ce$_6$MnI$_9$) was a result of modifying reaction conditions for making known compounds. CsR(R$_6$CoI$_{12}$)$_2$ was made when attempting to make the Er and Gd analogs of Cs$_4$R$_6$ZI$_{13}$ (R= Ce, Pr; Z= Co, Os).[53] In attempts to make a Ce/Mn analog of α-K$_4$La$_6$OsI$_{14}$, crystals of (CeI)$_{0.24}$(Ce$_6$MnI$_9$) were found. While the goal was to make more iodide rich compounds and therefore more isolated clusters, CsGd(Gd$_6$CoI$_{12}$)$_2$ turned out to be a valuable piece to understanding the magnetic properties of these cluster compounds. There were 14 known structure types for lanthanide iodide compounds that contained uncondensed octahedral clusters (see Table 1.1) but with the discovery of these two new structure types the count is now up to 16.

Experimental

      Synthesis. CsGd(Gd$_6$CoI$_{12}$)$_2$ was first discovered in a reaction where CsI, GdI$_3$, CoI$_2$ and Gd turnings were ground with a mortar and pestle in the ratio intended to make a compound with the composition "Cs$_4$(Gd$_6$CoI$_{14}$)." The reactants were heated to 750°C from room temperature at a rate of 6°C/hr, and then maintained at 750°C for 600 hours.

The furnace was then turned off and allowed to cool to room temperature. The product contained black, cube-like crystals, which where determined to be $CsR(R_6CoI_{12})_2$ by single crystal x-ray diffraction. The use of a $3CsI:19GdI_3:6CoI_2:23Gd$ reactant ratio (~8% rich in Gd for the intended product) in a reaction heated to 750°C for 21 days, followed by slow cooling (4.5°C/hr) to 300°C, yielded a product containing ~95% $CsGd(Gd_6CoI_{12})_2$ and ~5% GdOI. An exactly analogous reaction designed to synthesize the Er analog resulted in the formation of $CsEr(Er_6CoI_{12})_2$ (~50%) and unknown phases.

$(CeI)_{0.26}(Ce_6MnI_9)_2$ was found in reactions load with KI, CeI_3, MnI_2 and Ce metal in ratios intended to make "$K_x(Ce_6MnI_{12+y})$." In most of these reactions, $(CeI)_{0.26}(Ce_6MnI_9)_2$, was found in the product as black, plate like or multifaceted crystals. Reactions that yielded $(CeI)_{0.26}(Ce_6MnI_9)_2$ were conducted at 850°C for 500 hours by first raising the temperature from ambient at a rate of 7°C/hr. The reaction tube was then cooled at a rate of 6°C/hr to 300°C, at which time the furnace was turned off. X-ray powder patterns of the reactions loaded at the composition "$KCe_{12}Mn_2I_{18}$" contained a small percentage (5-10%) of $(CeI)_{0.26}(Ce_6MnI_9)_2$, along with CeOI, and other unidentified phase or phases.

   X-ray Structure Determinations. For $CsGd(Gd_6CoI_{12})_2$ and $(CeI)_{0.26}(Ce_6MnI_9)_2$, single crystal X-ray data was collected using a Bruker SMART 1000 CCD X-ray diffractometer equipped with graphite monochromated Mo K_α radiation ($\lambda = 0.71073$ Å). A Bruker Apex CCD X-ray diffractometer was used to collect data for $CsEr(Er_6CoI_{12})_2$. Crystals of $CsGd(Gd_6CoI_{12})_2$ and $(CeI)_{0.26}(Ce_6MnI_9)_2$ were mounted on nylon loops using Apeizon N grease and then placed in a N_2 stream at 110 K for data collection; for $CsEr(Er_6CoI_{12})_2$, Paratone® oil was used to mount the crystal and N_2 stream was set at 250 K. Frame data were indexed using SMART software[67] and the peak intensities were integrated using SAINT software.[69] Absorption corrections were

made using SADABS software.[70] The SHELXTL version 6.10 software package[71] was used as an interface to the SHELX-97 suite of programs,[72] which was used to implement structure solutions by direct methods and full-matrix least-squares structural refinements on F^2.

A black crystal of $CsGd(Gd_6CoI_{12})_2$ with the dimensions $0.06 \times 0.02 \times 0.02$ mm^3 was mounted on the diffractometer and 29945 reflections were collected. The data was indexed with cubic cell, and assigned to the $Pa\bar{3}$ space group. However, the data exhibited 31 systematic absence violations and the refinement showed a residual Fourier peak of 4.19 e Å^3, which formed an octahedron surrounding the Cs atoms at a distance of 2.874 Å. Attempts to identify and resolve a twin relationship by use of Gemini,[75] CellNow,[76] Platon,[77] and twin suggestions from XPREP[71] were unsuccessful. Disorder models could not be refined either. The same problems occurred in the course of the structure solution of one crystal of $CsEr(Er_6CoI_{12})_2$. The residuals (R_1) were 0.0684 and 0.0617 ($I > 2\sigma(I)$) for $CsEr(Er_6CoI_{12})_2$ and $CsGd(Gd_6CoI_{12})_2$ respectively. The structure solution for a second crystal of $CsEr(Er_6CoI_{12})_2$ at 250 K was solved in the $Pa\bar{3}$ space group; the data exhibited six weak ($6\sigma(I) \gtrsim I$) systematic absence violations. The final residual was 0.0459 ($I > 2\sigma(I)$).

A summary of the crystallographic data for $CsEr(Er_6CoI_{12})_2$ and $(CeI)_{0.26}(Ce_6MnI_9)_2$ is shown in Table 3.1. The fractional coordinates for the crystal structure of these two compounds are shown in Tables 3.2 and 3.4. Interatomic distances for these compounds are shown in Tables 3.3 and 3.5.

Table 3.1. Crystallographic data for $CsEr(Er_6CoI_{12})_2$ and $(CeI)_{0.26}(Ce_6MnI_9)_2$

Formula	$CsEr_{13}Co_2I_{24}$	$Ce_{6.13}MnI_{9.13}$
Formula weight (g/mol)	5470.75	2072.34
Temperature (K)	250(2)	110(2)
Crys. sys., space group, Z	Cubic, $Pa\bar{3}$ (No. 205), 4	Trigonal, $P\bar{3}$ (No. 147), 2
Lattice parameter (Å)	18.063(2)	11.695(1), 10.859(2)
V (Å^3)	5893.8(12)	1286.3(3)
Density (calc.) (g/cm^3)	6.165	5.351
Abs. coefficient (mm^{-1})	32.008	21.993
Extinction coefficient	$3.4(4) \times 10^{-5}$	
Final R indices [I > 2σ(I)]	$R_1{}^a = 0.0459,$ $wR_2{}^b = 0.0932$	$R_1{}^a = 0.0895,$ $wR_2{}^c = 0.1868$
R indices (all data)	$R_1{}^a = 0.0701,$ $wR_2{}^b = 0.1019$	$R_1{}^a = 0.1239,$ $wR_2{}^c = 0.2032$

$^a R_1 = \sum \lVert F_o \rvert - \lvert F_c \rVert / \sum \lvert F_o \rvert$; $^{b,c} wR_2 = (\sum[w(F_o{}^2 - F_c{}^2)^2] / \sum[w(F_o{}^2)^2])^{1/2}$, where $^b w = 1/[\sigma^2(F_o{}^2) + (0.0386P)^2 + (33.2546P)]$ and $^c w = 1/[\sigma^2(F_o{}^2) + (0.0797P)^2 + (61.5001P)]$, $P = (F_o{}^2 + 2F_c{}^2)/3$

Table 3.2. Atomic coordinates and equivalent isotropic displacement parameters ($\text{Å}^2 \times 10^3$) for $CsEr(Er_6CoI_{12})_2$

Atom	Wyckoff symbol	X	Y	Z	$^a U_{eq}$
Er(1)	24d	0.1731(1)	0.3300(1)	0.5241(1)	8(1)
Er(2)	24d	0.3141(1)	0.3298(1)	0.6677(1)	7(1)
Er(3)	4a	0	0.5000	0.5000	9(1)
I(1)	24d	0.1686(1)	0.3356(1)	0.3425(1)	15(1)
I(2)	24d	0.4954(1)	0.3332(1)	0.6623(1)	16(1)
I(3)	24d	0.3386(1)	0.3356(1)	0.5012(1)	17(1)
I(4)	24d	-0.0008(1)	0.3338(1)	0.4973(1)	12(1)
Cs(1)	4b	0.5000	0.5000	0.5000	40(1)
Co(1)	8c	0.1693(1)	0.3307(1)	0.6693(1)	7(1)

$^a U_{eq} = (8\pi^2/3) \sum_i \sum_j U_{ij} a_i{}^* a_j{}^* \bar{a}_i \bar{a}_j$.

Table 3.3. Selected interatomic distances (Å) and angles (degrees) for $CsEr(Er_6CoI_{12})_2$

Distances:

Er(1)-Co(1)	2.624(2)	Er(2)-I(2)$^{a\text{-}i}$	3.278(1)
Er(2)-Co(1)	2.615(2)	Er(2)-I(2)$^{i\text{-}a}$	3.185(1)
		Er(2)-I(3)^{i}	3.043(1)
Er(1)-Er(1)	3.769(1)		
Er(2)-Er(2)	3.708(1)	Er(3)-I(4)	3.004(1)
Er(1)-Er(2)	3.707(1)		
	3.635(1)	Cs(1)-I(2)	4.205(1)
		Cs(1)-I(3)	4.161(1)
Er(1)-I(1)$^{a\text{-}i}$	3.283(1)		
Er(1)-I(2)$^{i\text{-}a}$	3.075(1)	Angles:	
Er(1)-I(3)^{i}	3.020(1)	I(2)-Er(1)-I(4)	161.57(4)
Er(1)-I(4)^{i}	3.180(1)	I(3)-Er(1)-I(4)	163.07(4)
	3.156(1)	I(1)-Er(2)-I(2)	165.17(4)
		I(3)-Er(2)-I(1)	161.84(4)
Er(2)-I(1)$^{i\text{-}a}$	3.075(1)		
	3.136(1)		

Table 3.4. Atomic coordinates and equivalent isotropic displacement parameters ($Å^2 \times 10^3$) for $(CeI)_{0.26}(Ce_6MnI_9)$

Atom	Wyckoff symbol	x	y	z	$U_{eq}{}^a$	SOF
Ce(1)	6g	0.5468(1)	0.70796(9)	0.47641(9)	37.0(3)	1
Ce(2)	6g	0.50495(8)	0.87544(8)	0.18216(8)	23.8(2)	1
Ce(3)	6g	0.233(2)	0.036(2)	0.1629(19)	29(6)	0.043(4)
I(1)	6g	0.47818(8)	0.10598(8)	0.31898(8)	22.1(2)	1
I(2)	6g	0.77171(9)	0.96436(9)	0.33649(8)	26.4(2)	1
I(3)	6g	0.28490(9)	0.8693(1)	-0.00381(8)	27.1(2)	1
I(4)	1b	0	0	0	190(20)	0.26(2)
Mn(1)	2d	0.3333	0.6667	0.3318(4)	33.2(9)	1

$^aU_{eq} = (8\pi^2/3) \sum_i\sum_j U_{ij}a_i{}^*a_j{}^*\bar{a}_i\bar{a}_j.$

Table 3.5. Selected atomic distances (Å) and angles (degrees) for $(CeI)_{0.26}(Ce_6MnI_9)$

Ce(1)-Ce(1)	3.908(2)	Ce(3)-I(1)	3.07(2)
Ce(2)-Ce(2)	3.973(2)	Ce(3)-I(2)	3.14(2)
Ce(1)-Ce(2)	3.941(1)		3.15(2)
	3.904(2)	Ce(3)-I(3)	2.94(2)
			3.13(2)
Ce(1)-I(1)$^{i\text{-}i}$	3.228(1)	Ce(3)-I(4)	3.10(2)
Ce(1)-I(2)$^{i\text{-}a}$	3.222(1)		
Ce(1)-I(3)$^{i\text{-}a}$	3.244(1)	Ce(1)-Mn	2.780(3)
	3.194(1)	Ce(2)-Mn	2.780(3)
Ce(1)-I(3)$^{a\text{-}i}$	3.372(1)		
		Angles:	
Ce(2)-I(1)$^{i\text{-}i}$	3.224(1)	I(1)-Ce(2)-I(1)	165.27(5)
	3.259(1)	I(1)-Ce(2)-I(2)	164.73(5)
	3.293(1)	I(1)-Ce(1)-I(3)	163.67(4)
Ce(2)-I(2)$^{i\text{-}a}$	3.214(1)	I(2)-Ce(1)-I(3)	163.86(4)
Ce(2)-I(2)$^{a\text{-}i}$	3.420(2)		

A black multifaceted crystal of $(CeI)_{0.26}(Ce_6MnI_9)_2$, with the dimensions 0.11 × 0.12 × 0.12 mm^3, was mounted on the diffractometer and 3332 reflections were collected and indexed in the $P\bar{3}$ space group. During the data collection the crystal mounting pin obstructed the x-ray beam path causing a series of consecutive frames to be void of diffraction peaks from the crystal. The frames affected by the obstruction were not included in the data used to solve the structure. The basic structure emerged from direct methods and refined without difficulty, but two electron density peaks remained in an otherwise vacant cuboctahedral cavity created by the clusters. Since there were no unindexed reflections, no twinning beyond that by merohedry was deemed possible. After attempting every merohedral twin model suggested by XPREP[71] without making any headway, we considered disorder models (see discussion section). The most reasonable model was to restrain the non-cluster Ce and I to have the same occupancy

factor. This resulted in 26% of the cavities containing additional cerium and iodide ions, leaving the remaining cavities vacant.

Elemental Analysis. In order to establish whether potassium was present in $(CeI)_{0.26}(Ce_6MnI_9)_2$, X-ray photoelectron spectra (XPS) were recorded on a Kratos Axis Ultra Imaging X-ray photoelectron spectrometer equipped with an Al anode and a multichannel detector. Charge referencing was performed against adventitious carbon (C 1s, 284.5 eV). Samples were prepared by picking crystals (of like morphology) from reaction product mixtures from which crystals for X-ray structure determination were taken. XPS measurements were performed on two different samples. Potassium was not detected in either of the samples. The K/Mn atomic ratio for a benchmark $KMnCl_3$ sample was determined to be 56:44.

Atomic absorption (AA) spectroscopy was also used to determine the possible presence of potassium; crystals were selected in the same manner as those used for XPS measurements. The 3.3 mg sample was dissolved in 0.048 M HCl (5.0 ml) and analyzed on a Varian 250 AA system. The same HCl solution was used as the blank. The potassium content of the sample was not determined to be significantly different from the blank.

Results and Discussion

Synthesis. As indicated in the experimental section, $CsGd(Gd_6CoI_{12})_2$ is a stable phase that can be prepared in a yield that is less than quantitative only because it is difficult to entirely avoid oxygen-containing impurities. Thus, a modest excess of gadolinium is necessary to obtain the best practical results. For the erbium analog,

$CsEr(Er_6CoI_{12})_2$, our yields never exceeded the 50% reported here. Variations in stoichiometry and reaction temperatures were to no avail. The competing (and well-known) structure type, $Er(Er_6CoI_{12})$, is often observed as the major side-product of such attempts. We are very much interested in varying the magnetic properties of these compounds and so were motivated to incorporate Fe, Mn and Ni as interstitial atoms in compounds of this type, but such attempts resulted in the formation of $R(R_6ZI_{12})$, unreacted CsI, and/or other unidentified phases.

$(CeI)_{0.26}(Ce_6MnI_9)_2$ was found in several reactions loaded with KI, CeI_3, MnI_2 and Ce metal in ratios intended to target Ce analogs of α- or β-$K_4La_6OsI_{14}$,[56,55] and new compounds with $K_x(Ce_6MnI_{12+y})$ compositions. Despite the absence of potassium in this compound, we have so far only definitively observed this product in reactions including KI. Reactions loaded with CeI_3, MnI_2 and Ce metal in ratios at and near "Ce_6MnI_9" yielded similar black, plate-like crystals, but these diffracted poorly. Powder diffraction data did not indicate the presence of the sought-after $(CeI)_{0.26}(Ce_6MnI_9)_2$ when KI was not present. Since these reactions were conducted at 850 ˚C, above the melting point of KI, we speculate that the KI melt may allow nucleation of this phase. The reactions that were loaded with an excess of KI still yielded $(CeI)_{0.26}(Ce_6MnI_9)_2$ and contained white powder in the final product, but KI was not observed in the x-ray powder patterns of the products.

Structure. The $CsR(R_6CoI_{12})_2$ structure type may be viewed as an intergrowth of the $R(R_6CoI_{12})$ and $Cs(Er_6CI_{12})$ structure types; we preface our discussion of the structure with brief remarks concerning these two structures in order to clarify this viewpoint. If we adopt a view wherein the R_6ZI_{12} cluster is aligned with a 3-fold axis is vertical, then six of the cluster's bridging iodides may be described as 'waist' ligands (girding the center of the cluster at the same 'height' as the interstitial Z atom; Z = C,

Co). The other six iodide ligands bridge R–R bonds that make up the top and bottom triangular faces of the R_6 trigonal antiprism. In the $R(R_6CoI_{12})$ structure, cluster crosslinking occurs exclusively through the waist iodides and a $R\bar{3}$ structure is thereby generated. The 'top' and the 'bottom' iodides on vertically adjacent clusters form opposite triangular faces of a trigonal antiprism in which R^{III} ions are situated (top left, Figure 3.1). In the $Cs[Er_6CI_{12}]$ structure, cluster crosslinking occurs exclusively via the 'top' and 'bottom' iodides and all the iodides form cuboctahedral sites for 12-coordinate Cs ions (bottom left, Figure 3.1). A cubic ($Pa\bar{3}$) intergrowth of these two $R\bar{3}$ structures is generated by aligning the 3-fold axes of the two structures and "fusing" clusters (Figure 3.1). The full cubic symmetry structure emerges as cluster fusions are performed along nonintersecting 3-fold axes that run through each of the Cs^I and R^{III} ions in the structure. (Only the Cs polyhedron for the ion at (1/2, 1/2, 1/2) is shown; equivalent Cs positions at (1/2, 0, 0), (0, 1/2, 0), and (0, 0, 1/2) are not shown).
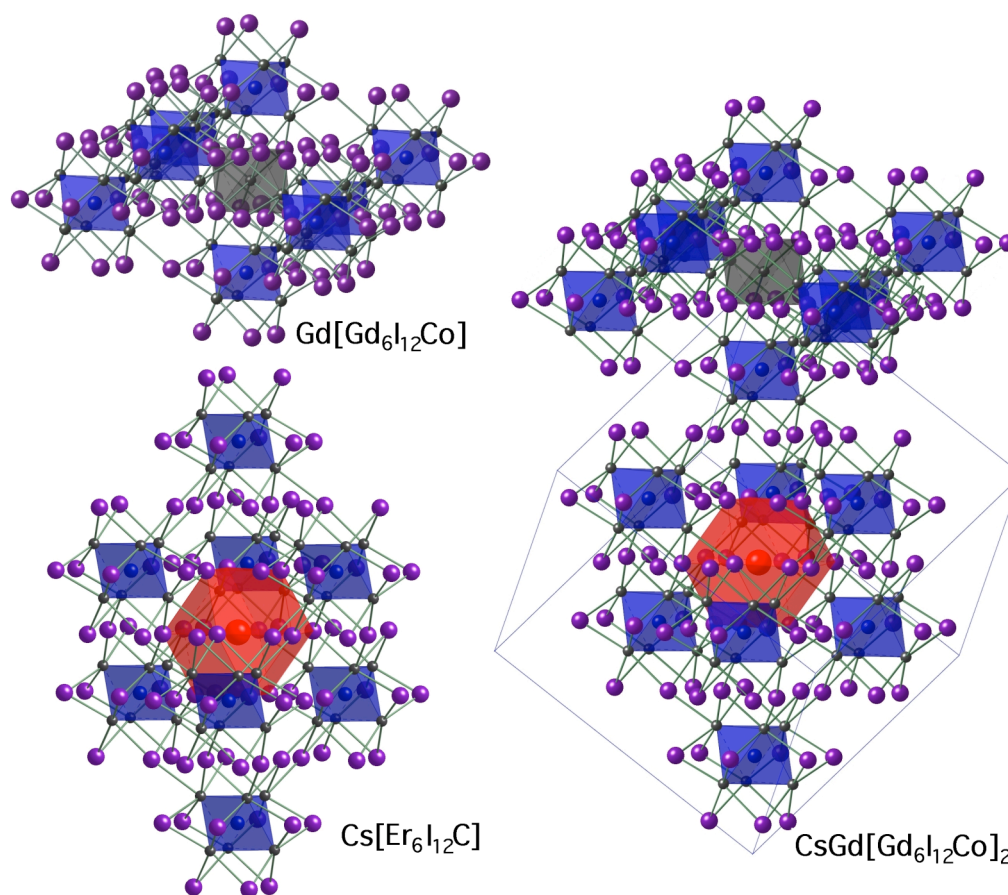
Figure 3.1. Structural relationship between Gd[(Gd$_6$Co)I$_{12}$], Cs[(Er$_6$C)I$_{12}$] and CsGd[(Gd$_6$Co)I$_{12}$]$_2$. The blue octahedra represent the Ln$_6$Z (Z = Co or C) units. The red cuboctahedron is a CsI$_{12}$ coordination polyhedron and Gd^{III}I$_6$ octahedron is grey.

When the CsGd(Gd$_6$CoI$_{12}$)$_2$ structure was initially determined, refinement in the Pa$\bar{3}$ space group was accompanied by difficulties symptomatic of twinning by merohedry: all reflections could be indexed, but there were numerous systematic absence violations of significant intensity and spurious peaks in the electron density persisted in the refined structure (e.g., a trigonal antiprism of electron density peaks, each ~ 4 e Å^{-3}, with dimensions similar to a Gd$_6$ cluster surrounding the Cs site). Various disorder models and twin laws were attempted, but no simple twinning sufficed;

more than one twin domain was probably present in this cubic case. The first several crystals obtained for $CsEr(Er_6CoI_{12})_2$ exhibited the same characteristics. Post publication of this structure, a compound with the same structure type we discovered, $CsGd(Gd_6C_2I_{12})_2$. The structure of $CsGd(Gd_6C_2I_{12})_2$ was solved as being twinned and is discussed in Chapter V. Unfortunately the same twin law used in the solution for the structure of $CsGd(Gd_6C_2I_{12})_2$ did not apply to the data collected for $CsGd(Gd_6CoI_{12})_2$ or $CsEr(Er_6CoI_{12})_2$. Fortunately, a crystal of $CsEr(Er_6CoI_{12})_2$ where these problems were minimal was found (six systematic absence violations were observed, but the peak intensities were quite weak, $6\sigma(I) \gtrsim I$).

In the structure of $(CeI)_{0.26}(Ce_6MnI_9)_2$, each cluster is centered on a 3-fold axis and is linked to six neighboring clusters through bridging iodides. Three clusters are linked through $I^{i\text{-}i}$, $I^{i\text{-}a}$ and $I^{a\text{-}i}$ bridges, the other three clusters are linked by $I^{i\text{-}a}$ and $I^{a\text{-}i}$ bridges. Thus, the structure can be viewed as layers of tightly cross-linked clusters (three iodine bridges) and the layers are joined by loose cross-linking (two iodine bridges), as shown in Figure 3.2. The resulting connectivity can be described as $(CeI)_{0.26}(Ce_6Mn)I^{i\text{-}i}_{6/2}I^{i\text{-}a}_{6/2}I^{a\text{-}i}_{6/2}$. The Mn-Mn distances within the layers are 7.677 Å, where as the Mn-Mn distances between the layers are 9.875 Å. The cavities are partially occupied by Ce-I units. The Ce atoms of the Ce-I units are disordered over six equivalent positions. When the structure is viewed down the c axis, as in Figure 3.3, the cavities stack upon each other to form channels.
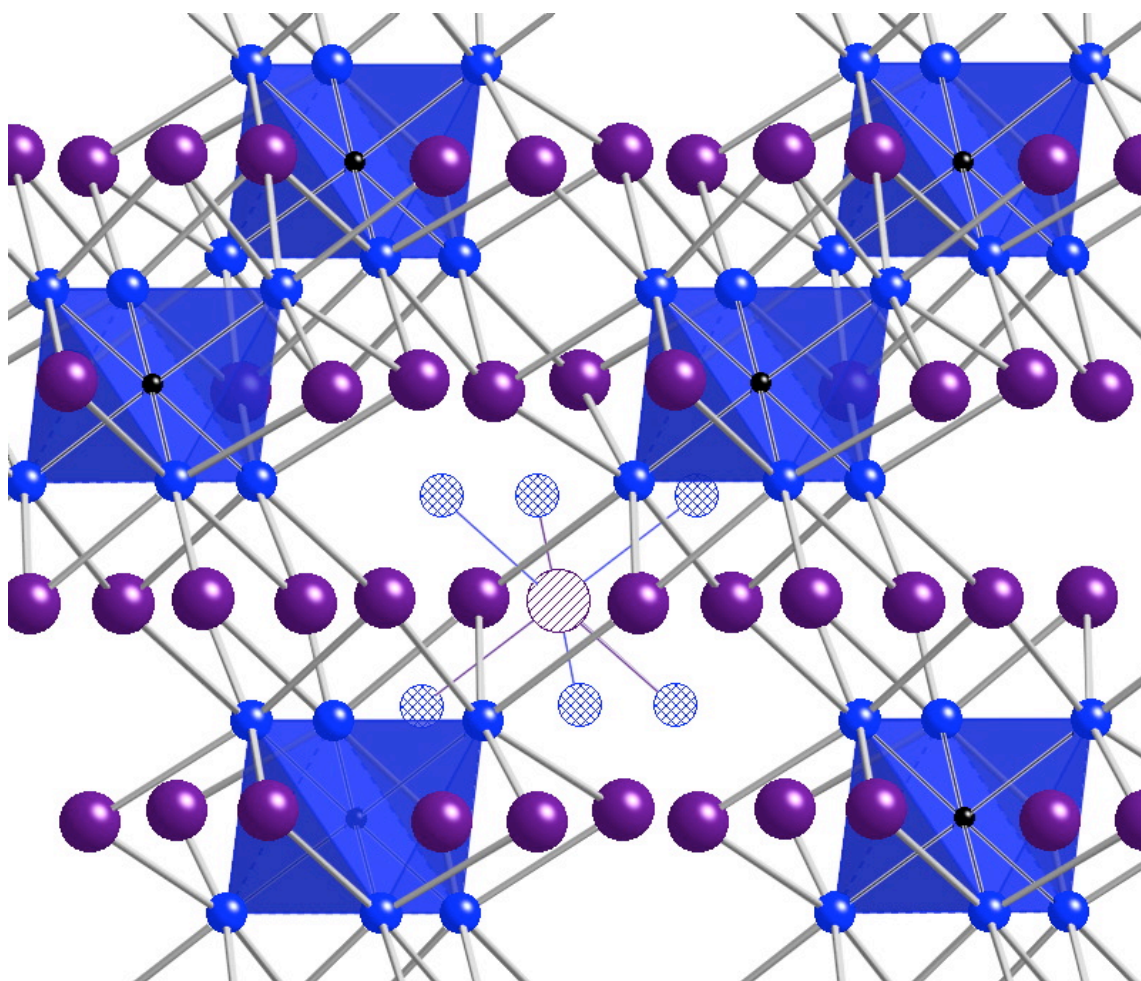
Figure 3.2. View through the [011] plane of $(CeI)_{0.26}(Ce_6MnI_9)_2$; Ce_6Mn cores are represented as blue trigonal anti-prisms, the iodine atoms are purple. The sites of disorder in the cavity are shown as hatched and striped circles for Ce(3) and I(4) respectively. Only one set of sites of disorder is shown for clarity.
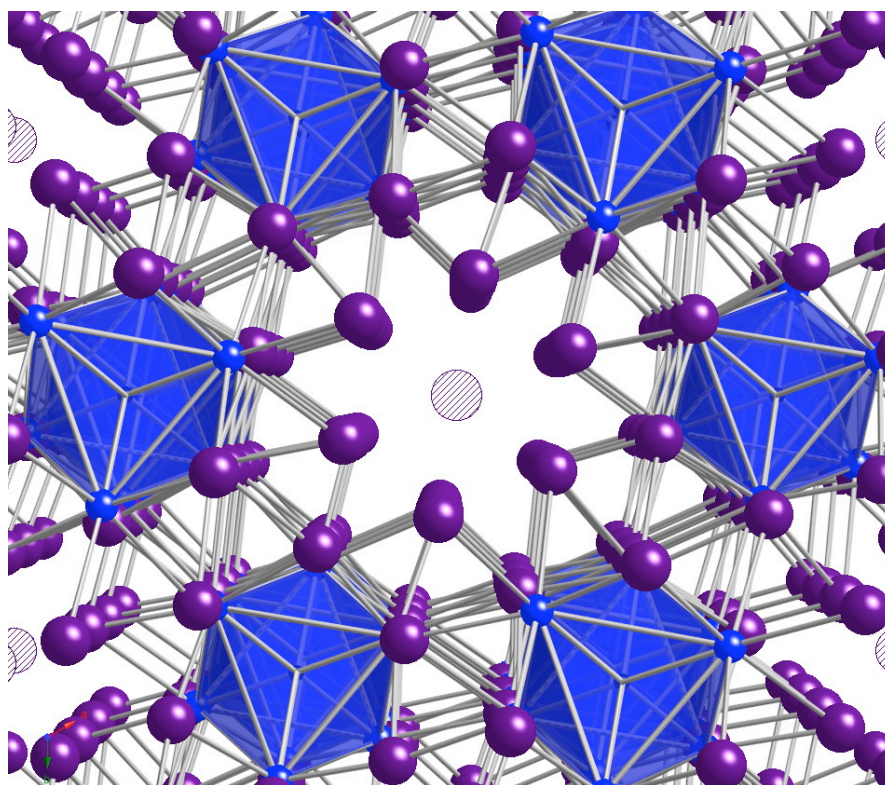
Figure 3.3. View down the c axis of $(CeI)_{0.26}(Ce_6MnI_9)_2$; cluster and atom color scheme as in Figure 3.2. The iodine atoms that form the cavity obscure the non-cluster Ce atoms.

The structure was solved two times from two different crystals that were picked from two different samples. The first solution came from data (6136 reflections) collected out to 56° 2θ. This solution yielded better residuals than those reported here: $R_1 = 0.0502$ ($F_o > 4sig(F_o)$), and the CeI occupancy of the cavity sites was refined to 24%. Concerned that the electron density peaks in the cavity might be artifacts attributable to truncation error, we collected a second, larger set of data (20216 reflections, 2θ < 68°). However, virtually the same solution was obtained, albeit with larger residual peaks (~8 e Å^{-3}, located 0.5 Å distant from Ce1) after the final solution. Despite the somewhat poorer residuals for this solution ($R_1 = 0.089$), we elected to report the results obtained for this larger data set.

We initially refined the structure with potassium occupying the two sites in the cavity, in light of potassium being reported as occupying a large cavity in a similar compound, KPr_6OsI_{10}.[35] However, XPS and AA results indicated that there is no potassium in the structure. A new disorder model containing cerium and iodine was used.

After refining the clusters, the center position of the cavity exhibited a significant residual electron density peak. Since cerium is far too small to occupy this position, iodine was assigned to it. The distances from the center of the cavity and the edge bridging iodine atoms of the clusters (6×4.31 Å and 6×4.42 Å) are longer than twice the *Shannon* crystal radius for 6 coordinate I^- (4.06 Å).[78] Since an unbound iodide ion is chemically unreasonable, a cerium atom was refined in the general position(s) that form a trigonal antiprism around the central I atom. The distance from this cerium atom to the nearest iodine atoms range from 2.94 Å to 3.15 Å which is short compared to the Ce^{3+}-I^- calculated from *Shannon crystal radii*[78] (3.34 Å).

The Fourier peaks for the two positions in the cavity indicate the electron density on both positions fell far short that needed for full occupancy of the sites. The disorder model used in the refinement consisted of restraining the occupancy of the non-cluster Ce such that its total population in the crystal equaled that of the iodine atoms in the center of the cavity. As a rationalization of this choice, we note that this allows no cavity iodides to remain unbound and allows no 5-coordinate cerium. This refinement model yielded a 26% occupancy of the cavities by CeI units.[79]

The anisotropic displacement parameters for the Ce atoms in the cavity could not be refined in a physically reasonable way and were therefore left isotropic. The iodine atom refined as a large prolate displacement ellipsoid (shown in figure 3.4), but this almost certainly reflects its average position, since there is no reason to believe that the

center of the cavity is at the optimal bonding distance with respect to the surrounding Ce positions.
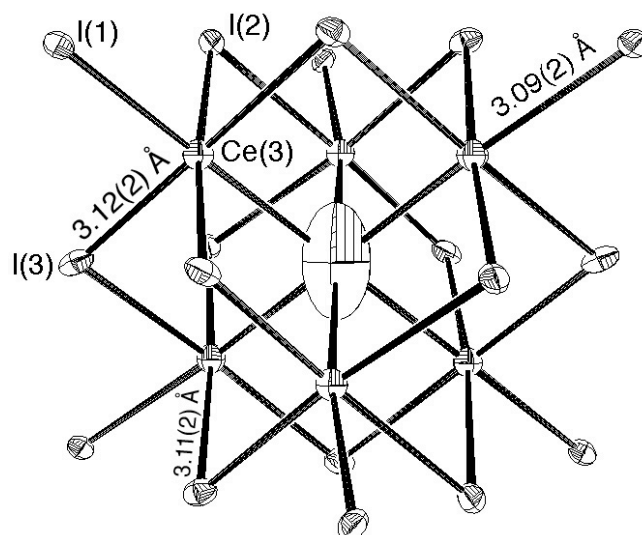
Figure 3.4. Coordination environment of I(4) (center) and Ce(3) in $(CeI)_{0.26}(Ce_6MnI_9)_2$. Ce(3) was refined isotropically. Ellipsoids drawn at 60%.

Conclusions

In attempts to find analogs of known $Cs_4R_6ZI_{13}$ and α-$K_4La_6OsI_{14}$ phases, we've discovered two new structure types of compounds containing reduced Ln-iodide clusters. With only 8 types of iodine bridges to neighboring octahedral lanthanide clusters ($I^{i\text{-}i}$, $I^{a\text{-}a}$, $I^{i\text{-}a}$, $I^{a\text{-}i}$, $I^{a\text{-}a\text{-}i}$, $I^{i\text{-}a\text{-}a}$, I^a, I^i), 16 different structure types have so far been observed. $CsEr(Er_6CoI_{12})_2$ and $CsGd(Gd_6CoI_{12})_2$ adopt a cubic intergrowth of two different $R\bar{3}$ structure types. The channels formed by the crosslinking of the clusters in $(CeI)_{0.26}(Ce_6MnI_9)_2$ may be capable of accommodating a range of cations. The magnetic properties of $CsGd(Gd_6CoI_{12})_2$ will be discussed in the next chapter (Ferromagnetic Coupling of Hexanuclear Gd Clusters).

CHAPTER IV

FERROMAGNETIC COUPLING IN HEXANUCLEAR Gd CLUSTERS[*]

Introduction

In this chapter, we investigate the series of compounds $CsGd(Gd_6CoI_{12})_2$ (described in the previous chapter), $Gd(Gd_6ZI_{12})$ (Z = Co, Fe or Mn) [38] and $Ca_xGd_{1-x}(Gd_6MnI_{12})$. These compounds provide a series of systems in which the Z-centered hexanuclear gadolinium clusters exhibit varying electron counts and allow us to investigate the effect that unpaired delocalized electrons have on magnetic coupling within the clusters. In the temperature-dependent magnetic susceptibility measurements and theoretical calculations reported here, we propose an exchange mechanism that explains the magnetic properties of compounds that contain Gd_6ZI_{12} types of clusters.

Experimental

Synthesis. $Gd[Gd_6ZI_{12}]$ (Z = Mn, Fe or Co) were prepared in reactions loaded with stoichiometric proportions of GdI_3, ZI_2 (Z = Mn, Fe, Co) and Gd metal turnings and heated in Nb tubes to 850°C for 16 days, as described previously.[38] $CsGd[Gd_6CoI_{12}]_2$ was synthesized by mixing CsI, GdI_3, CoI_2 and Gd metal turnings in a 3:19:6:23 ratio and heating to 750°C for 500 hours, followed by slow cooling (4.5°C/hr) to 300°C (reference to be published). In order to minimize contamination of samples by ferromagnetic impurities, Teflon® or Teflon® coated utensils were used when handling the products.

X-Ray Diffraction Studies. The products were identified by X-ray powder diffraction methods. The purity of the compounds was evaluated by comparison of their X-ray powder patterns with those calculated based on reported structures or single crystal data. A Bruker AXS D8 powder x-ray diffractometer equipped with graphite monochromated Cu K_α X-ray source was used with an airtight sample holder in order to obtain powder diffraction patterns of the samples. Using the program Powder Cell for Windows,[64] diffraction peaks from the samples were matched with the calculated diffraction peaks from the corresponding crystal structures. The desired cluster compounds were identified as the major phases, with GdOI identifiable as a side product (~1-5%).

X-ray diffraction data were collected on a single crystals of $Gd(Gd_6CoI_{12})$ and $Ca_{0.56}Gd_{0.44}(Gd_6MnI_{12})$, using Bruker x-ray diffractometers equipped with graphite monochromated Mo K_α radiation ($\lambda = 0.71073$ Å). A Bruker SMART 1000 CCD x-ray diffractometer and a Bruker Apex II CCD x-ray diffractometer were used for data collection on crystals of $Gd(Gd_6CoI_{12})$ and $Ca_{0.56}Gd_{0.44}(Gd_6MnI_{12})$ respectively. The crystals were mounted on nylon loops using Apeizon[®] N grease and then placed in a N_2 stream at 110 K for data collection. Frame data was indexed using SMART software[67] on the SMART 1000 diffractometer and the APEX II software package[68] for the APEX II diffractometer. The peak intensities were integrated using SAINT software.[69] Absorption corrections were made using SADABS software.[70] The SHELXTL version 6.10 software package[71] was used as an interface to the SHELX-97 suite of programs,[72] which was used to implement structure solutions by direct methods and full-matrix least-squares structural refinements on F^2.

Magnetic Measurements. Magnetic measurements were performed with a Quantum Design SQUID magnetometer MPMSXL on polycrystalline samples of

$Gd[Gd_6MnI_{12}]$, $Gd[Gd_6FeI_{12}]$, $Gd[Gd_6CoI_{12}]$ and $CsGd(Gd_6CoI_{12})_2$. Temperature dependent magnetization data were collected at 2-5 K intervals from 2-300K in applied fields of 0.1, 0.5, 1.0, 2.0 and 3.0 Tesla. All data were corrected for the sample holder contribution and for the intrinsic diamagnetic contributions after the measurements.[74]

Theoretical Background

The $4f$ orbitals on lanthanide atoms are highly contracted and their participation in Ln-ligand superexchange coupling is effectively precluded. However, a substantial *intraatomic* exchange interaction between $4f$ electrons and valence $5d$ and $6s$ electrons is present. Atomic spectral data for Gd $([Xe]4f^7 5d^1 6s^2)^{[13]}$ show a large energetic cost of "flipping" the $4f^7$ spin in opposition to the $5d$ electron $(E(^9D) - E(^7D) = 0.793$ eV; computed to be 0.706 eV in our calculations).[23,80] The $4f^7$-exchange field can be viewed as a contact interaction that exerts its direct influence only on orbitals centered on the gadolinium atom because only the valence $5d$ and $6s$ electrons significantly penetrate the atomic core, where they experience the effect of this exchange field. The more contracted $5d$ orbitals penetrate to a greater extent than the $6s$ orbital, and consequently the $5d$ electrons experience greater exchange interaction with the $4f^7$-core.

Figure 4.1 illustrates how the potential from the $4f^7$ core affects electrons that reside in with $5d$- and $6s$-character for the Gd atom. At the left side of Figure 4.1, we depict an "unperturbed" system wherein the valence d-electron experiences an average exchange potential from the half-filled $4f$ shell, so the d-electron has no preferred spin orientation. Upon applying the exchange field, the spin aligned with (against) the $4f$ spins is stabilized (destabilized) by an energy δ. For a Gd atom, 2δ is just the difference between the ^9D ground state and the first excited state, ^7D. These exchange interactions are intrinsically "ferromagnetic", favoring parallel alignment of the $4f$ and $5d$ spins.
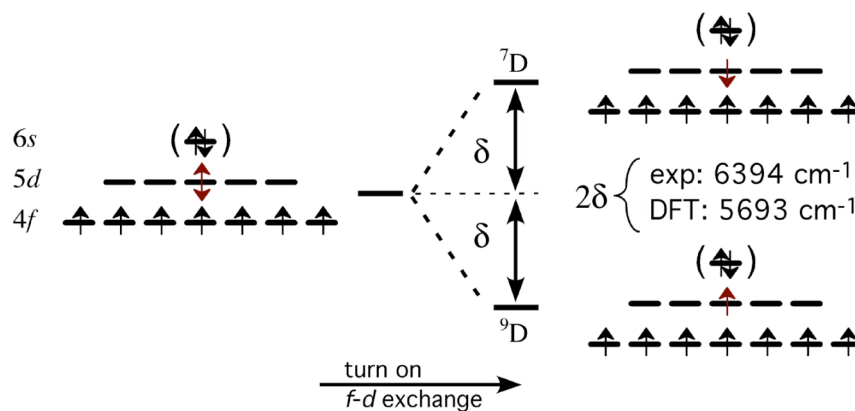
Figure 4.1. Electronic splitting of the Gd atom as a function of $4f$-$5d$ exchange perturbation.

Results and Discussion

Structures. The rhombohedral R[R_6ZX_{12}] structure ($R\bar{3}$ or $R3$), has been determined for R = Sc, Y, and many of the lanthanides, La-Lu ,where X= Cl, Br, or I.[31,38,43,46,81] Because we focus here on the magnetic properties of Gd-containing clusters, Gd[Gd_6ZI_{12}], we have determined the single crystal structures of Gd(Gd_6CoI_{12}), features of which may have an effect on the electronic and magnetic properties. These structures exhibit one crystallographically distinct cluster per cell (Figure 4.2); all 12 Gd-Gd edges of the cluster are bridged by one of two crystallographically distinct iodide atoms. Six iodine atoms bridge the "waist" edges of each Gd_6 octahedron and simultaneously form exo bonds to metal vertices of adjacent clusters (X^{i-a}).
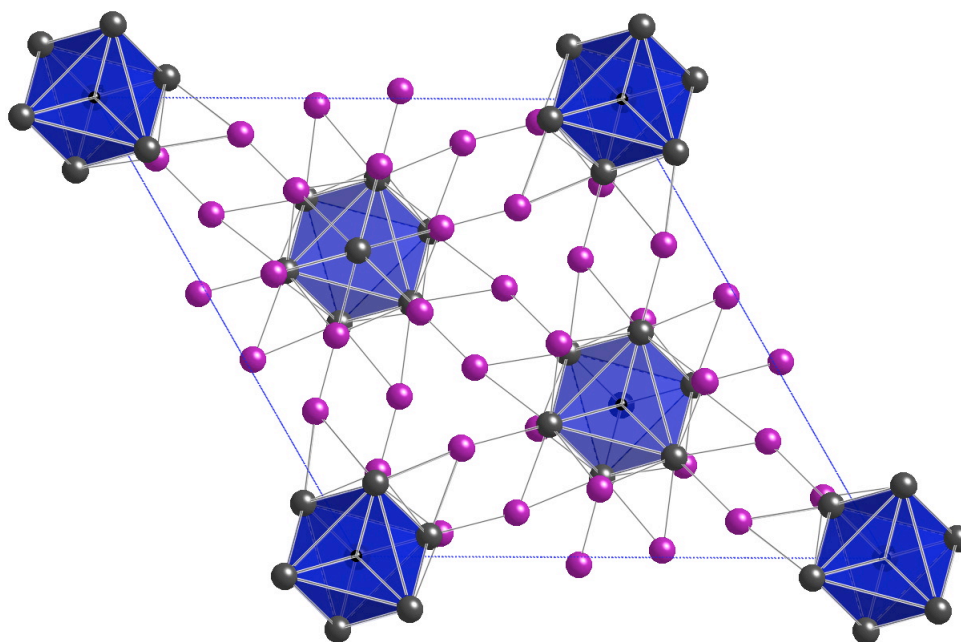
Figure 4.2. *c*-axis projection of Gd(Gd$_6$CoI$_{12}$) ($R\bar{3}$).

The other six halide atoms bridge Gd-Gd edges at the "top" and "bottom" triangular faces of the Gd$_6$ trigonal antiprism (I^i). The seventh Gd atom, located midway between the (Gd$_6$Z)I$_{12}$ clusters along the *c* axis, binds to six I^i atoms that form a trigonal antiprism. Because it does not participate in metal-metal bonding, it can be regarded as a Gd^{III} ion. Using the established notation, the structures are thus described as Gd^{3+}[Gd$_6$Z(I^i)$_6$(I^{i-a})$_{6/2}$(I^{a-i})$_{6/2}$]$^{3-}$. In the centric ($R\bar{3}$) structures, the symmetry of the Gd$_6$ZI$_{12}$ clusters deviates very slightly from D_{3d} and the departure from octahedral symmetry is small enough that an O_h approximation is still useful in discussing their electronic structure.

The single crystal structures of Gd(Gd$_6$CoI$_{12}$) and Ca$_{0.56}$Gd$_{0.44}$(Gd$_6$MnI$_{12}$) were determined and the data is presented in Tables 4.1-4.4. Unit cell parameters had been determined from Guinier camera powder diffraction film data for Gd(Gd$_6$CoI$_{12}$),[38] but a

single crystal structure determination had not been reported. Since the powder

diffraction data for $Gd(Gd_6CoI_{12})$ were obtained in the presence of a primary silicon

standard, the smaller parameters found here (0.046 Å for *a* and 0.059 Å for *c*) are likely

the result of drift in diffractometer angles between calibrations – the powder data were

collected at ambient temperature and the parameters would be expected to be longer.

While there have been several studies of the 7-12 structure type, [37-40] the crystal structure

of a Mn centered Gd cluster has not yet been reported.

Table 4.1. Crystallographic data for $Gd(Gd_6CoI_{12})$ and $Ca_{0.56}Gd_{0.44}(Gd_6MnI_{12})$

Empirical formula	Gd_7CoI_{12}	$Ca_{0.56}Gd_{6.44}MnI_{12}$
Crystal size	$0.11 \times 0.08 \times 0.07$ mm^3	$0.16 \times 0.09 \times 0.02$ mm^3
Formula Weight	2682.48 g/mole	2612.87 g/mole
Temperature (K)	110(2)	110(2)
Crystal system, Space group, Z	Trigonal, $R\overline{3}$ (No. 148), 3	Trigonal, $R\overline{3}$ (No. 148), 3
Unit cell dimensions *a,c*	15.412(2) Å, 10.678(2) Å	15.4625(3) Å, 10.6579(5) Å
Volume	2196.5(6) Å^3	2206.79(12) Å^3
Density (calculated)	6.084 mg/cm^3	5.898 mg/cm^3
2θ range for data collection	4.88 to 46.52°.	4.88 to 67.48°
Reflections collected	3854	14798
Independent reflections	707 [R(int) = 0.0479]	1907 [R(int) = 0.0496]
Absorption coefficient	28.800 mm^{-1}	27.389 mm^{-1}
Extinction coefficient	$1.54(8) \times 10^{-4}$	Not used
Final R indices [I>2σ(I)]	$R_1 = 0.0247$, $wR_2 = 0.0492$	$R_1 = 0.0233$, $wR_2 = 0.0519$
R indices (all data)	$R_1 = 0.0282$, $wR_2 = 0.0503$	$R_1 = 0.0279$, $wR_2 = 0.0540$

[a]$R_1 = \sum||F_o|-|F_c|| / \sum|F_o|$; [b]$wR_2 = (\sum[w(F_o^2-F_c^2)^2 / \sum[w(F_o^2)^2])^{1/2}$; $w = 1/[\sigma^2(F_o^2) + (0.0166P)^2]$ for $Gd(Gd_6CoI_{12})$ and $w = 1/[\sigma^2(F_o^2) + (0.0253P)^2]$ for $Ca_{0.56}Gd_{0.44}(Gd_6MnI_{12})$, where $P = (F_o^2 + 2F_c^2)/3$

Table 4.2. Atomic coordinates and equivalent isotropic displacement parameters for $Gd(Gd_6CoI_{12})$ and $Ca_{0.56}Gd_{0.44}(Gd_6MnI_{12})$

Atom	Wyckoff symbol	x	Y	Z	$U_{eq}{}^a$	SOF
			$Gd(Gd_6CoI_{12})$			
Gd(1)	3b	0	0	0.5	0.0091(3)	1
Gd(2)	18f	0.0440(1)	0.1587(1)	0.8586(1)	0.0043(2)	1
I(1)	18f	0.8676(1)	0.0516(1)	0.6599(1)	0.0066(2)	1
I(2)	18f	0.2376(1)	0.3171(1)	0.9947(1)	0.0080(2)	1
Co(1)	3a	0	0	0	0.0026(6)	1
			$Ca_{0.56}Gd_{0.44}(Gd_6MnI_{12})$			
Ca(1)	3b	2/3	2/3	1/3	0.0257(3)	0.562(3)
Gd(1)	3b	2/3	2/3	1/3	0.0257	0.439(3)
Gd(2)	18f	0.5069(1)	0.2185(1)	0.3112(1)	0.01095(6)	1
I(1)	18f	0.7189(1)	0.5182(1)	0.1696(1)	0.01409(7)	1
I(2)	18f	0.4315(1)	0.0186(1)	-0.1637(1)	0.01496(7)	1
Mn(1)	3a	2/3	1/3	-1/6	0.0100(2)	1

$^a U_{eq} = (8\pi^2/3) \sum_i \sum_j U_{ij} a_i^* a_j^* \bar{a}_i \bar{a}_j.$

Table 4.3. Selected interatomic distances (Å) and angles (degrees) for $Gd(Gd_6CoI_{12})$

Distances:

Gd(2)-I(2)	3.1121(8)	Gd(1)-I(1)	3.0545(6)
Gd(2)-I(2)	3.1413(8)	Gd(2)-Gd(2)	3.7884(9)
Gd(2)-I(2)	3.3041(8)	Gd(2)-Gd(2)	3.7284(9)
Gd(2)-I(1)	3.1830(8)	Gd(2)-Co	2.6577(5)
Gd(2)-I(1)	3.1927(8)		

Angles:

I(1)-Gd(2)-I(2)	162.41(2)	Gd(1)-I(1)-Gd(2)	89.777(19)
I(1)-Gd(2)-I(2)	163.56(2)	Gd(1)-I(1)-Gd(2)	89.958(19)
I(1)-Gd(1)-I(1)	180.000(14)	Gd(2)-I(1)-Gd(2)	72.91(2)
Gd(2)-Gd(2)-Gd(2)	59.466(9)	Gd(2)-I(2)-Gd(2)	73.20(2)
Gd(2)-Co-Gd(2)	180.000(17)	Gd(2)-I(2)-Gd(2)$'$	97.271(19)

Table 4.4. Selected interatomic distances (Å) and angles (degrees) for $Ca_{0.56}Gd_{0.24}(Gd_6MnI_{12})$

Distances:			
Gd(2)-I(2)	3.1032(3)	Gd(1)-I(1)	3.0915(2)
Gd(2)-I(2)	3.1275(3)	Ca(1)-I(1)	3.0915(2)
Gd(2)-I(2)	3.3135(3)	Gd(2)-Gd(2)	3.7902(3)
Gd(2)-I(1)	3.1471(3)	Gd(2)-Gd(2)	3.8219(3)
Gd(2)-I(1)	3.1533(3)	Gd(2)-Mn(1)	2.6913(2)
Angles:			
I(1)-Gd(2)-I(2)	164.433(8)	Gd(1)-I(1)-Gd(2)	89.171(7)
I(1)-Gd(2)-I(2)	165.177(8)	Gd(1)-I(1)-Gd(2)	89.285(7)
Gd(2)-Gd(2)-Gd(2)	59.723(3)	Gd(2)-I(1)-Gd(2)	74.690(8)
Gd(2)-I(2)-Gd(2)′	96.688(7)	Gd(2)-I(2)-Gd(2)	74.933(8)

The Gd_6Z trigonal antiprism is compressed along the *c* axis. This is manifest in the difference between the Gd(2)-Gd(2) distances within (3.7884(9) Å, 3.7902(3) Å) and between (3.7284(9) Å, 3.8219(3) Å) the triangular Gd_3 faces normal to the 3-fold axis (of $Gd(Gd_6CoI_{12})$, $Ca_{0.56}Gd_{0.44}(Gd_6MnI_{12})$). The average Gd(2)–Co distance is 0.038 Å longer than the corresponding Er–Co distance in $CsEr(Er_6CoI_{12})_2$[82] than in $Gd(Gd_6CoI_{12})$, a bit less than the difference in the Pauling radii (for metals) of Er and Gd (0.047 Å).[83] The Gd(2)-Mn distance is 0.033 Å longer than the Gd(2)-Co distance, which is a little longer that the Pauling radii (for metals) difference of Co and Mn (0.009 Å).[83]

No single crystals of the fully substituted forms of $Gd(Gd_6MnI_{12})$ or $Ca(Gd_6MnI_{12})$ were obtained and no other methods to quantify the cation ratio (Ca/Gd) were performed. For the final refinement of the single crystal data of $Ca_{0.56}Gd_{0.44}(Gd_6MnI_{12})$ the occupancy of the cation site was constrained so that the sum of the occupancies of Gd and Ca would equal one and the displacement parameters would refine but be equal. This refinement resulted in a R_1 [$I>2\sigma(I)$] 0.0233. When the cation site was assigned to be unit occupancy of Gd the R_1 [$I>2\sigma(I)$] was 0.0566 (R_1(all)

0.0624, wR$_2$(all) 0.1841) and the U$_{eq}$ for the Gd in the cation site was 0.062. When the cation site was assigned to be unit occupancy of Ca the R$_1$ [I>2σ(I)] was 0.0631 (R$_1$(all) 0.0692, wR$_2$(all) 0.2043) and the U$_{eq}$ for Ca went negative (non positive definite).

In order to qualitatively determine the Ca/Gd cation ratio in the bulk the relative intensities of powder diffraction peaks were used. The most sensitive diffraction lines to the change in cation occupancy are the peaks from the (110) and (101) reflections. The 110 plane (d spacing is 7.7493 Å) slices through the noncluster Gd and Ca atoms whereas the 101 plane does not. The ratio in observed intensities of these lines were compared to the calculated intensities for the loaded stoichiometry (Table 4.5). As seen in Table 4.5 the trend of increasing the Ca/Gd loading ratio decreases I(110)/I(101). Since only three different loading ratios were used and the observed peak intensity ratios are different than those observed we regard the Ca/Gd ratio relationship between each sample to be qualitative. The powder pattern data supports the idea that there is some incorporation of Ca in the cation sight for the sample loaded for Ca$_{0.5}$Gd$_{0.5}$(Gd$_6$MnI$_{12}$) and this is also supported by the refinement of the single crystal data reported here. Based on the I(110)/I(101) ratio of the sample loaded for Ca(Gd$_6$MnI$_{12}$) we know that this sample has more Ca in the cation site than the sample loaded for Ca$_{0.5}$Gd$_{0.5}$(Gd$_6$MnI$_{12}$). Reactions loaded with a Ca:Gd ratio greater than 1:6 resulted in a I(110)/I(101) ratio no smaller than 1.32.

Table 4.5. The $I(110)/I(101)$ ratios of observed and calculated powder pattern data for $Ca_xGd_{1-x}(Gd_6MnI_{12})$

	$I(110)/I(101)$	
Loaded Composition	Observed	Calculated[65]
$Gd(Gd_6MnI_{12})$	3.09	2.61
$Ca_{0.5}Gd_{0.5}(Gd_6MnI_{12})$	1.70	1.23
$Ca(Gd_6MnI_{12})$	1.32	0.568

The structure of $CsGd(Gd_6CoI_{12})_2$, shown in Figure 4.3, features Gd_6CoI_{12} clusters with 3-fold symmetry. This structure type is well described as an intergrowth of $Gd(Gd_6CoI_{12})$ and $Cs(Er_6CI_{12})$ structure types.[82] Because the clusters have C_3 symmetry, the 12 Gd-Gd edges are bridged by four crystallographically distinct iodine atoms. Looking down the 3-fold axis, the three iodine atoms on the top form exo bonds to neighboring clusters and the three on the bottom bind to the isolated Gd^{III}. Of the six iodine atoms the bridge Gd-Gd bonds around the waist, three form exo bonds to neighboring clusters and the other three form part of the Cs^+ ions' cuboctahedral coordination spheres.
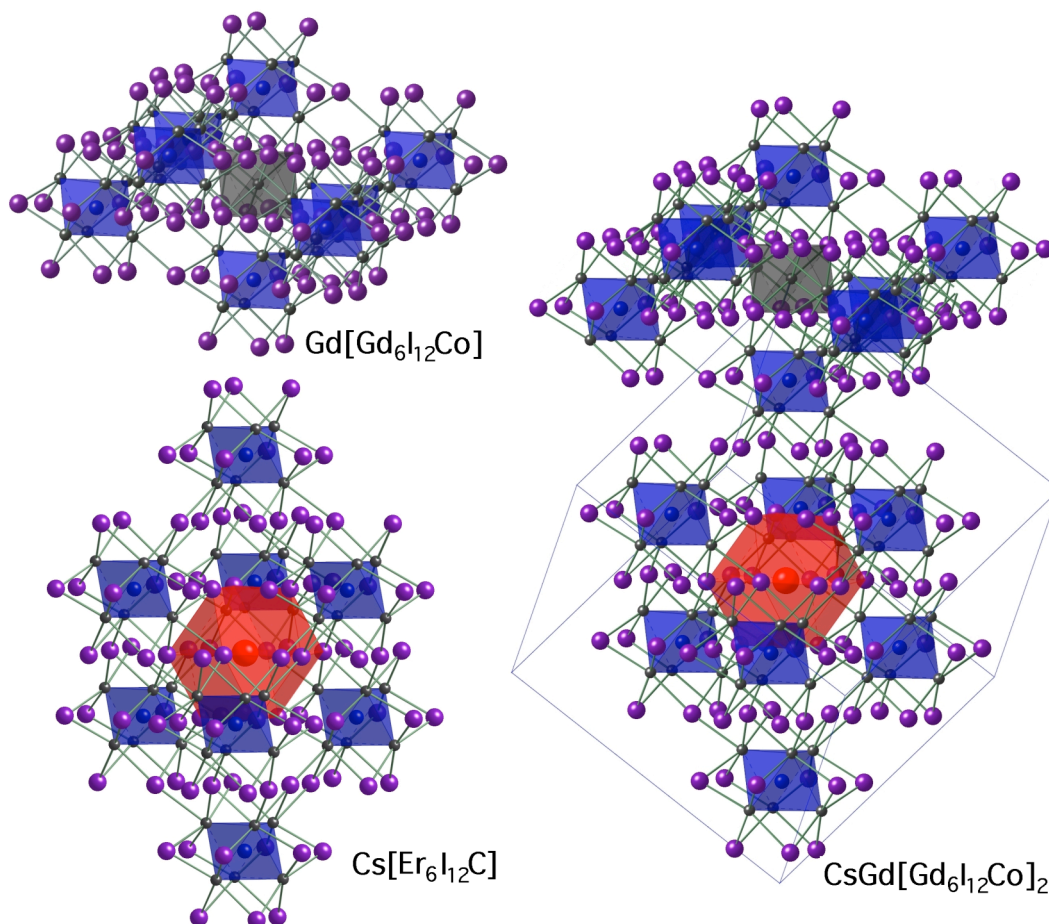
Figure 4.3. Structural relationship between $Gd[(Gd_6Co)I_{12}]$, $Cs[(Er_6C)I_{12}]$ and $CsGd[(Gd_6Co)I_{12}]_2$. The blue octahedra represent the Ln_6Z ($Z = Co$ or C) units. The red cuboctahedron is a CsI_{12} coordination polyhedron and $Gd^{III}I_6$ octahedron is grey.

Electronic Structure. Compounds of the $R[R_6ZI_{12}]$ structure type have been made with a variety of interstitial elements (Z), including several of the transition metals of Groups 7–11 and the main group atoms B, C, N – as well as C_2.[31,38,43,81,84] Interstitials are essential to the formation and stability of these clusters; formally, they provide electrons to the electron-deficient R_6 cage and engage in strong R–Z bonding that is undoubtedly much stronger than the R–R bonding. We will briefly review the bonding

scheme for these clusters to place the magnetic results in context. Figure 4.4 shows a molecular orbital diagram for the $[Gd_6ZX_{12}]$ clusters where Z is a transition metal; levels that have predominately Gd $5d$ character are displayed. In O_h symmetry, first-row transition metal interstitial $t_{2g}/e_g(3d)$ and $a_{1g}(4s)$ orbitals interact with the cluster orbitals of like symmetry to form bonds with the surrounding Gd cluster. The highest occupied t_{1u} orbital, one of which is illustrated in Figure 4.5, is predominantly delocalized over the Gd_6 cage and is only slightly stabilized by a small contribution of Z-atom $4p$ orbitals. The electronic requirements for the Gd_6Z octahedron is given in Figure 4.4; a closed-shell cluster-based-electron count of 18 applies. The closed-shell configuration is achieved when Z = Co (i.e., the compound is $Gd[Gd_6CoI_{12}]$); the HOMO is fully occupied (t_{1u}^6). $[Gd_6FeI_{12}]^{3-}$ and $[Gd_6MnI_{12}]^{3-}$ clusters have t_{1u}^5 and t_{1u}^4 HOMO configurations, respectively. By substituting Ca^{2+} for Gd^{3+} the electron count of the manganese centered cluster will go from -3 to -2 and therefore the HOMO configuration of the cluster will go from t_{1u}^4 to t_{1u}^3.
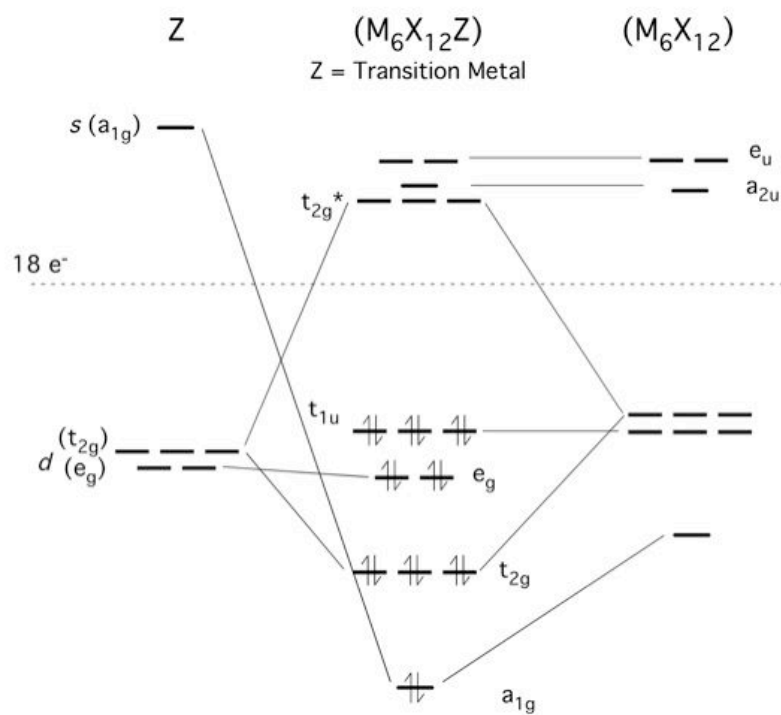
Figure 4.4. MO diagram of M_6X_{12} octahedral cluster with a transition metal element as the interstitial atom.
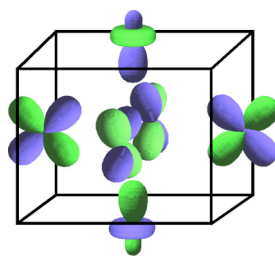
t_{1u}

Figure 4.5 One of the cluster bonding orbitals that make up the highest occupied t_{1u} set for the transition metal centered clusters.

Magnetic Susceptibilities. Syntheses of these compounds are nearly quantitative, as indicated by powder diffraction measurements. Nevertheless, their magnetic properties are highly sensitive to the presence of ferromagnetic impurities, even in small proportions. All of the samples measured were at least to some extent contaminated with ferromagnetic impurities, and it was therefore necessary to measure magnetizations over a range of applied fields to determine the extent to which such impurities contribute. Figure 4.6 illustrates the saturation of ferromagnetic impurities by increasing the applied field. Data presented below are results obtained at an applied fields of 3.5 Tesla where saturation of the ferromagnetic impurities is virtually complete and was always verified by comparison with data at lower fields.
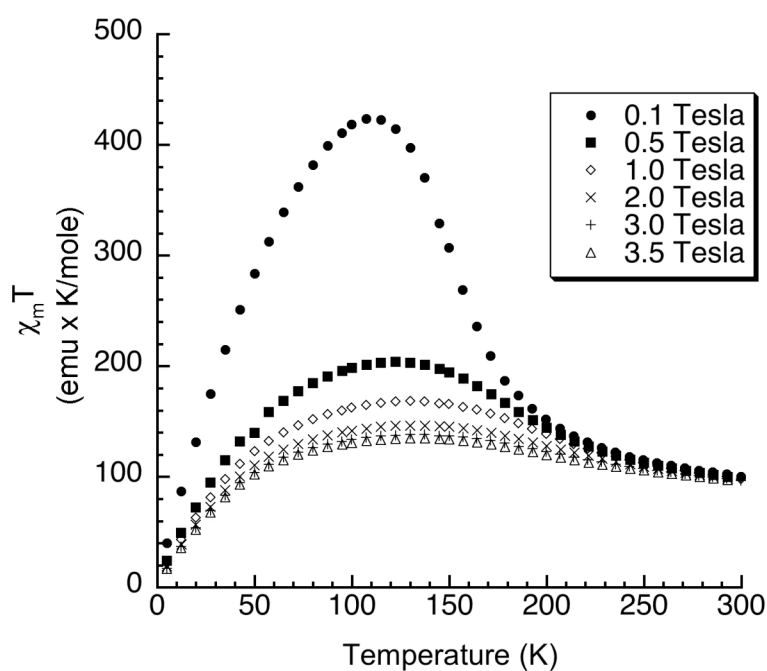
Figure 4.6. Ferromagnetic impurities are saturated by using larger applied fields; there is little difference between $\chi_m T$ at 2.0 and 3.0 Tesla.

As indicated, the Gd_6Fe and Gd_6Mn clusters respectively possess one and two unpaired electrons, primarily delocalized over the six Gd atoms. In analyzing the susceptibilities of $Gd[Gd_6ZI_{12}]$ (Z = Mn, Fe, Co), we assume that the structurally isolated Gd^{III} center makes an ideal Curie-like Gd^{III} ($S = 7/2$) contribution that can be subtracted from the total susceptibility to obtain the susceptibility contribution, $\chi(Gd_6Z)$, made by the coupled cluster network:

$$\chi(Gd_6Z) = \chi - \chi(Gd^{III})$$

To help clarify the meaning of the magnetic data for these clusters, the data are plotted as $\chi_m(Gd_6Z) \bullet T$ vs. T for the Mn-, Fe- and Co-centered $Gd[Gd_6ZI_{12}]$ compounds in Figure 4.7.

As usual for this type of plot, ideal Curie-Law behavior results in a horizontal line wherein the intercept with the ordinate yields the Curie constant, C_{molar} ($= \chi_m T$), that is related to the effective magnetic moment per cluster (μ_{eff}) via the relationship $C_{molar} = (N_A \mu_B^2 / 3k_B) \mu_{eff}^2$. In Figure 4.6, a reference line is shown for the Curie constant expected for a collection of independent Gd spins ($J = S = {}^7/_2$; and taking $g_J = 2$): $C_{Curie} = 47.25$ emu K mole^{-1}. Deviations in $\chi_m T$ from the Curie line are an indication of the net effect of magnetic coupling as a function of temperature; values below(above) the Curie line indicate that the net alignment of moments with the external field is less(more) than expected for a collection of independent moments.
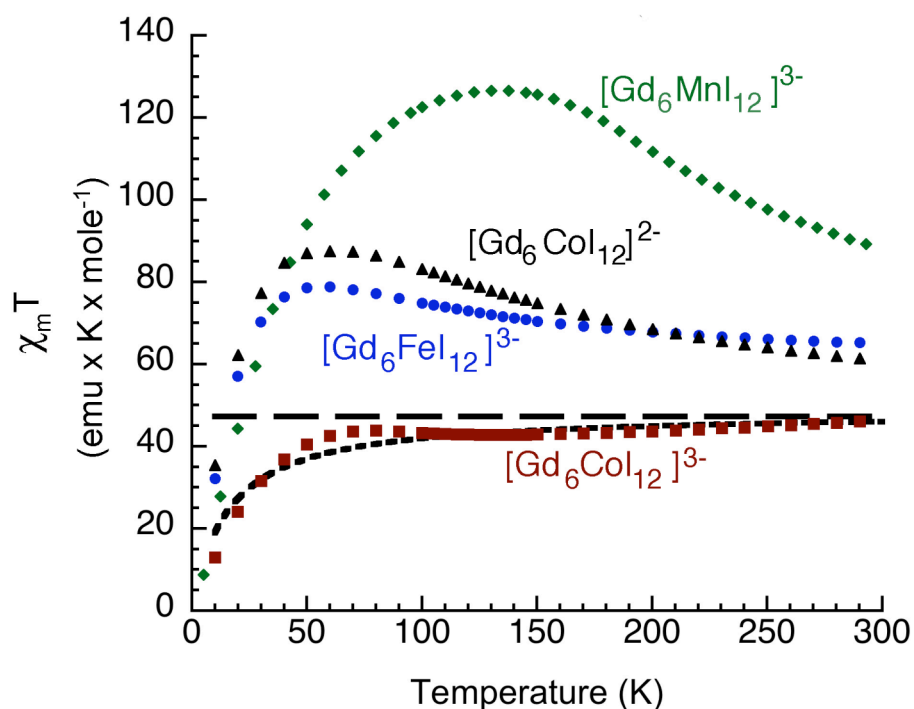
Figure 4.7. $\chi_m T$ vs. T for Gd(Gd$_6$CoI$_{12}$), Gd(Gd$_6$FeI$_{12}$), Gd(Gd$_6$MnI$_{12}$) and CsGd(Gd$_6$CoI$_{12}$)$_2$ at a 3.5 Tesla applied field, adjusted according to the equation on pg 50. χ_m(Gd^{III}) was subtracted from data for CsGd(Gd$_6$CoI$_{12}$)$_2$ and the resultant was divided by two to yield a per cluster susceptibility for [Gd$_6$CoI$_{12}$]$^{2-}$. The Curie constant (47.25 emu K mol^{-1}) for an "ideal" cluster with six uncoupled Gd^{III} centers (S = 7/2; g = 2) is shown as the long-dashed line. The Curie-Weiss fit to [Gd$_6$CoI$_{12}$]$^{3-}$ is shown as the short-dashed line.

With a susceptibility approaching Curie behavior above 100 K, Gd(Gd$_6$CoI$_{12}$) exhibits the weakest Gd–Gd exchange coupling among compounds in this series (though much larger in magnitude than normally observed for empty 5*d*-shell Gd^{III} compounds, where exchange coupling constants (*J*) are typically ~ 0.01 cm^{-1}). The Curie constant (C$_m$) obtained by fitting all the χ_m(Gd$_6$Co) data with a Curie-Weiss expression (χ_μ =

$C_m/(T-\theta)$) is 48.38 ($\pm$ 0.67) emu K mole^{-1} and the Weiss constant (θ) is -15.48 ($\pm$ 1.59) K.

There were two reasons for trying to make $Ca(Gd_6MnI_{12})$. First, the non cluster paramagnetic atom (the Gd^{3+} cation) would no longer be a contributing factor to the magnetic susceptibility observed. Second, the t_{1u} cluster valence orbitals would be half filled and therefore less susceptible to Jahn-Teller distortions. If the t_{1u} orbitals distort those unpaired electrons (if not paired by the lowering of symmetry) may not be delocalized over all six cluster Gd atoms.

The only correction made on the magnetic susceptibility data plotted in Figure 4.8 was for the diamagnetic contribution of the sample holder (plastic straw and bag). The subtraction of the paramagnetic contribution of the non cluster Gd^{3+} cation was not done to the data plotted in Figure 4.8 because the Ca:Gd ratio is not known for the compounds that contain both cations. In order to plot $\chi_m T$ as in Figure 4.7, the molar mass of the compounds would have to be known. The molar mass of the compounds is not known for the mixed cation compounds, therefore $\chi_g T$ was plotted in Figure 4.8. The uncertainty of the Ca:Gd ratio also causes a problem for determining the diamagnetic core corrections. The purpose of Figure 4.8 is to compare the temperature dependence of $\chi_g T$ for $Gd(Gd_6MnI_{12})$ to that of the mixed cation compounds.
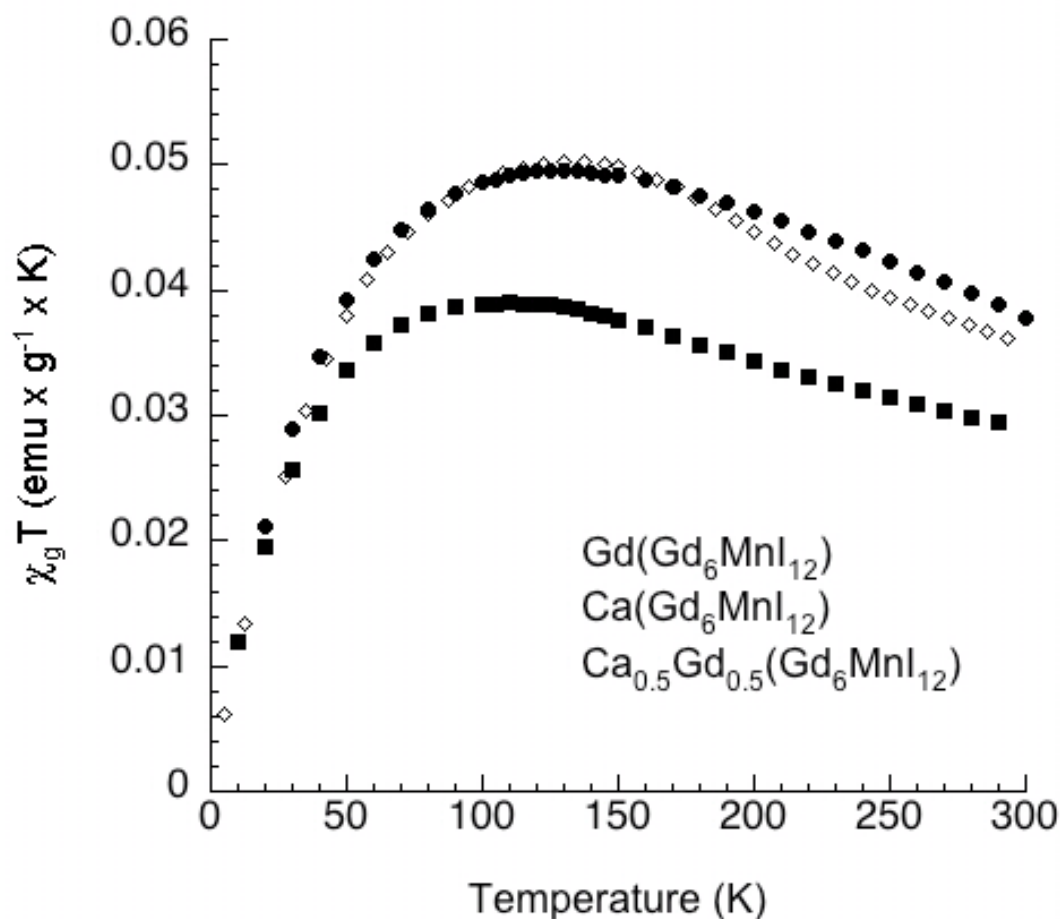
Figure 4.8. $\chi_g T$ vs. T plot for reactions loaded to make $Gd(Gd_6MnI_{12})$, $Ca(Gd_6MnI_{12})$ and $Ca_{0.5}Gd_{0.5}(Gd_6MnI_{12})$. The Ca:Gd ratio for the latter two samples was only qualitatively determined via powder x-ray diffraction.

Magnetism: Interpretation and Computational Results. The effective magnetic moment per cluster is increased considerably for the $[Gd_6FeI_{12}]^{3-}$ and $[Gd_6MnI_{12}]^{3-}$ systems in comparison with the compound with Co-centered clusters. This is attributable to relatively strong exchange interactions between the unpaired electrons

in the HOMO and the electrons in the $4f$ orbitals. Neither compound yields a susceptibility that is well described by a Curie-Weiss fit, but it is clear that above 50 K the effects of ferromagnetic coupling dominate the data's departure from independent-moment behavior. The 16-electron $[Gd_6MnI_{12}]^{3-}$ cluster, having two holes in the HOMO, exhibits a significantly larger susceptibility over the entire measured temperature range than the 17-electron (one hole) $[Gd_6FeI_{12}]^{3-}$ system. All of these systems show the effects of substantial antiferromagnetic coupling at the lowest temperatures.

The clusters in $CsGd(Gd_6CoI_{12})_2$ possess 17 electrons for metal-metal bonding, and this compound therefore offers a useful control for our implicit hypothesis concerning the influence of open-$5d$-shell character on the magnetic properties of these compounds. Although these clusters are Co-centered, the cluster charge is –2, so they are isoelectronic with the Fe-centered clusters in $Gd(Gd_6FeI_{12})$, which have a cluster charge of –3. Figure 4.7 shows that the susceptibilities for the isoelectronic systems are indeed similar.

When there is only one hole in the HOMO as with the Fe centered cluster, it may be a break in the degeneracy of the three orbitals that causes incomplete delocalization of the hole. This may be why we observe an effective magnetic moment lower than expected for complete ferromagnetic coupling. With the 16 electron case, $Gd(Gd_6MnI_{12})$, having two holes there is a larger magnetic moment per cluster, but still not as large as expected for a $S = 44/2$ cluster.

Substituting Ca^{2+} in the Gd^{3+} cation site did not substantially enhance the magnetic moment per cluster. In the case of the sample loaded to make $Ca_{0.5}Gd_{0.5}(Gd_6MnI_{12})$ the magnetic moment per cluster was lower than $Gd(Gd_6MnI_{12})$ at temperatures above 50 K. No further interpretation of the temperature dependent magnetic susceptibility of $Ca_xGd_{1-x}(Gd_6MnI_{12})$ compounds due to the uncertainty of the degree of Ca substitution.

As indicated in our earlier qualitative remarks, the strong intracluster coupling is attributed to the presence of appreciable unpaired spin-density in metal-metal bonding electrons that are delocalized over the six metal atoms of the cluster. The clusters in these compounds are not structurally isolated, and hence intercluster coupling has an important effect on these compounds' magnetic properties. Lindsay Roy, a former member of the Hughbank's research group, had constructed two structural models $[Gd_6CoI_{12}](OPH_3)_6$ and $[Gd_6CoI_{12}]_2(OPH_3)_{10}$ (shown in Figure 4.9) to evaluate the relative energies of various spin configurations using DFT calculations.[85]
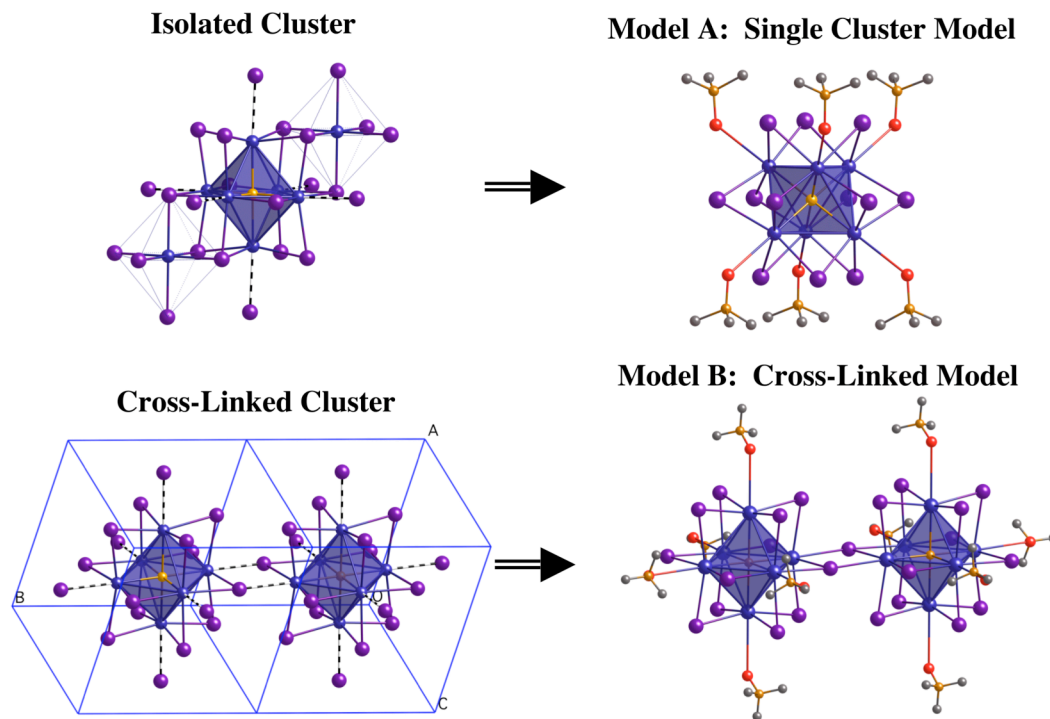
Figure 4.9. Relationship between single cluster model (A) and cross-linked model (B) and parent $Gd(Gd_6ZI_{12})$ structure.

Lindsay Roy performed electronic structure calculations on $[Gd_6CoI_{12}](OPH_3)_6$ to interpret the *intercluster* magnetism of these compounds. By calculating a series of spin patterns for the $[Gd_6CoI_{12}](OPH_3)_6$ model (shown in Figure 4.10) using DFT, it was found that the lowest energy spin pattern is that with all of the 4*f* spins aligned parallel to the spins of the three valence CBEs, the latter of which are spin-up in all calculations. If the Gd 4*f* moments are successively "flipped," the energy increases in steps of ~1480 cm^{-1} (range: 1380–1600 cm^{-1}) for each Gd moment flipped.[85]
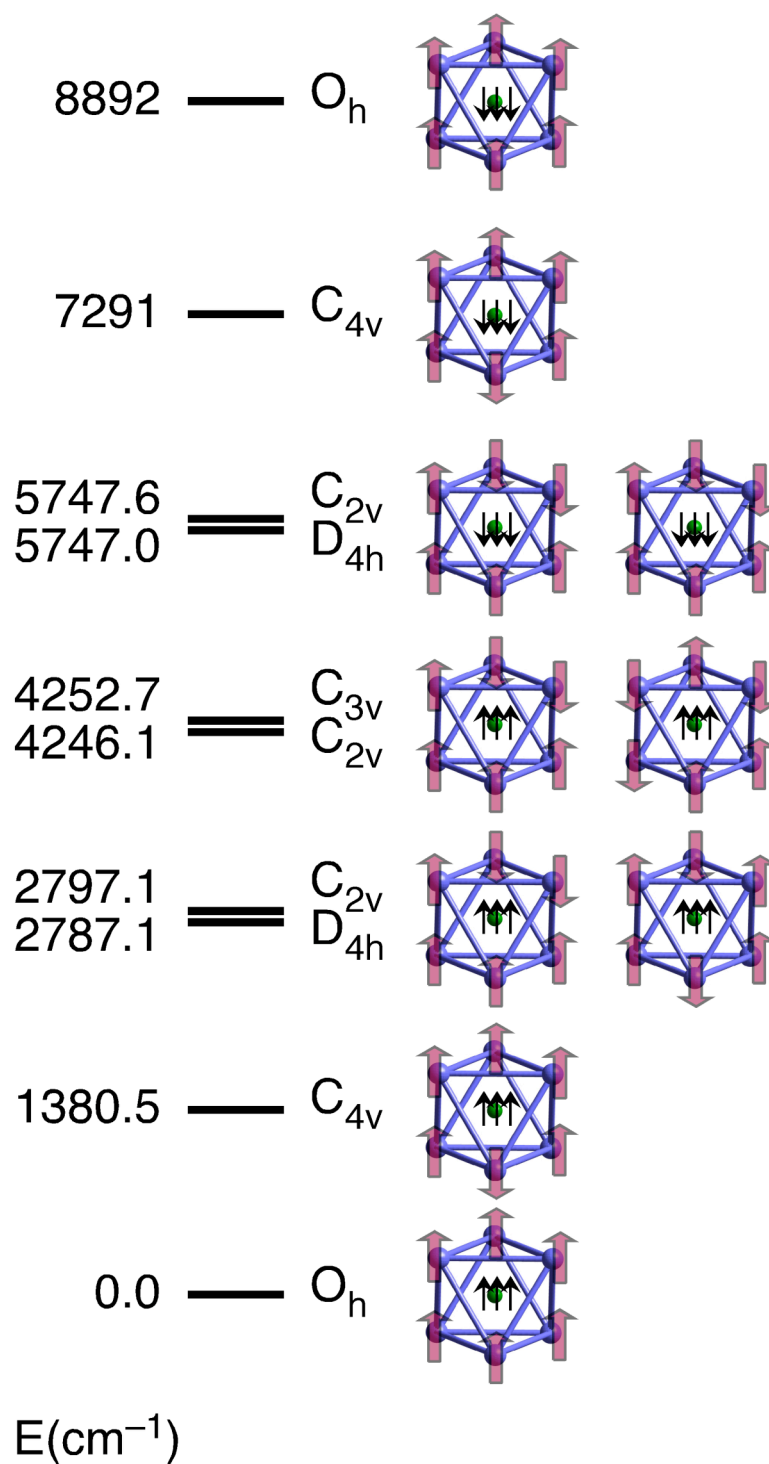
Figure 4.10. 10 spin patterns and energies for the model $[Gd_6CoI_{12}](OPH_3)_6$.

In order to estimate the magnitude of *inter*cluster coupling, Lindsay Roy performed two calculations using the model $(Gd_6CoI_{12})_2(OPH_3)_{10}$, which maintains the intercluster bonding found in the solid state compound. Since the difference between the ferromagnetically coupled single cluster and the next lowest spin state was ~1400 cm^{-1}, we only considered the cross-linked models that contain *intra*cluster ferromagnetic coupling, assuming all other configurations will be much higher in energy. Figure 4.11 illustrates the energy difference between $S = 45$ and $S = 0$ in the cross-linked cluster model, which is 50 times weaker than intracluster couplings. The intercluster coupling favors antiferromagnetic spin alignment between clusters and an expected suppression of the susceptibility at low temperature.
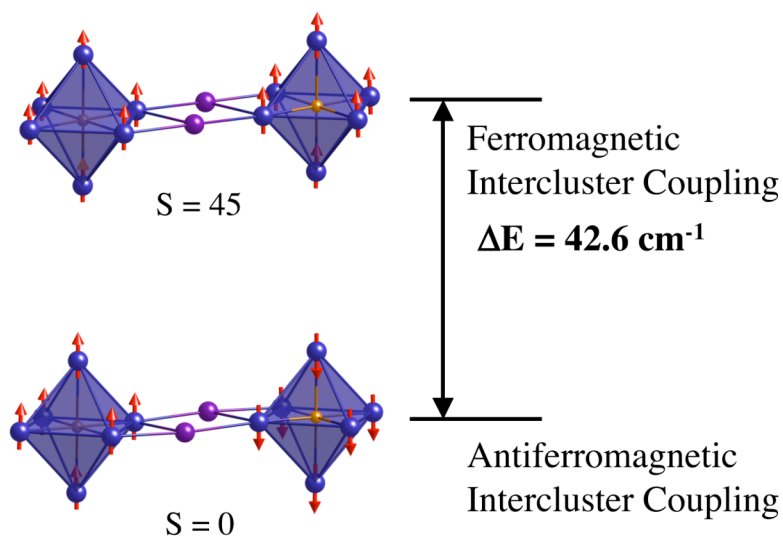
Figure 4.11. Energy difference between $S = 0$ and $S = 45$ for the cross-linked model.

Conclusions

Study of the homologous series of compounds, $Gd(Gd_6ZI_{12})$ (Z = Co, Fe, Mn) demonstrates the efficacy with which unpaired, delocalized Gd–Gd bonding electrons can couple the spins localized in the $4f$ orbitals of the Gd atoms. Because of the strong exchange interactions between the electrons localized in the $4f$ orbitals in Gd and the valence ($5d$ and $6s$) electrons, strong magnetic communication can occur. The similarity in the temperature dependent susceptibility of the isoelectronic compounds, $Gd(Gd_6FeI_{12})$ and $CsGd(Gd_6CoI_{12})_2$ supports our contention that the magnetic properties of these compounds are largely dependent on the local electronic structure of the cluster and are less dependent on the structure of the extended network.

$Gd(Gd_6MnI_{12})$, $Gd(Gd_6FeI_{12})$ and $CsGd(Gd_6CoI_{12})_2$ all showed larger temperature dependent magnetic susceptibilities than $Gd(Gd_6CoI_{12})$, which has a closed shell cluster HOMO. However the magnitude of the susceptibilities were not as large as expected for a complete coupling of the magnetic moments of all the Gd atoms in the cluster. The lower than ideal magnetic susceptibility may, in part, be due to incomplete delocalization of the hole in the cluster HOMO caused by a break in the degeneracy of these orbitals. DFT calculations suggest that intercluster magnetic coupling is also significant. Structural isolation of the clusters will help to decipher the contributions of intra- vs. intercluster coupling and would pave the way to an interesting class of molecular magnets in compounds appropriately doped with lanthanide elements other than gadolinium.

CHAPTER V

SYNTHESIS STRUCTURE AND MAGNETIC PROPERTIES OF DICARBIDE

CENTERED HEXANUCLEAR Gd CLUSTERS[*]

Introduction

In the previous chapter the ferromagnetic coupling of transition metal centered hexanuclear Gd cluster compounds was demonstrated with a series of Gd_6ZI_{12} cluster containing compounds. In this chapter the ferromagnetic coupling present in $Cs(Gd_6C_2I_{12})$ is demonstrated. Density functional theory (DFT) and extended Hückel (EH) calculations were used to support the proposed mechanism for intracluster ferromagnetic coupling and to make predictions on the magnetic properties of the other dicarbide centered clusters reported here, $Gd_6C_2I_{11}$, $Gd(Gd_6C_2I_{12})$ and $CsGd(Gd_6C_2I_{12})_2$.

The purpose of trying to make hexanuclear gadolinium cluster compounds with carbon interstitials was to study the magnetic properties of $Gd(Gd_6CI_{12})$[45] and hopefully a gadolinium analogue of $Cs(Er_6CI_{12})$.[49,50] Previously there were nine known structure types (differentiating between mono and dicarbed centered clusters) that contain structurally isolated R_6 (R = rare earth) clusters centered by carbon atom(s) $Cs_2(LuCl_6)(Lu_6CCl_{12})$,[49] $Cs_4(Pr_6C_2I_{13})$,[54] $Cs_4(Sc_6CCl_{13})$,[54] $Cs_2(Pr_6C_2I_{12})$,[52] $Rb(Pr_6C_2I_{12})$,[48] $Cs(Er_6CI_{12})$,[49,50] $R(R_6CI_{12})$ (R = Sc, La, Ce, Pr, Gd, Tb, Er),[45,46] $Sc_6C_2I_{11}$,[36] $R_6C_2I_{10}$ (R = La, Ce).[34] In this chapter four new compounds are presented, which fall into the category of structurally isolated R_6 iodide clusters centered by carbon atoms. $Gd_6C_2I_{11}$ and $Cs(Gd_6C_2I_{12})$ crystallize in the $Sc_6C_2I_{11}$ and $Rb(Pr_6C_2I_{12})$ structure types respectively. $Gd(Gd_6C_2I_{12})$ and $CsGd(Gd_6C_2I_{12})_2$ crystallize in structure types similar to the transition

metal centered $R(R_6ZI_{12})$ and $CsR(R_6CoI_{12})_2$ respectively, however, the dicarbide interstitial distorts the octahedral shape of the Gd_6 clusters.

Experimental Section

    Synthesis. Due to the air and moisture sensitivity of the reactants and products, all compounds were handled in nitrogen filled glove boxes or in high vacuum lines. Reactants were loaded into Nb reaction tubes, welded closed under a partial pressure of Ar and then sealed in evacuated silica jackets. Gd metal ingots used were from Stanford Materials (99.95% REM) unless otherwise indicated, in which case the source was Ames Laboratory (99.999% including nonmetals). Turnings of these metals were obtained by drilling the ingots in a glovebox using a tungsten carbide drill bit. GdI_3 was prepared by reaction of Gd turnings with HgI_2 (Strem 98%) as described in the literature,[62] then sublimed at least three times. Graphitic carbon (Alfa Aesar 99.9%) was heated under vacuum at 900ºC for 24 hours. CsI (Aesar 99%) was sublimed under dynamic vacuum before use. All reactants were stored in evacuated, sealed ampoules until their use.

    The crystals used in the structure determination of $Gd_6C_2I_{11}$, $Gd(Gd_6C_2I_{12})$ and $CsGd(Gd_6C_2I_{12})_2$ were all obtained from reactions loaded with CsI, GdI_3, Gd metal and graphitic carbon, but combined in molar ratios that weren't those of the target compounds. Crystals that were subsequently used to determine the $CsGd(Gd_6C_2I_{12})_2$ structure were obtained from two different reaction tubes loaded with the target composition "$Cs(Gd_6C_2I_{12})$" that had been heated in a 850-830ºC temperature gradient. The structure determined from the better of the two x-ray diffraction data sets is reported here. The crystals used in the structure determinations of $Gd_6C_2I_{11}$ and $Gd(Gd_6C_2I_{12})$ were selected from the products of two reactions that had been loaded to target

CsGd(Gd$_6$C$_2$I$_{12}$)$_2$ – heated in a 900-880ºC temperature gradient. Attempts to improve the yields of these syntheses are discussed below.

Gd(Gd$_6$C$_2$I$_{12}$) was synthesized by loading Gd (Ames Lab), GdI$_3$ and graphitic carbon in a 3:4:2 molar ratio, heating to 900ºC for 20 days, then cooling at a rate of 18ºC/hr to ambient temperature. The powder pattern of this black powder product indicated the presence of GdI$_3$ and GdOI in small quantities (~5% each) in addition to the intended product. The presence of Gd$_6$C$_2$I$_{11}$ was not observed in the powder pattern. Attempts to make this compound at temperatures lower than 900ºC (875ºC, 850ºC and 840ºC) yielded GdI$_3$, GdOI and an unidentified phase (or phases).

Gd$_6$C$_2$I$_{11}$ was made by loading a Nb tube with Gd (Ames Lab), GdI$_3$ and graphitic carbon in a 7:11:6 molar ratio and heating to 900ºC for 16 days and then slowly cooling to room temperature at a rate of 18ºC/hr. The powder pattern of this reaction indicated that Gd$_6$C$_2$I$_{11}$ was the major phase, contaminated with (~5% each) GdOI and GdI$_3$. No Gd(Gd$_6$C$_2$I$_{12}$) was detected.

Several attempts were made to improve the synthetic yield of CsGd(Gd$_6$C$_2$I$_{12}$)$_2$. Reactions were conducted at temperatures ranging from 750ºC to 900ºC for times ranging from 16 to 24 days. The major phases observed in the powder patters ranged from CsGd$_6$C$_2$I$_{12}$, CsGd$_{10}$C$_4$I$_{18}$ and/or Gd(Gd$_6$C$_2$I$_{12}$). Reaction conditions that resulted in the formation of CsGd(Gd$_6$C$_2$I$_{12}$)$_2$ as more than a minor phase could not be found.

A crystal of CsGd$_6$C$_2$I$_{12}$ was picked form a reaction loaded with CsI, GdI$_3$, graphitic carbon and Gd metal (Ames lab) in a ratio that targeted the already established composition (3:11:6:7). The reported structure was obtained from a crystal that was retrieved from a reaction that was heated to 825ºC for 16 days. The powder pattern of this sample indicated the product was phase pure, but a small, light gray fraction of the product was visible, but presumably amorphous. A quantitative yield, as indicated by

powder x-ray diffraction and visual inspection, was obtained from a reaction loaded stoichiometrically for $CsGd_6C_2I_{12}$ and heated to 800ºC for 20 days. The crystals picked from this latter reaction exhibited severe twinning problems. The magnetic measurements reported here were collected on this latter sample.

X-ray Structure Determination. For $Gd(Gd_6C_2I_{12})$, $CsGd(Gd_6C_2I_{12})_2$ and $Cs(Gd_6C_2I_{12})$, single-crystal x-ray diffraction data was collected on a Bruker, APEX II CCD diffractometer equipped with graphite-monochromated Mo K_α radiation source (λ = 0.71073 Å). A Bruker, SMART 1000 CCD diffractometer equipped with graphite monochromated Mo K_α radiation source were used to collect single crystal diffraction data on $Gd_6C_2I_{11}$. All crystals were mounted onto nylon loops using Apiezon[®] N grease and then placed under a cold N_2 stream (−163 ˚C) for data collection. Frame data were indexed using the APEX II software package[68] and the peak intensities were integrated using the SAINT program.[69] The faces of all the crystals, excluding $Gd_6C_2I_{11}$, were indexed using the scope interface software of the APEX II package and absorption corrections were made using SADABS software.[70] The SHELXTL software package[71] was used as an interface to the SHELX-97 suite of programs,[72] which was used to implement structure solutions by direct methods and full-matrix least-squares structural refinements on F^2.

Several attempts to obtain a single crystal structure of $CsGd_6C_2I_{12}$ were made. All but the last data set collected resulted in structure solutions that exhibited symptoms of twinning and/or disorder that seem to plague this class of C_2-centered cluster compounds. The last crystal mounted was black, multifaceted with dimensions $0.07 \times 0.06 \times 0.05$ mm^3. A total of 21,050 reflections were collected ($4.52 \leq 2\theta \leq 69.72°$) and indexed to the $P\overline{1}$ space group. This resulted in 6,071 unique reflections after

averaging redundant data. The final anisotropic refinement of all atoms resulted in a $R_1=0.0312$ and $wR_2 = 0.0599$ for all data.

A black crystal of $Gd(Gd_6C_2I_{12})$ with the dimensions $0.23 \times 0.19 \times 0.13$ mm^3 was mounted on a diffractometer and 20,320 reflections were collected ($4.98° \leq 2\theta \geq 70.66°$) to give 2,055 unique for the space group $R\overline{3}$ (No. 148). Initially this data set was indexed with the unit cell $a,b = 30.7086(8)$ $c = 10.3645(5)$ in the $R\overline{3}$ space group. The refined structure was essentially just a $2 \times 2 \times 1$ supercell ($Z=12$) derived from the typical 7-12 structure type ($Z=3$ in the hexagonal setting). The carbon atoms could not be located and there were significant residual peaks (5-6 e$^-$/Å^3) located 0.5 Å from each of the cluster Gd atoms.

This initially indexed supercell was thought to be a possible indication of long range ordering of dicarbides. The R_1 value was 0.1037 and there was no indication from the refinement of the SOF or thermal displacement parameters that suggest an ordering in the supercell that did not exist in the smaller Z=3 unit cell. Lower symmetry space groups were tested, but no long-range ordering model emerged that would justify the use of the larger cell. The data were therefore reindexed using a larger number of reflections (1,375) and a unit cell consistent with the usual 7-12 structure was suggested by the indexing program that is a part of the APEX II package,[68] $a = 15.3599(3)$ Å, $c = 10.3676(3)$ Å, $R\overline{3}$, Z=3. The structure was solved and refined to have the usual 7-12 structure, and the carbon interstitial atoms were easily located. The residual Fourier peaks that were 0.5 Å from the cluster Gd atoms were still present in this refinement. A disorder model that satisfactorily accounted for the residual peaks is described in detail in the discussion section.

We note here that there were 173 out of 20,320 total reflections in the doubled unit cell which had been indexed to an odd h or k with an intensity larger than 3 $\sigma(I)$

before averaging. All reflections where h or k was odd had an intensity less than 10 $\sigma(I)$. Because of the small number and low intensity of these reflections, and the lack of any noticeable characteristics in the structure solution that revealed longer range ordering that would require the doubled unit cell, the smaller unit cell was chosen. With the smaller unit cell the R_1 and wR_2 were 0.0375 and 0.0863 respectively. It is possible that in a more extensive investigation, perhaps by use of electron diffraction, the origin of these subtle anomalies could be revealed.

A black crystal of $Gd_6C_2I_{11}$ with the dimensions $0.17 \times 0.11 \times 0.09$ mm^3 was mounted on the diffractometer and 38,172 reflections were collected ($2.86° \leq 2\theta \leq 70.68°$) to give 10,883 unique for the space group $P\bar{1}$ (No. 2). The initial solution appeared to contain Gd_6 clusters but the presence of an inversion center resulted unreasonable interatomic distances for one of the clusters. The structure solution in the P1 space group resulted in a crystal structure that looked very similar to the one reported here and yielded a $R_1 = 0.0488$ ($I>4\sigma(I)$) for an anisotropic refinement of all atoms. When checking for additional symmetry, the program *Platon* suggested the correct space group was $P\bar{1}$. The structure coordinates generated by *Platon* were entered into SHELX and refined. The final structure solution of $Gd_6C_2I_{11}$ was void of the problems that plagued the initial $P\bar{1}$ solution. The results of this refinement is the final structure reported here with $R_1 = 0.0715$ and $wR_2 = 0.1178$ for all reflections. Very similar difficulties were described by Dudis and Corbett in structural determination of $Sc_6C_2I_{11}$, the only other compound that adopts this structure type.[36]

A black crystal of $CsGd(Gd_6C_2I_{12})_2$ with the dimensions $0.14 \times 0.10 \times 0.08$ mm^3 was mounted on the diffractometer and 119,282 reflections were collected ($2.20° \leq 2\theta \leq$

69.42º) to give 4,338 unique for the space group $Pa\bar{3}$ (No. 205). The crystal structure was initially refined as isotypic with $CsEr(Er_6Co_2I_{12})_2$ – without an appreciable distortion to the octahedral Gd_6 cages and only one carbon atom residing in the center of each cage. This initial structure solution was inadequate in several respects: (1) There were 689 reflections that were systematic absence violations for the $Pa\bar{3}$ space group, but all reflections were well indexed; (2) The isotropic displacement parameters for the carbon atom were near zero and could not be refined anisotropically; (3) There were significant residual Fourier peaks (43 and 48 $e^-/Å^3$) located about 0.5 Å away from the cluster Gd atoms.

The systematic absence violations were attributed to the presence of merohedral twinning. The TwinRotMat program as implemented in Platon[77] suggested a twin law discussed later and illustrated in on page 81. The twin law was entered into the least squares refinement and all the systematic absence violations were accounted for; the R_1 value was reduced from 0.249 to 0.066. The two twin components were refined to 59:41 ratio. Because the centers of clusters (i.e., the erstwhile C atom position) in this structure (and in most other cluster-based compounds of this type)[32] effectively reside on a site in the iodine sublattice, it is common in twinned crystals to find spurious electron density peaks in the cluster interstices. This accounts for the very small displacement parameter for the carbon atom prior to the inclusion of the twin law in the refinement; indeed, the refinement of the twin law did not fully remove the residual Fourier peak in the center of the cluster that was 15.09 $e^-/Å^3$.

The clusters in this structure reside on 3-fold axes and disordering of the dicarbide units on the three nominal 4-fold cluster axes (as in $Gd(Gd_6C_2I_{12})$ and as

shown in figure on page 79) accounts for the residual Fourier peaks located near the cluster Gd atoms. The same site occupancy constraints used for $Gd(Gd_6C_2I_{12})$ were used here. The final R_1 value was 0.0659 ($I>2\sigma(I)$). There is also a peak (12.5 $e^-/Å^3$) that generates a trigonal antiprism surrounding the Cs atom at a distance of 3.0 Å.

A second data set was collected on a different crystal of $CsGd(Gd_6C_2I_{12})_2$. While the second data set refined to yield a nearly identical structure as the one reported here, there were 13 systematic absence violations in the $Pa\overline{3}$ space group, which resulted in 7,285 out of 156,918 reflections being rejected. When the twin law that was applied to the structure reported here was applied to the second data set the fractional twin component parameter would reduce to a small negative number and the structure refinement became unstable. The final R_1 value for the refinement (no twin law applied) of this second data set was 0.0702 ($I>2\sigma(I)$). The residual peaks in the center of the clusters and around the Cs atom were 11.49 and 10.31 $e^-/Å^3$ respectively. As with the first data set, the C atoms could not be refined anisotropically in the second data set.

A summary of the crystallographic data for these four compounds is shown in Tables 5.1 and 5.2. Interatomic distances are shown in Table 5.3. The generic labeling for the interatomic distance table is illustrated in Figure 5.1.

Table 5.1. Crystallographic data for $Gd_6C_2I_{11}$, $Gd(Gd_6C_2I_{12})$, $CsGd(Gd_6C_2I_{12})_2$ and $Cs(Gd_6C_2I_{12})$

	$Gd_6C_2I_{11}$	$Gd(Gd_6C_2I_{12})$	$CsGd(Gd_6C_2I_{12})_2$	$Cs(Gd_6C_2I_{12})$
fw (g/mol)	2363.42	2647.57	5246.78	2623.23
crystal size (mm^3)	0.17×0.11×0.09	0.23×0.19×0.13	0.14×0.10×0.08	0.07×0.06×0.05
crystal system	Triclinic	Rhombohedral	Cubic	Triclinic
space group, Z	$P\bar{1}$ (No. 2), 2	$R\bar{3}$ (No. 148), 3	$Pa\bar{3}$ (No. 205), 4	$P\bar{1}$ (No. 2), 1
unit cell dimensions (Å°)	a=9.4123(3), b=10.4059(3), c=14.7645(5) α=87.800(1)°, β=75.713(1)°, γ=69.381(1)°	a=15.3599(3) c=10.3676(5)	a=18.055(3)	a = 9.3345(5), b = 9.3730(5), c = 9.7596(2) α= 71.556(2)°, β= 72.487(1)°, γ = 72.525(1)°
volume ($Å^3$)	1309.72(7)	2118.29(12)	5885.3(17)	752.37(7)
density (calculated)	5.993 mg/cm^3	6.226 mg/cm^3	5.921 mg/cm^3	5.790 mg/cm^3
abs. coeff	27.923 mm^{-1}	29.300 mm^{-1}	27.623 mm^{-1}	26.525 mm^{-1}
2θ range	2.86 to 70.68°	4.98 to 70.66°	3.20 to 69.42°	4.52 to 69.72°
index ranges	-15≤h≤14, -16≤k≤16, -23≤l≤23	-24≤h≤24, -24≤k≤24, -16≤l≤16	-23≤h≤28, -28≤k≤28, -28≤l≤28	-14≤h≤14, -15≤k≤14, -15≤l≤15
total no. reflns	38,172	20,320	119,282	21,050

Table 5.1 Continued

	$Gd_6C_2I_{11}$	$Gd(Gd_6C_2I_{12})$	$CsGd(Gd_6C_2I_{12})_2$	$Cs(Gd_6C_2I_{12})$
independent reflns [R_{int}]	10,883 [0.0568]	2,055 [0.0672]	4,338 [0.0881]	6,071 [0.0264]
$R_1{}^a$, wR_2 [$I>2\sigma(I)$]	0.0452, 0.1036[b]	0.0375, 0.0863[c]	0.0659, 0.1650[d]	0.0270, 0.0586[e]
$R_1{}^a$, wR_2 (all data)	0.0715, 0.1178[b]	0.0514, 0.0952[c]	0.1065, 0.2056[d]	0.0312, 0.0599[e]
goodness-of-fit on F^2	1.044	1.048	1.001	1.132

[a]$R_1 = \sum||F_o|-|F_c||/\sum|F_o|$. [b,c,d,e] $wR_2 = [\sum[w(F_o{}^2-F_c{}^2)^2]/ \sum[w(F_o{}^2)^2]]^{1/2}$, where [b]$w = 1/\sigma^2(F_o{}^2)+(0.0474P)^2+18.1621P$], [c]$w = 1/\sigma^2(F_o{}^2)+(0.0360P)^2+126.6520P$], [d]$w = 1/\sigma^2(F_o{}^2)+(0.1083P)^2+43.8050P$] and [e]$w = 1/\sigma^2(F_o{}^2)+(0.0205P)^2+4.1644P$]

Table 5.2. Atomic coordinates and equivalent isotropic displacement parameters ($Å^2 \times 10^3$) for $Gd_6C_2I_{11}$, $Gd(Gd_6C_2I_{12})$, $CsGd(Gd_6C_2I_{12})_2$, $Cs(Gd_6C_2I_{12})$

atom	Wyck.	x	y	z	$U_{eq}{}^a$	occ.
			$Gd_6C_2I_{11}$			
Gd(1)	2i	0.37829(4)	0.06803(4)	0.86841(3)	4.78(8)	1
Gd(2)	2i	0.62155(5)	-0.03016(4)	0.62020(3)	6.12(8)	1
Gd(3)	2i	0.16509(4)	0.14633(4)	0.70103(3)	5.30(8)	1
Gd(4)	2i	0.62950(4)	-0.35447(4)	0.40343(3)	4.97(8)	1
Gd(5)	2i	0.57993(4)	0.28370(4)	0.76727(3)	4.96(8)	1
Gd(6)	2i	0.13584(4)	0.45445(4)	0.84814(3)	6.21(8)	1
I(1)	2i	0.88606(1)	0.05426(5)	0.64937(4)	8.3(1)	1
I(2)	2i	0.37064(6)	-0.13041(5)	0.56670(3)	5.66(9)	1
I(3)	2i	0.86469(6)	0.37523(5)	0.80896(4)	8.0(1)	1
I(4)	2i	0.87212(6)	-0.29149(5)	0.48254(3)	6.5(1)	1
I(5)	2i	0.63014(6)	0.12265(6)	0.94167(4)	7.8(1)	1
I(6)	2i	0.87821(6)	-0.62912(5)	0.32111(4)	7.6(1)	1
I(7)	2i	0.62470(6)	-0.21039(5)	0.78043(4)	8.0(1)	1
I(8)	2i	0.12887(6)	-0.04395(5)	0.85456(4)	8.0(1)	1
I(9)	2i	0.38391(6)	0.54142(5)	0.89424(4)	8.5(1)	1
I(10)	2i	0.36905(6)	-0.46248(5)	0.40109(4)	7.8(1)	1
I(11)	2i	0.12196(6)	0.28340(5)	0.02390(4)	8.2(1)	1
C(1)	2i	0.3147(9)	0.2710(9)	0.7606(6)	9(2)	1
C(2)	2i	0.4348(9)	0.1522(8)	0.7027(5)	5(1)	1
			$Gd(Gd_6C_2I_{12})$			
Gd(11)	18f	0.1880(2)	0.5625(1)	0.0297(2)	5.8(3)	0.690(9)
Gd(12)	18f	0.1590(4)	0.5411(3)	0.0049(3)	6.6(5)	0.310(9)
Gd(2)	3a	1/3	2/3	-1/3	33.4(3)	1
I(1)	18f	0.02121(3)	0.58725(3)	0.16526(4)	11.6(1)	
I(2)	18f	0.19911(3)	0.71984(3)	-0.17035(4)	9.6(1)	1
C	18f	0.2914(12)	0.6392(12)	0.1271(16)	4(3)	0.310(9)

Table 5.2 Continued

Atom	Wyck.	x	y	z	$U_{eq}{}^{a}$	occ.
			$CsGd(Gd_6C_2I_{12})_2$			
Gd(11)	24d	0.1689(1)	0.3321(1)	0.5326(2)	13.5(4)	0.64(1)
Gd(12)	24d	0.1704(2)	0.3330(2)	0.5074(5)	16.8(7)	0.64(1)
Gd(21)	24d	0.3032(2)	0.3319(1)	0.66683(9)	14.8(4)	0.36(1)
Gd(22)	24d	0.3288(5)	0.3315(2)	0.6666(2)	19.0(7)	0.36(1)
Gd(3)	4a	0	1/2	1/2	24.9(3)	1
I(1)	24d	0.33821(5)	0.33276(4)	0.83554(4)	21.7(2)	1
I(2)	24d	0.00222(5)	0.66902(3)	0.50308(3)	15.9(2)	1
I(3)	24d	0.33653(6)	0.33487(5)	0.49985(4)	19.2(2)	1
I(4)	24d	0.16568(6)	0.16356(5)	0.49790(4)	22.6(2)	1
Cs	4b	1/2	1/2	1/2	32.6(2)	1
C(1)	24d	0.1691(14)	0.3352(14)	0.7085(12)	10(4)	0.36(1)
C(2)	24d	0.1684(16)	0.3723(14)	0.6726(16)	15(4)	0.36(1)
			$Cs(Gd_6C_2I_{12})$			
Gd(1)	2i	0.60864(2)	0.47049(2)	0.19051(2)	5.94(5)	1
Gd(2)	2i	0.53005(2)	0.76769(2)	0.40962(2)	5.72(5)	1
Gd(3)	2i	0.23222(2)	0.58961(2)	0.47684(2)	5.64(5)	1
I(1)	2i	0.65256(4)	0.79851(3)	0.07252(3)	9.29(6)	1
I(2)	2i	0.43161(3)	0.86809(3)	0.70998(3)	9.44(6)	1
I(3)	2i	0.27370(3)	0.58004(4)	0.14321(3)	9.58(6)	1
I(4)	2i	0.06022(3)	0.65197(4)	0.78357(3)	9.13(6)	1
I(5)	2i	0.13361(3)	0.28138(3)	0.56966(3)	9.01(6)	1
I(6)	2i	0.21285(3)	0.93040(3)	0.35455(3)	8.94(6)	1
Cs	1a	0	0	0	22.9(1)	1
C	2i	0.5258(5)	0.4923(5)	0.4241(5)	8.0(8)	1

^{a} $U_{eq} = (8\pi^2/3) \sum_i \sum_j U_{ij} a_i^* a_j^* \bar{a}_i \bar{a}_j$

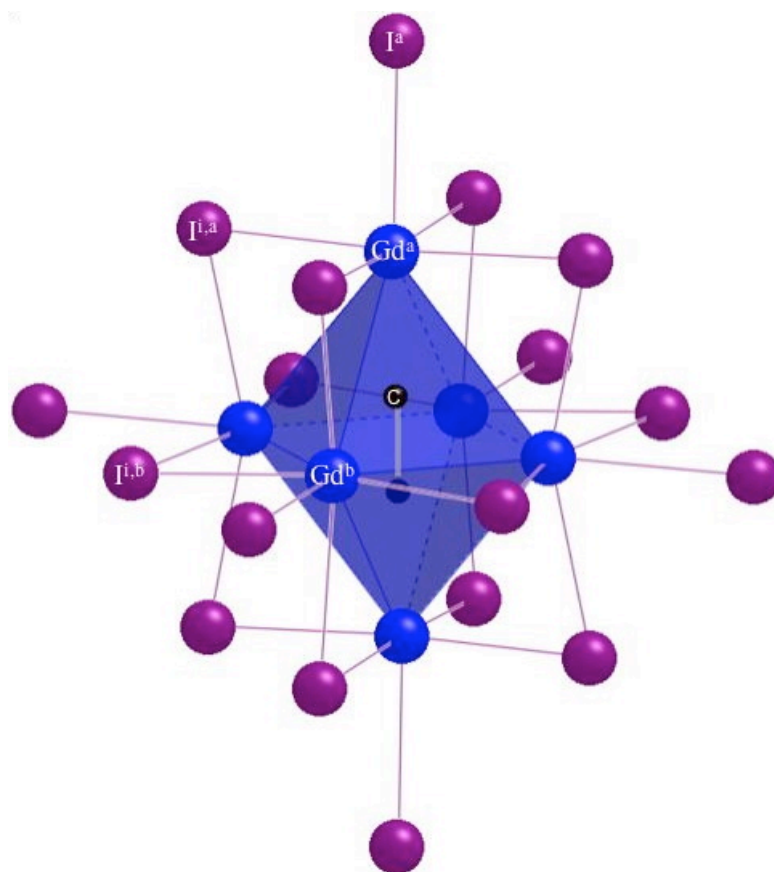**Figure 5.1**. Labels used in the interatomic distances Table (5.3). Gd^a atoms are on the elongated axis where as the Gd^b atoms are in the basal plane of the cluster. An I^{i,a} atom is edge bridging (inner) iodine atom that bridges Gd^b –Gd^a bonds. An I^{i,b} is a edge bridging iodine atom that bridges a Gd^b–Gd^b bond. An I^a atom is axial to the cluster and not bridging.

Table 5.3. The ranges of selected interatomic distance and angles for $Gd_6C_2I_{11}$, $Gd(Gd_6C_2I_{12})$, $CsGd(Gd_6C_2I_{12})_2$ and $Cs(Gd_6C_2I_{12})$[*]

Distances (Å)	$Gd_6C_2I_{11}$	$Gd(Gd_6C_2I_{12})$	$CsGd(Gd_6C_2I_{12})_2$	$Cs(Gd_6C_2I_{12})$
Gd^b-C	2.535-2.590	2.512-2.578	2.492-2.603	2.534-2.569
Gd^a-C	2.224-2.236	2.224(2)	2.172-2.172	2.230
Gd^b-Gd^b	3.455-3.495	3.453-3.471	3.428-3.469	3.456-3.469
Gd^b-Gd^a	3.770-3.905	3.808-3.817	3.746-3.820	3.782-3.887
Gd^b-$I^{i,b}$	2.987-3.016	3.122-3.123	3.075-3.157	3.005-3.018
Gd^b-$I^{i,a}$	3.046-3.087	3.122-3.123	3.075-3.157	3.087-3.090
Gd^b-I^{a-i}	3.336-3.397	3.508	3.510-3.516	3.332-3.381
Gd^b-$I^{i,b-a}$	3.043-3.091	3.107-3.127	3.106-3.131	3.075-3.093
Gd^b-$I^{i,a-a}$	3.087-3.167	3.107-3.127	3.106-3.131	3.151-3.188
Gd^b-$I^{i,a-i}$	3.254-3.273			
Gd^a-$I^{i,a}$	2.961-3.035	3.041-3.051	3.003-3.123	3.015-3.030
Gd^a-I^{a-i}	3.220-3.260	3.033	3.054-3.056	3.248
Gd^a-$I^{i,a-a}$	3.042-3.126	3.041-3.051	3.065-3.083	3.111-3.114
Gd^a-$I^{i,a-i}$	3.164-3.169			
C-C	1.469	1.40(3)	1.463	1.455
Gd^n-I		3.074-3.076	3.052	
Cs-I			4.195	4.005-4.275
Angles (Degrees)				
I^i-Gd^b-I^i	156.94-160.27	157.06-157.62	156.83-158.85	157.17-160.00
I^i-Gd^a-I^i	173.11-176.89	174.56-174.94	173.23-175.16	174.94-176.19

[*]For the iodine labels the first superscript term corresponds to the position as labeled in Figure 5.1. The superscript term after the dash corresponds to the position on the neighboring cluster. For example Gd^b-$I^{i,b-a}$ corresponds to an interatomic distance between a basal Gd atom and an I atom that is bridging two basal Gd atoms and axial on the neighboring cluster.

Computational Studies. The electronic structures of bulk $Cs(Gd_6C_2I_{12})$ and a discrete molecular model $Gd_6C_2I_{12}(IH)_6^-$ cluster, intended to represent a single cluster of $Cs(Gd_6C_2I_{12})$, were investigated using density functional theory (DFT). Within the Cerius 2 program suite,[86] DMol^3 was used to perform the calculations.[87-89] The Becke

exchange functional,[90] the Lee-Yang-Parr correlation functional[91] (BLYP),[92] and relativistic effective core potentials (ECP)[93] with the double numerical basis including d-polarization functions (DND) were used in the calculations – all as implemented in DMol^3. The convergence criterion for the energy was set to 10^{-6} a.u. The atomic coordinates from the crystal structure of $CsGd_6C_2I_{12}$ were used. A grid of 36 k-points where used to calculate the DOS. Averaged interatomic distances from the crystal structure of $Cs(Gd_6C_2I_{12})$ were used to construct the $Gd_6C_2I_{12}(IH)_6{}^-$ model so that it had D_{4h} symmetry.

The YAEMOP program[94] was used to perform the extended Hückel calculations. The extended Hückel exponents, valence shell ionization potentials and coefficients for Gd atoms are shown in Table 5.4. 6s and 5d electrons are assigned two different H_{ss} and H_{dd} energies, depending on whether their spins are parallel (Gd^+) or antiparallel (Gd^-) to the 4f electrons' spins on the atom on which they reside. The parameters were obtained from previous calibration calculations performed on similar compounds.[95]

Table 5.4. Extended Hückel exponents (ζ), valence shell ionization potential (H_{ii} in eV) and coefficients[95]

Atom	Orbital	H_{ii} (eV)	ζ_1	ζ_2	c_1	c_2
"Gd+"	5s	-7.12	1.74			
	5p	-4.40	1.70			
	4d	-7.03884	1.40	3.60	0.8316	0.3041
"Gd–"	5s	-6.91	1.74			
	5p	-4.40	1.70			
	4d	-6.56116	1.40	3.60	0.8316	0.3041
Y	5s	-7.02	1.74			
	5p	-4.40	1.70			
	4d	-6.80	1.40	3.60	0.8316	0.3041
I	5s	-18.00	2.679			
	5p	-12.70	2.322			
C	2s	-21.40	1.625			
	2p	-11.40	1.625			
O	2s	-32.30	2.275			
	2p	-14.80	2.257			
P	3s	-18.60	1.75			
	3p	-14.00	1.30			
H	1s	-13.60	1.30			

Gd^+ and Gd^- correspond to the parameters used to model the spin-dependent energies of valence s and d electrons for Gd atoms with spins aligned parallel and antiparallel respectively with the local spin direction of the 4f electrons.

For the molecular models an idealized D_{4h} $Gd_6C_2I_{12}$ cage was constructed using averaged interatomic distances from the crystal structure of $CsGd_6C_2I_{12}$. As we have done in previous calculations, phosphine oxide (OPH$_3$) ligands were also used to "cap-off" clusters to mimic the coordination environment supplied by iodine atoms in the solid state.[26,44,95] The interatomic distances for the OPH$_3$ ligand were obtained from the previous calculations just mentioned[26,44,95] and the Gd-O distance chosen based on rare earth phosphine oxide distances found in "Comprehensive Coordination Chemistry II Volume 3."[96] The bent OPH$_3$ ligands were arranged to yield a cluster of C_{2h} symmetry.

Results and Discussion

  Synthesis. The compounds reported in this paper illustrate the delicate balance that determines relative phase stability in these dicarbide-containing Gd-rich iodides. A dramatic illustration of this delicacy is found in the three reactions wherein $Gd(Gd_6C_2I_{12})$, $Gd_6C_2I_{11}$ and $CsGd_{10}(C_2)_2I_{18}$ were found under nearly identical conditions. Three reaction tubes were loaded with the same reactants in the same ratios, i.e., all loaded at the "$CsGd(Gd_6C_2I_{12})_2$" composition, heated in the same furnace wherein they were subjected to the same temperature gradient for the same length of time. The results of several reactions targeted to form the ternaries $Gd(Gd_6C_2I_{12})$ and $Gd_6C_2I_{11}$ often yielded mixtures of these compounds. To date, the best yield obtained for $Gd(Gd_6C_2I_{12})$ was obtained from a reaction tube that was loaded with a stoichiometric ratio of Gd, GdI_3 and C (3:4:2 molar ratio) and heated to 900ºC for 500 hrs followed by slow cooling to room temperature. For $Gd_6C_2I_{11}$, the best yield to date was observed in a reaction loaded stoichiometrically (7:11:6 $Gd:GdI_3:C$), heated to 900ºC for 400 hrs. In these two instances, $Gd(Gd_6C_2I_{12})$ did not appear in the powder pattern of the product loaded for $Gd_6C_2I_{11}$, and vice versa. Caution should be exercised in interpreting these results – more often we obtain mixtures of these two phases, perhaps because the minor but persistent formation of GdOI obviously shifts the phase composition towards the Gd-poorer phase, $Gd_6C_2I_{11}$.

  Despite several attempts to improve the yield of $CsGd(Gd_6C_2I_{12})_2$ by varying the reaction conditions, $CsGd(Gd_6C_2I_{12})_2$ is at best synthesized in disappointing yield. The largest quantity and best quality crystals came from reactions conducted with Cs-rich and C-poor compositions (Gd, GdI_3, CsI and C in ratios to target "$CsGd_6C_1I_{12}$") in a temperature gradient of 850-830ºC over 7 cm. In reactions run with the

"CsGd($Gd_6C_2I_{12}$)$_2$" composition, Cs($Gd_6C_2I_{12}$), Cs($Gd_{10}C_4I_{18}$)[97] and Gd($Gd_6C_2I_{12}$) were the more prevalent products.

Structure. The most important factor that distinguishes cluster compounds discussed in this paper from most of the uncondensed cluster compounds of electron-poor metals in literature is the presence of the C_2 unit, which forces the octahedral Gd_6 cage to distort. In compounds that adopt structure types wherein the clusters of the parent compound lie on sites of threefold symmetry, the incorporation of a dicarbide unit as an interstitial results either in disorder or in a lowering of symmetry. When disorder is complete, the averaged structure maintains the symmetry of the parent structure type.

Gd($Gd_6C_2I_{12}$) adopts the ubiquitous '7-12' structure type that has been observed over the entire range of rare-earth metals with a variety of interstitial atoms.[31,38,43,44,46,81] Typically, in structures of this type, the RE_6 cage exhibits modest departures from an ideal octahedral geometry when centered by a single transition metal or main group atom. When centered by a dicarbide unit, the cluster is lengthened along one local 4-fold axis to accommodate the C_2 'dumbbell', as seen in compounds such as $Cs_4Pr_6C_2I_{13}$,[54] $Cs_2(Pr_6C_2I_{12})$,[52] Rb($Pr_6C_2I_{12}$),[48] $Sc_6C_2I_{11}$,[36] and $R_6C_2I_{10}$ (R=La, Ce).[34] Of course, the same is seen in numerous condensed cluster compounds as well.[34,50,98-104] Since in the parent 7-12 structure type has $R\bar{3}$ (No.148) space group symmetry and the clusters are centered on $\bar{3}$ positions, the C_2 'dumbbell' is impossible to accommodate without symmetry breaking, unless it is disordered. In our refined model of the structure, just such disorder is present – it is an averaged structure in which symmetry dictates equal populations of clusters distorted along each of the local 4-fold axes (left side of Figure 5.2). This averaged structure consists of an inner octahedron of gadolinium atoms with Gd-Gd distances of 3.453-3.470 Å and outer octahedron of gadolinium with Gd-Gd distances of 4.122-4.144 Å. The center of the averaged

structure contains six carbon atom sites (related by a 3-fold rotation). The outer Gd
atom sites are about 0.5 Å from the inner Gd atom sites.

Based on the distances and displacement parameters (the U_{eq}s were large for the
Gd and C atoms) a disorder model was used to refine the site occupancy factors of the
Gd and C sites. There were no q peaks near the iodine atoms that would allow for the
refinement of split position iodine sites. The constraints used to model the disorder
were:

$$SOF_{Gd\ inner} + SOF_{Gd\ outer} = 1$$

$$SOF_{Gd\ outer} = SOF_C$$

where $SOF_{Gd\ inner}$ is the site occupancy factor for the inner Gd site, $SOF_{Gd\ outer}$ is the site
occupancy factor for the outer Gd site and SOF_C is the site occupancy factor for the
carbon site. This model was chosen because simultaneous occupancy of adjacent inner
and outer Gd sites is physically precluded. In any individual cluster, one expects
occupancy of two outer sites (collinear with the C_2 axis) and four inner sites (in the
stretched octahedral basal plane). The refined inner to outer occupancy ratio (SOF_{Gd}
$_{inner}$:$SOF_{Gd\ outer}$ = 69:31) was in good correspondence with this expectation. Since the
refined occupancy factors are close to those expected for a cluster distorted along one
axis, we assume the structure consists of disordered, distorted octahedra. The
interpretation of the disorder is pictorially represented in Figure 5.2 and the interatomic
distances of $Gd(Gd_6C_2I_{112})$ are labeled in Figure 5.3.
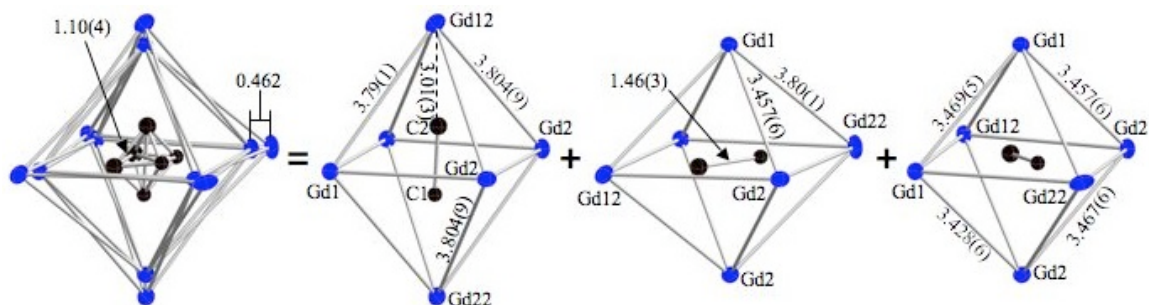
Figure 5.2. The averaged cluster of $CsGd(Gd_6C_2I_{12})_2$ is shown on the left. The structure was modeled as being the average of the three distorted clusters shown on the left. The ratio of $Gd_{inner}:Gd_{outer}$ occupation was refined to 64:36. Gd1 and Gd2 are Gd_{inner} sites while Gd12 and Gd22 are Gd_{outer} sites. Thermal ellipsoids are plotted at 50%. The same refinement model was used for $Gd(Gd_6C_2I_{12})$.
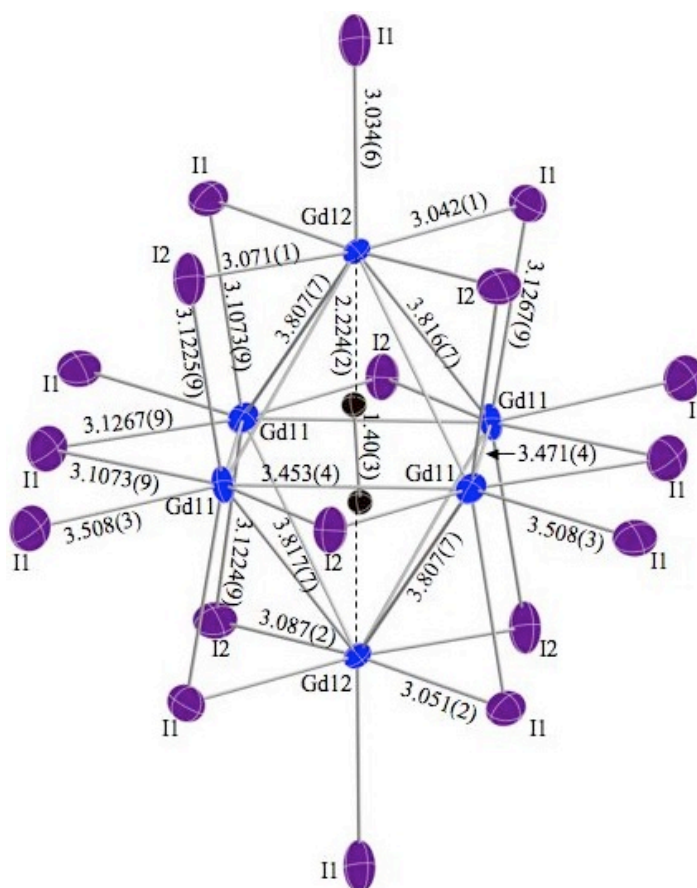
Figure 5.3. Interatomic distances for a cluster of $Gd(Gd_6C_2I_{12})$. Thermal ellipsoids plotted at 95% probability.

The structure of $CsGd(Gd_6C_2I_{12})_2$ is a distorted variant of the $CsEr(Er_6CoI_{12})_2$ type.[44] Initially this structure was solved with one carbon in the center of the cluster, which is located 2.357-2.544 Å from the surrounding Gd atoms. There were 689 reflections that violated the systematic absences for $Pa\bar{3}$ and $|E^2-1|$ was large (1.26). Other space group suggestions from Xprep were tried to no avail. The initial solution was then entered into Platon to check for twinning. The TwinRotMat function of Platon suggested the twin law shown in Figure 5.4. This twin operation applies a two fold operation that sends h to k and l to $–l$ (or any of the equivalent 6 permutations consistent with a cubic space group). The reflection conditions for $Pa\bar{3}$ are $hk0$: $h=2n$, $0kl$: $k=2n$, $h0l$: $l= 2n$ and $h00$: $h=2n$. If we look at the reflections in the $hk0$ plane of twin component 1 there should only be reflections that have even h indices. The presence of twin component 2, which has h and k axes flipped from twin component 1, will give the appearance of odd h indices in the $hk0$ plane and make the even h indices more intense. When the twin operation is applied to the structure some of the iodine sites are sent to the center of the clusters. The distribution of twin components was refined to be 59:41 and the R_1 value was reduced to 0.0659 from 0.2490. After the twin law was applied the peaks for the C_2 interstitial were identifiable but there was still a residual peak of 15.22 $e^-/Å^3$ in the center of the clusters due to imperfect refinement of the twin ratios. A residual peak (12.5 $e^-/Å^3$) 3.0 Å from the Cs atom was also present in the final refinement that was not enhanced or reduced by the application of the twin operation.
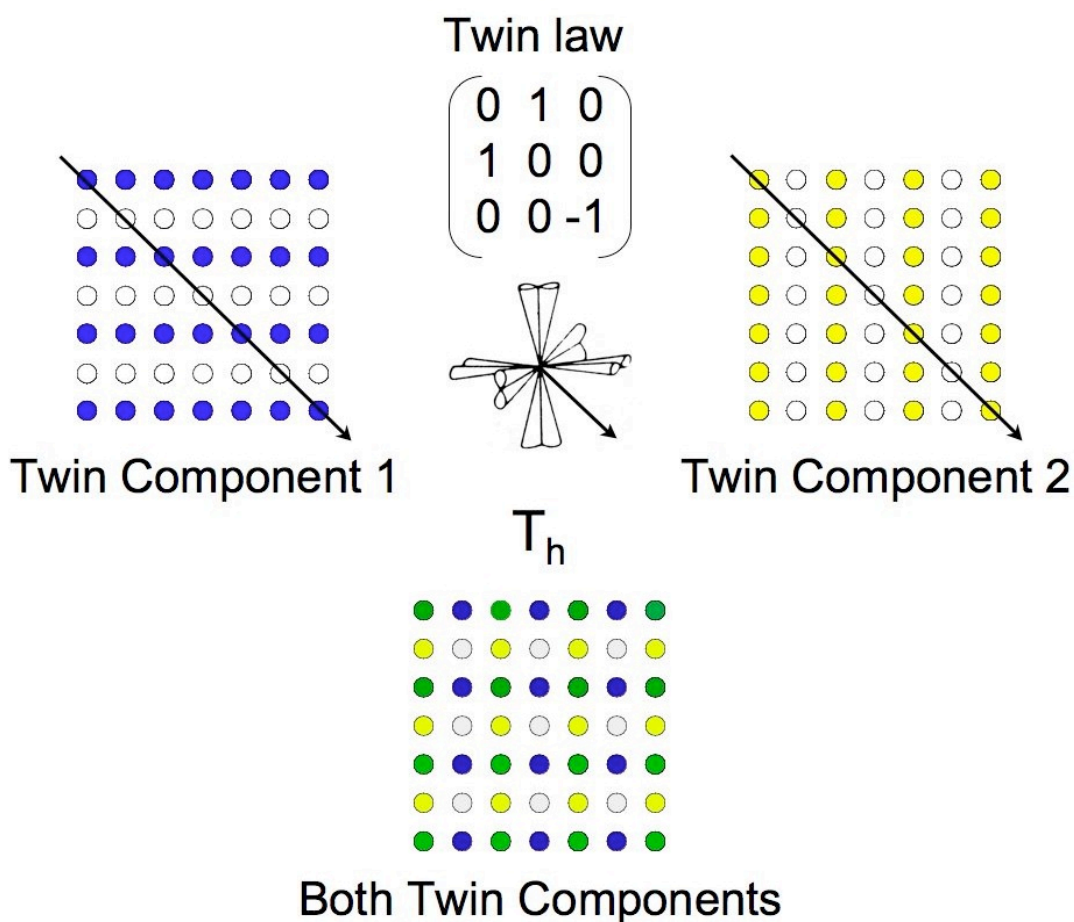
Figure 5.4. Relationship between twin components in the crystal structure of $CsGd(Gd_6C_2I_{12})_2$. The blue and yellow dots represent reflections in the hk0 pane for twin component 1 and 2. The green dots represent overlapping reflections of the two twin components. The arrows represent two fold rotation axes. The reflections conditions for Pa$\bar{3}$ are *hk*0*:* $h=2n$, 0*kl:* $k=2n$, *h*0*l:* $l=2n$ and *h*00*:* $h=2n$.

Also observed were residual electron density peaks located 0.5 Å from each cluster gadolinium. This symptom was identified as being caused by the disorder of distorted octahedra containing C_2 units as described for $Gd(Gd_6C_2I_{12})$. The same SOF constraints that were applied to the refinement of $Gd(Gd_6C_2I_{12})$, were applied to

CsGd(Gd$_6$C$_2$I$_{12}$)$_2$. The SOF$_{Gd\ inner}$:SOF$_{Gd\ outer}$:SOF$_C$ ratio refined to 64:36:36. The interatomic distances of the Gd$_6$C$_2$ cluster of CsGd(Gd$_6$C$_2$I$_{12}$)$_2$ are shown in Figure 5.2.

CsGd$_6$C$_2$I$_{12}$ adopts the CsEr$_6$CI$_{12}$[49,50] structure type. The distortion of the Gd$_6$ cage, as a result of incorporating a dicarbide interstitial, lowers the space group from the parent structure (R$\overline{3}$) to P$\overline{1}$ (Unit cell shown in Figure 5.5). The first several crystals that single crystal x-ray diffraction data was collected on indexed with unit cell parameters similar to the ones obtained on the structure reported here. However, the data indexed poorly (many peaks that could not be indexed within a reasonable degree of tolerance) and in the cases where full data sets were collected, structure solutions exhibited symptoms similar to CsGd(Gd$_6$C$_2$I$_{12}$)$_2$ (twinning and/or disorder). Distortions caused by incorporating a C$_2$ group as an interstitial of an octahedron in a structure type where the parent space group contains a threefold, tend to result in disorder in most of the crystals for which data was collected. In some cases single crystal data could be indexed to a rhombohedral unit cell with the dimensions a,b = 11.2(1) Å and c = 20.8(2) Å. These parameters are similar to the ones obtained for Cs(Er$_6$CI$_{12}$).[49,50] The last crystal x-ray diffraction data was collected on was void of these problems and the solution was routine.
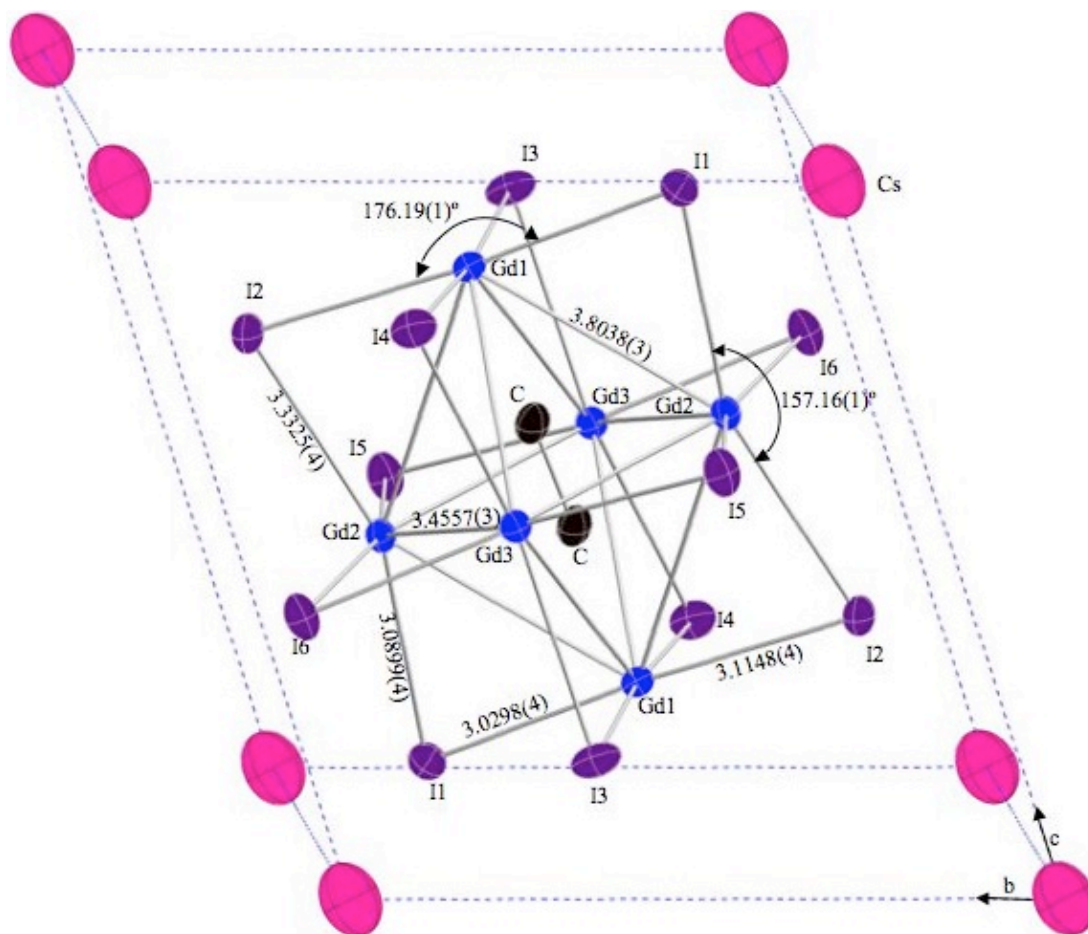
Figure 5.5. Unit cell of $Cs(Gd_6C_2I_{12})$ (Thermal ellipsoids plotted at 95%). An inversion center resides in the center of the cluster.

$Gd_6C_2I_{11}$ adopts the $Sc_6C_2I_{11}$ structure type.[36] The Schäfer and Schnering notation[28] for this structure is $(Gd_6C_2)I^i_4I^{i\text{-}i}_{2/2}I^{i\text{-}a}_{6/2}I^{a\text{-}i}_{6/2}$. Of the structures reported here $Gd_6C_2I_{11}$ is the most crosslinked. This is also the only structure reported here that does not have a non cluster cation. The $I^{i\text{-}i}$ type cross linking (shown in Figure 5.6) brings the clusters closer together (center of Gd_6 cage to center of neighboring Gd_6 cage for $Gd_6C_2I_{11}$ 7.729 Å, $CsGd_6C_2I_{12}$ 9.334 Å, $CsGd(Gd_6C_2I_{12})_2$ 9.496 Å, $Gd(Gd_6C_2I_{12})$ 9.518

Å) than the others reported here. This compound also has a longer C-C distance (1.46(1)

Å) than the other compounds reported here (see Table 5.3).
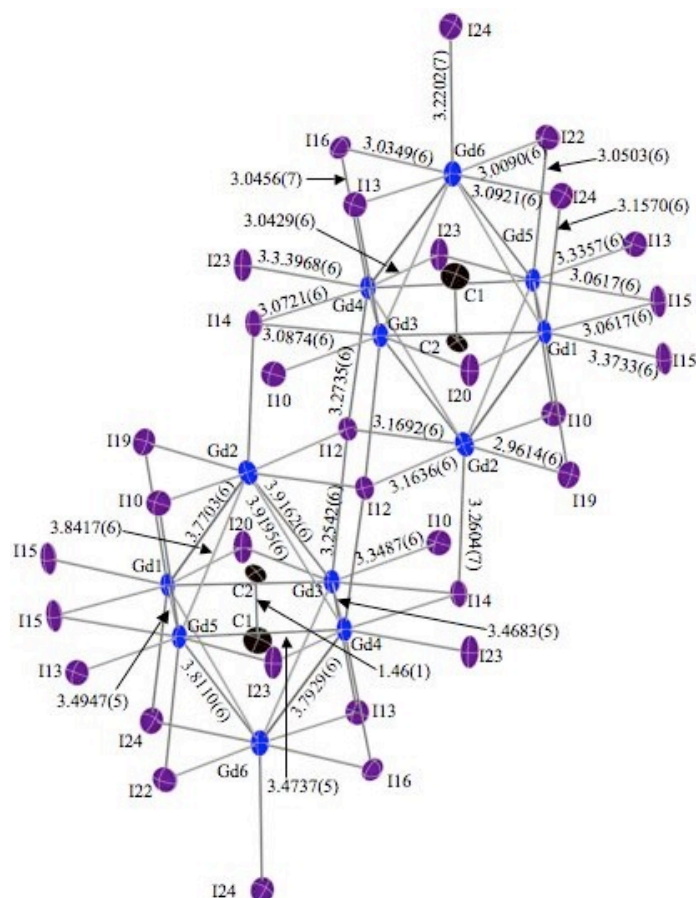
Figure 5.6. Two clusters of $Gd_6C_2I_{11}$ cross linked via $I(12)^{i-i}$ and $I(14)^{i-a}$. Gd-I and Gd-Gd distances labeled on the upper and lower clusters respectively. The two clusters are related by an inversion center. Thermal ellipsoids plotted at 95%.

Electronic Structure. The electronic band structure of $CsGd_6C_2I_{12}$ calculated by

DFT was used as a benchmark to evaluate the results of molecular model calculations.

The band structure calculation yielded results that are basically in accord with various

other computational treatments of dicarbide-containing cluster compounds.[36] The DFT density of states for $CsGd_6C_2I_{12}$ (Figure 5.7) was calculated assuming a ferromagnetic Gd spin alignment. For the moment, we'll confine our comments to the general features of the calculation, some details being more readily understood by reference to calculations on molecular model systems discussed below. The very sharp and large peaks at about -7 eV for the α spin and about -1.5 for the β spin correspond to localized Gd 4f orbitals. The remaining bands ranging between -5.7 eV and -9 eV have mostly iodine or C-C bonding character and are therefore little affected by the Gd 4f spins. For this reason, the occupied up- and down-spin DOS curves closely mirror each other in this energy range (disregarding the 4f bands themselves). The up spin (α) band at -3.59 eV and the down spin (β) band at -2.61 eV correspond to the half-occupied b_{1g} basal plane bonding orbital shown on page 93– also discussed below. The up- and down-spin bands centered near -4.6 eV correspond to the e_g cluster-based orbitals that are well described as filled $C_2\ \pi^*$ orbitals that have been stabilized by interaction with Gd-based 5d-orbital acceptors. The up-spin band at -2.48 eV and the down spin band at -2.12 eV corresponds to the orbital of b_{1u} symmetry shown on page 93. The remaining unoccupied bands between -2 eV and 0 eV have predominantly Gd 5d character.
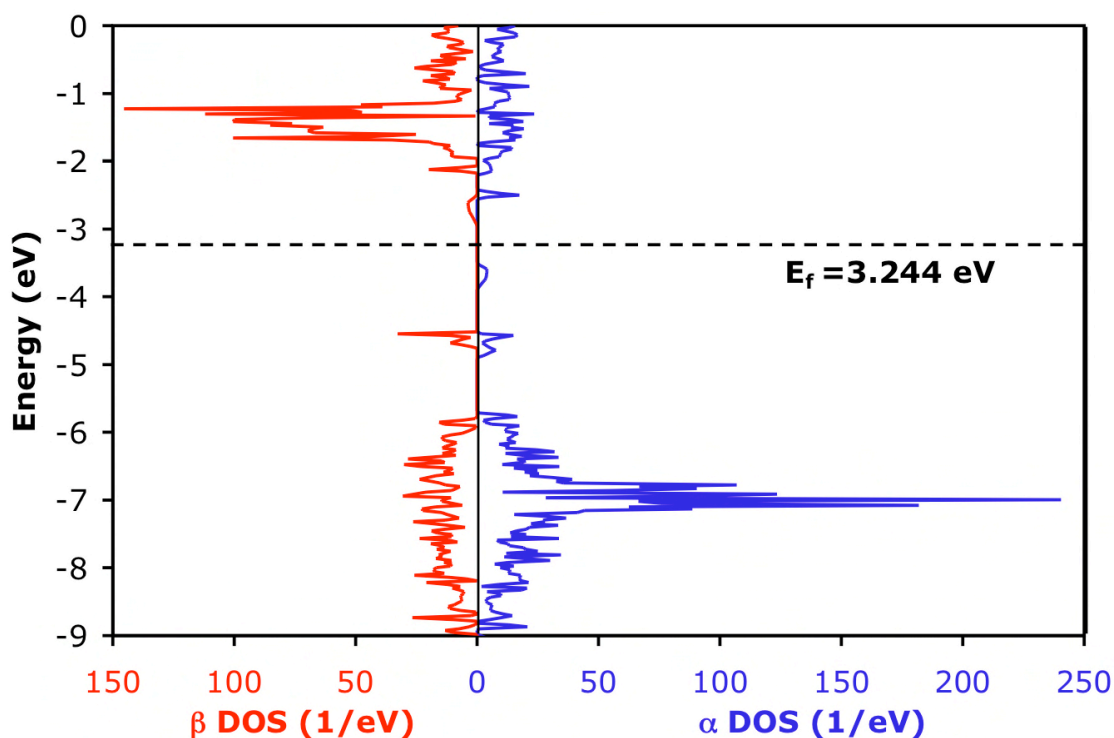
Figure 5.7. DOS plot for the α and β spin electrons of the ferromagnetic spin pattern for CsGd$_6$C$_2$I$_{12}$ calculated by DFT using 36 k-points.

In order to understand the magnetic behavior expected of the dicarbide-centered cluster compounds reported in this chapter, two model systems were studied. The first was Gd$_6$C$_2$I$_{12}$(IH)$_6$$^{n-}$ ($n = 0, 1, 2, 3$) where HI was used to complete the coordination sphere of the Gd$_6$C$_2$I$_{12}$ cluster, i.e., the HI serves in place of iodine atoms from adjacent clusters that are present in the solid state. In the same spirit, we also performed calculations in which phosphine oxide ligands served to cap-off the terminal ligand sites, Gd$_6$C$_2$I$_{12}$(OPH$_3$)$_6$$^{n-}$ ($n = 0, 1, 2, 3$) (shown in Figure 5.8). OPH$_3$ ligands have been used for similar molecular models in the past.[26,44,95] Geometrical details and assumptions are presented in a preceding section. Calculations on these molecular model systems were

performed with the use of both DFT and the spin-polarized extended Hückel method we have previously described.[26,44,95]

Unfortunately, in all the molecular model system DFT calculations, several 'artifact' Kohn-Sham orbitals are encountered at energies near to that of the b_{1g} basal-plane orbital (the SOMO for $Gd_6C_2I_{12}(IH)_6{}^{1-}$). These are predominantly antibonding orbitals localized on the terminal ligands (-IH or -OPH$_3$). Of course, these orbitals have no counterparts in the bulk electronic band structure of $CsGd_6C_2I_{12}$ – hence our labeling of them as 'artifacts'. They pose the most serious complications in the calculations of mono- and polyanionic systems; indeed with negative charges exceeding −1, their presence seems to preclude convergence to any physically satisfactory description of the electronic structure. We obtained convergence for $Gd_6C_2I_{12}(IH)_6{}^{1-}$ and the occupied orbitals are sensible (very analogous to those found in solid-state band structure of $CsGd_6C_2I_{12}$). Nevertheless, some artifact orbitals are still found interleaving the low-lying unoccupied cluster orbitals within 0.4 eV of the b_{1g} SOMO. As we shall see, the presence of such orbitals still injects some ambiguity into prediction or rationalization of magnetic properties. These artifacts are even worse for $Gd_6C_2I_{12}(OPH_3)_6{}^{n-}$ systems, where orbitals of OPH$_3$ character fall between the b$_{1g}$ and b$_{1u}$ cluster bonding orbitals. We therefore abandoned this model for use with DFT calculations.
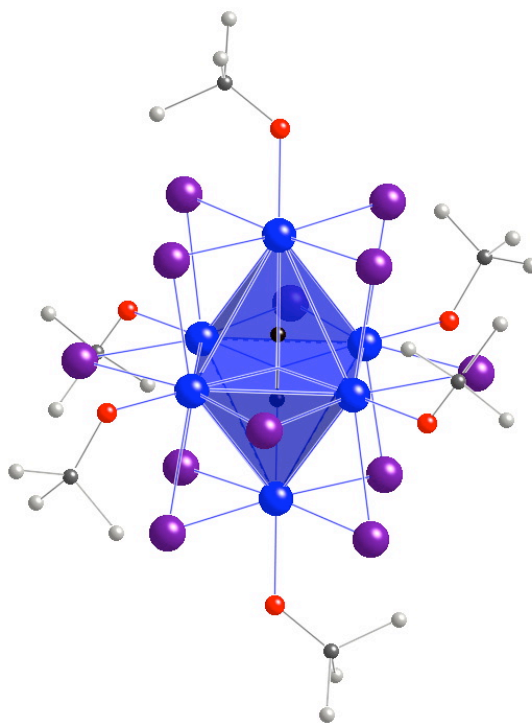
Figure 5.8. The molecular model, $Gd_6C_2I_{12}(OPH_3)_6$, used in the extended Hückel calculations. The OPH_3 ligands were arranged so that the model would have C_{2h} symmetry. The Gd atoms are blue, the Iodine atoms are purple, the carbon atoms are black, the oxygen atoms are red, the phosphorus atoms are dark gray and the hydrogen atoms are light gray.

Among the compounds reported and structurally characterized in this paper, three different cluster-bonding electron counts (CBEs) are represented. Formal electron counting makes this clear: $Cs(Gd_6C_2I_{12})$ and $Gd_6C_2I_{11}$ are respectively accounted for as $Cs^+Gd_6^{18+}C_2^{6-}I_{12}^{12-}\cdot1e^-$ and $(Gd_6^{18+}C_2^{6-}I_{11}^{11-})\cdot1e^-$; $CsGd(Gd_6C_2I_{12})_2$ is represented as $Cs^+Gd^{3+}[(Gd_6^{18+}C_2^{6-}I_{12}^{12-})\cdot2e^-]_2$; $Gd(Gd_6C_2I_{12})$ is represented as $Gd^{3+}(Gd_6^{18+}C_2^{6-}I_{12}^{12-})\cdot3e^-$. In every case, the dicarbide assignment, C_2^{6-}, is consistent with filling the π^* orbitals (as already indicated for the bulk solids' band structure) and a C-C distance of $\sim$ 1.46 Å. Unfortunately, synthetic obstacles already described have so far prevented us from obtaining sufficiently pure samples to perform magnetic measurements on any of

these compounds except $Cs(Gd_6C_2I_{12})$. Nevertheless, we present a unified discussion of the expected effects of that variations in the CBE counts are expected to exert on coupling between the d $4f$ magnetic moments. This treatment, with some adaptation, will be of relevance to measurements (not yet performed) on cerium and praseodymium compounds mentioned in our introductory section and more materials not yet synthesized.

To compare the relative energies of various spin patterns for the -1, -2, and -3 clusters, extended Hückel (EH) calculations on the $Gd_6C_2I_{12}(OPH_3)_6$ model was used. Figure 5.10 exhibits the ordering, relative energies, and character of the EH MOs and a comparison with their solid state counterparts calculated for $CsGd_6C_2I_{12}$ at $k = 0$ using DFT. Since the ordering and orbital character of the frontier orbitals calculated using EH match those calculated using DFT on the solid, even if the quantitative energy gap comparison is only fair. (We shall argue that the $E(b_{1g}) - E(b_{1u})$ gap is the most important. The reader should bear the differences in these treatments in mind however, since the differences in orbital energy differences will affect the quantitative aspects of what follows.

Figure 5.9 shows how the Gd_6 cage orbitals interact with the C_2 interstitial orbitals to give the molecule based obitals. Opposed to the nearly O_h symmetric transition metal centered clusters, these clusters are distorted to D_{4h} and the interstitial is a C_2 unit. The orbitals of the C_2 interstitial ($\sigma^*_{s/p}$ (a_{2u}), π (e_u), σ_p (a_{1g}), π^* (e_g)) can interact with the cage orbitals, which have a_{2u}, e_u, a_{1g} and e_g symmetry. This leaves the cage orbitals of b_{1g} and b_{1u} symmetry.

From the pictures of the MOs calculated from the $k=0$ DFT calculation of $CsGd_6C_2I_{12}$ we can get an idea of the nature of the orbitals. The b_{1g} SOMO could be described as bonding between the $5d_{xy}$ orbitals of the basal Gd atoms. The b_{1u} type

orbital consists of a bonding combination of d_{yz} orbitals on the Gd atoms. The wavefunction coefficients are smaller on the axial Gd atoms than those of the basal Gd atoms. The e_g orbitals below the b_{1g} orbital are a bonding combination of the π^* orbitals of the C_2 unit and the out of phase combination of trans basal Gd d_{xz} orbitals.

To fill in the electrons into the MO diagram we count electrons by considering each atom as an ion. For example, $CsGd_6C_2I_{12}$ would be counted as $Cs^+Gd_6^{18+}C_2^{6-}I_{12}^{12-} \bullet 1e^-$. The C_2 intersititial is counted as having a C-C single bond because of its bond distance (1.469Å) and the diatomic π^* orbitals being filled. Based on this counting scheme $Cs(Gd_6C_2I_{12})$ has one extra electron that goes into the next orbital above the e_g orbitals that contain C_2 π^* character. The electron count for $CsGd(Gd_6C_2I_{12})_2$ breaks down as $Cs^+Gd^{3+}(Gd_6^{18+}C_2^{6-}I_{12}^{12-})_2 \bullet 4e^-$. This leaves two extra electrons per cluster that go into orbitals above the orbitals with C_2 π^* character. $Gd(Gd_6C_2I_{12})$ would have three extra electrons that go into orbitals above the e_g set. $CsGd(Gd_6C_2I_{12})_2$ has a closed shell b_{1g} HOMO and $Gd(Gd_6C_2I_{12})$ has a b_{1u} SOMO.
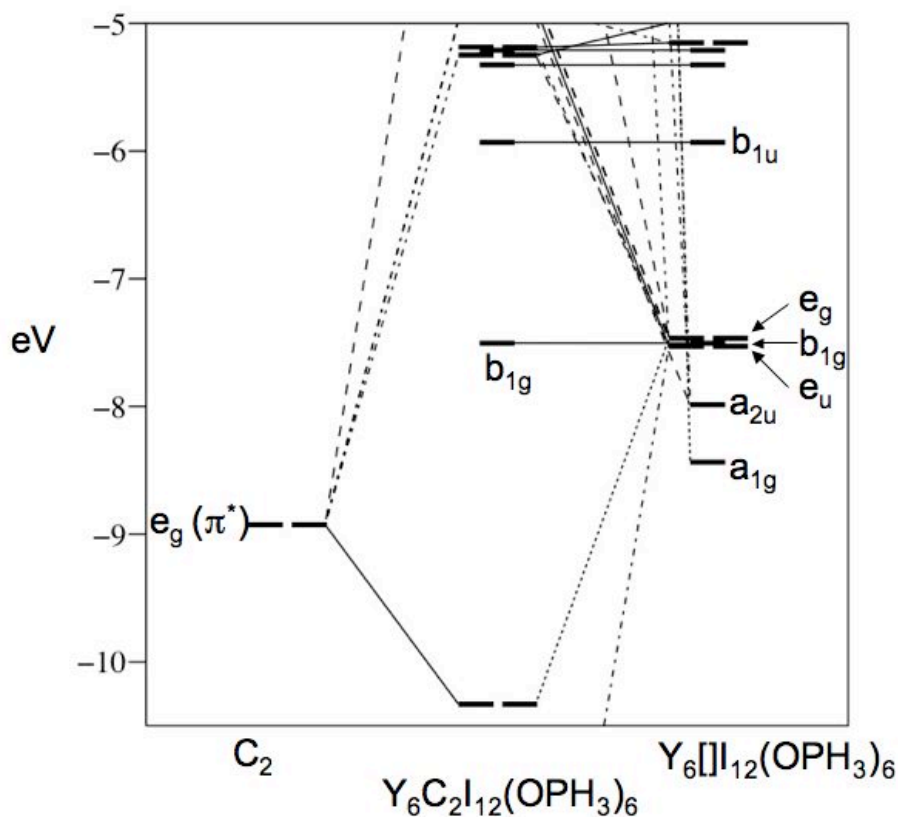
Figure 5.9. Fragment molecular orbital diagram for the C_2 interstitial interacting with the $Y_6[]I_{12}(OPH_3)_6$ empty cage. Y was used as a non $4f$ electron containing substitute for Gd.

By comparing orbital energies of "$Y_6C_2I_{12}(OPH_3)_6$" and "$Gd_6C_2I_{12}(OPH_3)_6$" using EH we can get an idea of the magnitude of stabilization caused by d-f exchange interactions. On the left hand side of Figure 5.10 the relative energies of "$Y_6C_2I_{12}(OPH_3)_6$" represents the cluster with no electrons in $4f$ orbitals. When the stabilization (destabilization) of the $5d$ and $6s$ orbitals due to the presence of parallel (antiparallel) spins of the $4f$ electrons is applied the α and β spins split in the manner shown on the right hand side of Figure 5.10. The stabilization of the α spins is greater for the ferromagnetic spin pattern (middle of Figure 5.10) than the spin pattern with the

electrons in the $4f$ orbitals of one of the basal Gd atoms apposing the rest (far right of Figure 5.10).

Several factors influence the splitting of the α and β spins. One factor is the amount of Gd $5d$ and $6s$ character the orbital, which contains the electron in question, has. For example in Figure 5.10 the α and β spins split more in the b_{1g} and b_{1u} than in the e_g orbitals because there is more Gd $5d$ character in the b_{1g} and b_{1u} orbitals. Another factor that influences the splitting of the α and β spins is the number of parallel $5f$ spins. If the spins of the electrons in the $4f$ orbitals of one of the basal Gd atoms are flipped to oppose the rest the splitting of the α and β spins is decreased as shown in Figure 5.10. As a result of flipping the spins of the $4f$ electrons on one of the basal atoms the e_g set from the D_{4h} spin pattern are no longer equivalent in the C_{2v} spin pattern, so they split into a_2 and b_1 orbitals. Mixing between orbitals of similar energy and the same symmetry also plays a role in the degree of splitting of the α and β spins. The degree of splitting of the α and β spins can be observed in the DOS plot of $Cs(Gd_6C_2I_{12})$ calculated using DFT and plotted in Figure 5.7.
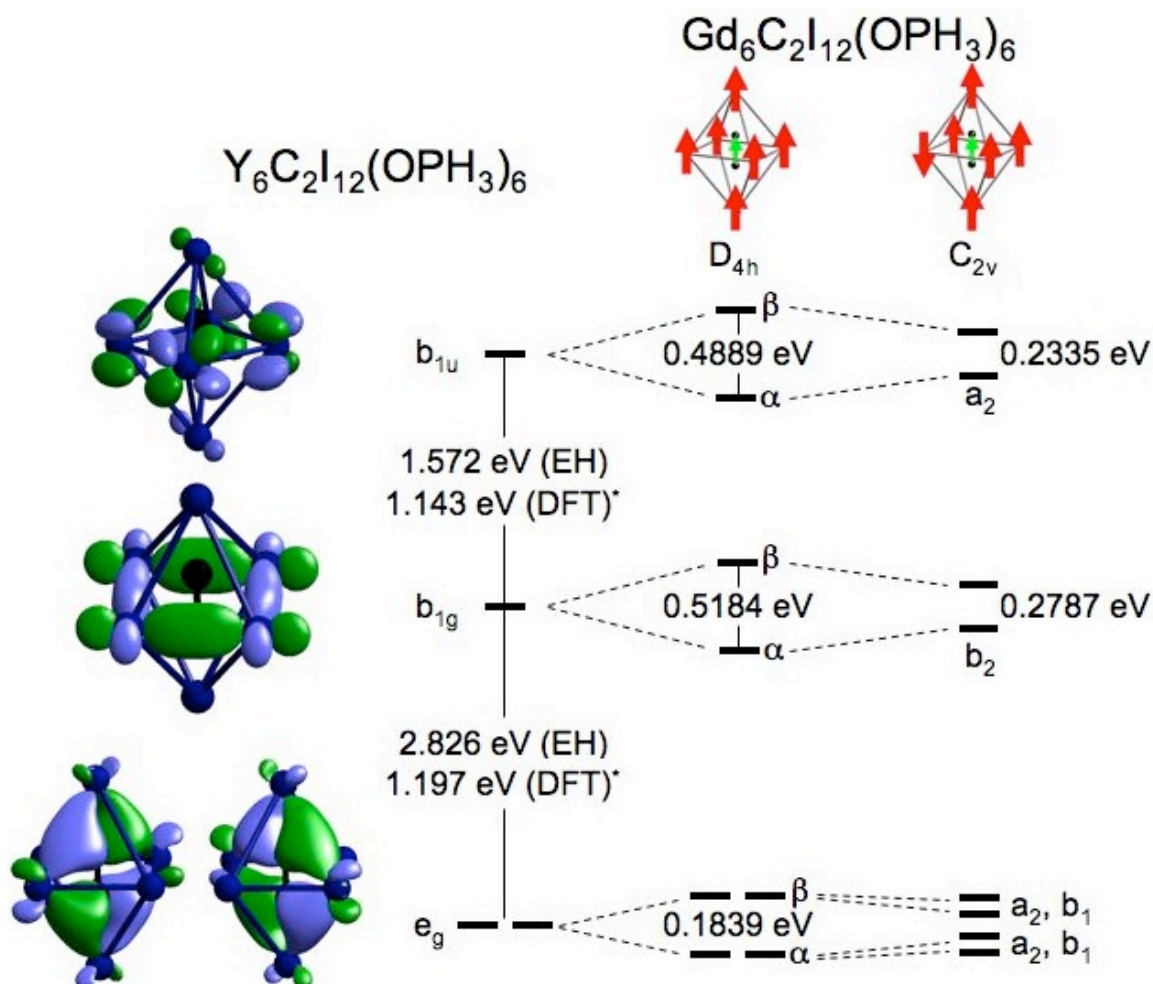
Figure 5.10. Orbital pictures for the frontier orbitals (rendered from the DFT calculations on "Cs($Y_6C_2I_{12}$)" using Cerius 2) along with the relative energies of the orbitals for $Y_6C_2I_{12}(OPH_3)_6$ calculated using EH and the bands of "Cs($Y_6C_2I_{12}$)" using DFT are shown on the left hand side. The splitting of the α and β spins calculated for two different spin patterns of $Gd_6C_2I_{12}(OPH_3)_6$ as calculated by EH is shown on the right. *The relative energies of the bands of "Cs($Y_6C_2I_{12}$)" were obtained from a 36 k-point, spin restricted, DFT calculation using the atomic coordinates Cs($Gd_6C_2I_{12}$) and comparing the energies at the center of the bands.

The density of states for $CsGd_6C_2I_{12}$ was calculated using DFT with results shown in Figure 5.10. The up spin (α) band at -3.59 eV and the down spin (β) band at -2.61 eV correspond to the b_{1g} basal plane bonding orbital shown in Figure 5.10. This band should be localized on the cluster and is half filled. The up spin band at -4.60 eV and the down spin band at -4.57 eV correspond to the e_g cluster based orbitals. The up spin band at -2.48 eV and the down spin band at -2.12 eV corresponds to the orbital of b_{1u} symmetry shown in Figure 5.10. The very sharp and large peaks at about -7 eV for the α spin and about -1.5 for the β spin corresponds to the electrons localized in the $4f$ orbitals of the Gd atoms. The bands lumped between about -5.7 eV and -9 eV have mostly iodine character and are not affected much by spins of the electrons in the 4f orbitals of the Gd atoms.

Magnetic Properties. The x-ray powder pattern of $Cs(Gd_6C_2I_{12})$ indicates a single phase product, nevertheless, susceptibility data inevitably exhibit contributions from magnetically ordered impurities in the samples that are apparently undetectable in the diffraction data. In order to saturate the contribution of the ferromagnetic impurities the magnetic susceptibility measurements were collected at a series of applied fields. As seen in Figure 5.11, an applied field of 2.0 Tesla or more is sufficient to effectively saturate the magnetically ordered impurities.
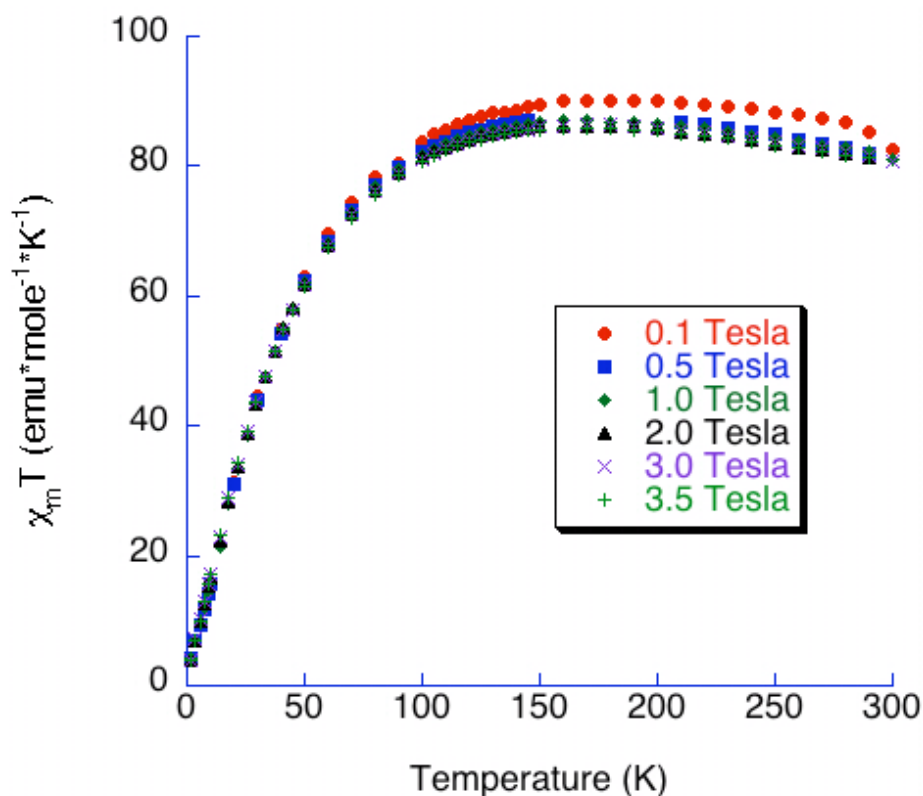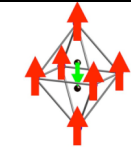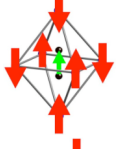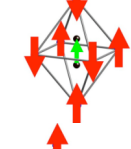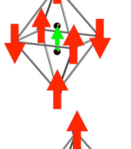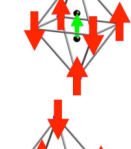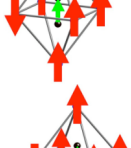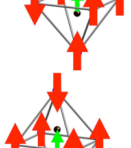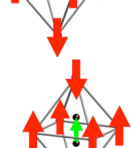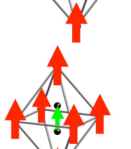
Figure 5.11. $\chi_m T$ vs. Temperature of $CsGd_6C_2I_{12}$ for applied fields of 0.1, 0.5, 1.0, 2.0, 3.0 and 3.5 Tesla applied fields.

In Figure 5.11, the susceptibility data are plotted as $\chi_m T$ vs. T. Ideal Curie behavior for this type of plot would result in a horizontal line that intercepts the $\chi_m T$ axis at a value that is equal to the Curie constant, $C_{molar} (= \chi_m T)$. The Curie constant is related to the effective magnetic moment per cluster (μ_{eff}) via the relationship $C_m = (N_a\mu_B^2/3k_B)\mu_{eff}^2$. The Curie constant expected for a collection of independent Gd spins (J=S=7/2; and taking $g_J = 2$) is $C_{Curie} = 47.25$ emu×K×mole^{-1}. Deviations in $\chi_m T$ from the Curie constant for 6 independent Gd spins are an indication of the net effect of magnetic coupling as a function of temperature. Values greater(less) than 47.25 emu×K×mole^{-1} indicate that the net alignment of moments with the external field is more(less) than expected for a collection of independent moments.

At temperatures above 130 K, $\chi_m T$ is roughly 85 emu×K/mole. Below 130 K antiferromagnetic coupling begins to dominate. If we calculate the expected C_m for the basal plane Gd moments to be ferromagnetically coupled and the axial Gd spins to be independent we get (C_m for 4 Gd ferromagnetically coupled = 105 emu×K/mole, C_m for two independent Gd atoms = 2×7.875, the total for 4 ferro Gds + 2 independent =) 120.75 emu×K/mole. While the observed C_m (85 emu×K/mole) at higher temperatures is lower than expected for all (243 emu×K/mole) or even just the basal (120 emu×K/mole) Gd spins to be ferromagnetically coupled, it is higher than six independent Gd spins (47.25 emu×K/mole).

Interpretation of Magnetic Results Using Calculations. The energies of selected spin patterns of $Gd_6C_2I_{12}(OPH_3)_6^{n-}$ were calculated using EH as implemented in YAEMOP. The "Gd^+" and "Gd^-" parameters in Table 5.4 were used to represent Gd with the spins of the electrons in the $4f$ orbitals relative to the spin up electron in the d orbitals of the Gd atoms. The results of these calculations are shown in Table 5.5. The models $Gd_6C_2I_{12}(OPH_3)_6^{n-}$ and $Gd_6C_2I_{12}(IH)_6^{n-}$ were used to represent $Cs(Gd_6C_2I_{12})$ when n=1. The models with n=2 and 3 represent the clusters of $CsGd(Gd_6C_2I_{12})_2$ and $Gd(Gd_6C_2I_{12})$ respectively.

Table 5.5. Relative energies (cm^{-1}) of spin patterns for [Gd$_6$C$_2$I$_{12}$(OPH$_3$)$_6$]^n calculated using EH and Gd$_6$C$_2$I$_{12}$(IH)$_6^n$ using DFT

n = -1 (EH)	n = -3 (EH)	n = -1 (DFT)	n = -2 (EH)
D$_{4h}$ 4181.176	D$_{4h}$ 3963.449	D$_{4h}$ 5318.507	
C$_{2v}$ 1925.890	C$_{2v}$ 1343.638	C$_{2h}$ 2481.907	D$_{4h}$ 415.375
C$_s$ 1845.234	C$_{2h}$ 1239.16	C$_{2v}$ 2457.150	C$_{4v}$ 320.686
C$_{2h}$ 1821.038	C$_s$ 1019.565	C$_{2v}$ 2169.638	D$_{4h}$ 257.613
C$_{2v}$ 1736.430	C$_{2v}$ 921.811	C$_s$ 2146.789	C$_{2h}$ 181.313
C$_{2v}$ 934.312	C$_{2v}$ 446.670	C$_{2v}$ 1090.548	C$_{2v}$ 169.699
C$_{2v}$ 846.075	C$_{2v}$ 405.777	C$_{2v}$ 1059.975	C$_{2v}$ 159.698
D$_{4h}$ 148.406	D$_{4h}$ 19.922	D$_{4h}$ 36.477	C$_{2v}$ 119.289
C$_{4v}$ 62.105	D$_{4h}$ 3.872	D$_{4h}$ 29.454	C$_{2v}$ 16.050
D$_{4h}$ 0	C$_{4v}$ 0	C$_{4v}$ 0	C$_s$ 0

Even though the ordering of the relative energies of the spin patterns don't completely match between the EH calculations of $Gd_6C_2I_{12}(OPH_3)^-$ and the DFT calculations of $Gd_6C_2I_{12}(IH)^-$, a couple of trends are observed. There is stronger coupling between the Gd spins when there is an unpaired electron delocalized in Gd-Gd bonding orbitals. This is evident from the comparison of the relative energies of the selected spin patterns of the -2 anions vs. the -1 and -3 anions. The range of energies spanned for the patterns of the -2 molecule was 415 cm^{-1} where as the range for the -1 and -3 molecules were 4,181 cm^{-1} (5,318 cm^{-1} DFT) and 3,964 cm^{-1} respectively. Even though the total range of energies spanned by the -1 molecule differed by about 1,000 cm^{-1} between the DFT and EH calculations they are still an order of magnitude bigger than the range of energies spanned by the -2 molecule.

With odd electron counts, the basal Gd spins are much more strongly coupled than the axial Gd spins. The cost of flipping the spins of one of the basal Gd atoms from the completely ferromagnetic configuration for the -1 and -3 anions was calculated to be 846 cm^{-1} (1091 cm^{-1} DFT) and 386 cm^{-1} respectively. To flip an axial Gd spin it costs 62 cm^{-1} (favored by 37 cm^{-1} DFT) for the -1 anion and is favored by 20 cm^{-1} for the -3 anion.

As we've seen, for the cluster monoanion the EH and DFT results are quite similar in broad terms. As we have indicated, that is because the unpaired electron in the b_{1g} orbital dominates the $5d$-mediated exchange between the $4f$ moments – intraatomic $5d$-$4f$ spin alignment is paramount and both the DFT calculations and our spin-polarized EH model simulations capture that effect. However, when the coupling is weaker – as between the axial and basal Gd moments, we see some disagreement between the two treatments. We might generally be inclined to defer to the results of the first-principles

DFT method in such a case, but in this instance it is not clear which approach should yield better results. The exchange potential induced by various lower symmetry spin patterns will correspondingly possess those lower symmetries. As we have explained in previous studies,[26,44,95] understanding finer splitting seen in Table 5.5 thus requires an analysis of the specific second-order orbital mixings induced by any specified spin pattern. The EH results presumably rely on less accurate orbital splittings, but in this case the DFT molecular model results are plagued by low-lying spurious orbitals that are not present in either the band structure calculations of the real system under investigation or in the EH calculations. Lacking experimental magnetic data on *truly isolated clusters*, there seems to be insufficient motivation to settle this problem however and we shall defer the issue to future investigations.

The relative energies of these spin patterns suggest that the magnetic susceptibilities of compounds that contain -1 and -3 charged $Gd_6C_2I_{12}$ clusters should reflect strong coupling between the basal plane Gd atoms and exhibit weak coupling between axial Gd atoms. The magnetic susceptibility of compounds containing -2 charged $Gd_6C_2I_{12}$ clusters should reflect weak coupling between the spins of the electrons in the $4f$ orbitals of Gd.

Conclusions

The structural properties of the compounds reported here have led to the discovery of structural trends and complicated solutions. Hexanuclear Gd compounds tend to incorporate C_2 interstitials rather than single carbon atoms. C_2 centered Gd clusters form similar structure types as mono atom centered rare earth clusters, however, the clusters distort to accommodate the diatomic interstitial. When the C_2 centered Gd

clusters crystallize in a structure type where the parent is mono atom centered and has $\bar{3}$ symmetry, the distortion of the C_2 centered clusters tend to be disordered in the crystal.

The magnetic properties of these compounds were explored via magnetic susceptibility measurements and electronic structure calculations. The magnetic susceptibility data collected on $Cs(Gd_6C_2I_{12})$ indicates the μ_{eff} on a per cluster basis is larger than isolated paramagnetic Gd atoms but not as large as four basal Gd atoms ferromagnetically coupled. The DFT and EH electronic structure calculations suggest that the frontier orbitals of the compounds reported have primarily basal Gd-Gd bonding character. The relative energies of the spin patterns calculated using EH, suggests that $Cs(Gd_6C_2I_{12})$ and $Gd(Gd_6C_2I_{12})$ should have stronger ferromagnetic coupling between the basal Gd atoms than $CsGd(Gd_6C_2I_{12})_2$ because of unpaired electrons in the frontier orbitals.

While $CsGd_6C_2I_{12}$ was able to be made cleanly, $Gd_6C_2I_{11}$, $Gd(Gd_6C_2I_{12})$ and $CsGd(Gd_6C_2I_{12})_2$ were not. $Gd_6C_2I_{11}$ and $Gd(Gd_6C_2I_{12})$ could be made in about 90% yields (based on powder patterns), however, attempts to make these products in pure enough yields for SQUID measurements were unsuccessful. Reaction conditions that yield more than a several crystal yield of $CsGd(Gd_6C_2I_{12})_2$ has not yet been found.

CHAPTER VI

CONCLUSIONS

Two new structure types, $(CsR(R_6CoI_{12})_2$ (R=Er, Gd) and $(CeI)_{0.26}(Ce_6MnI_9))$, were added to the 14 known structure types that contain transition metal centered RE_6 iodide clusters. The known structure types are differentiated by the arrangement of clusters cross-linked by iodide bridges in only 8 different ways (I^{i-i}, I^{a-a}, I^{i-a}, I^{a-i}, I^{a-a-i}, I^{i-a-a}, I^a and I^i). $CsR(R_6CoI_{12})_2$ can be described as an intergrowth of two known compounds $Gd(Gd_6CoI_{12})$ and $Cs(Er_6CI_{12})$. $(CeI)_{0.26}(CeMnI_9)$ is a unique structure type with tight I^{i-i} cross-linking in one plane and I^{i-a}, I^{a-i} bridges connecting the tight cross-linking planes. These two structure types were the result of extensive synthetic exploration on the system $A_xR_6MI_{12+y}$ (A= alkali metal or Ca; R= Gd, Er, Ce; M= Mn, Fe, Co). This system was explored by targeting clusters with a 15-18 e^- count.

From the magnetic susceptibility measurements of the series of transition metal centered Ln_6 compounds ($Gd(Gd_6MI_{12})$ M = Mn, Fe, Co and $CsGd(Gd_6CoI_{12})_2$) a mechanism was suggested for how the spins of the electrons in the $4f$ orbitals of Gd atoms with in a cluster can couple. Coupling the electrons in $4f$ orbitals of neighboring Gd atoms requires unpaired electrons in Gd-Gd bonding orbitals. This was demonstrated by the larger magnetic moment per cluster for $Gd(Gd_6MnI_{12})$, $Gd(Gd_6FeI_{12})$ and $CsGd(Gd_6CoI_{12})_2$ compared to $Gd(Gd_6CoI_{12})$ which has a closed shell configuration for the occupied Gd-Gd bonding orbitals.

Four new carbon centered Gd clusters were discovered, $Gd_6C_2I_{11}$, $Gd(Gd_6C_2I_{12})$, $CsGd(Gd_6C_2I_{12})_2$ and $Cs(Gd_6C_2I_{12})$. Initially the discovery of dicarbide centered Gd clusters was a surprise since there appeared to be evidence, although unpublished,[61] that a single carbon centered $Gd(Gd_6CI_{12})$ could be made. Previously bioctahedral Gd

clusters centered by dicarbide units were known.[98-104] Attempts to rationalize the formation of dicarbide centered clusters or single carbon centered clusters using atomic radii break down when we look at the known structures. While the larger rare earths like La, Ce and Pr form dicarbide centered clusters and the smaller rare earths Er and Lu form single carbon centered clusters, Sc, the smallest rare earth, forms both types of clusters ($Sc(Sc_6CI_{12})^{46}$ and $(Sc_6C_2I_{11})^{36}$).

$Cs(Gd_6C_2I_{12})$ has been made in quantitative yields so that magnetic measurements could be performed. $Gd(Gd_6C_2I_{12})$ and $Gd_6C_2I_{11}$ could be made in about 90% yield and free of other cluster compounds according to x-ray powder diffraction. $CsGd(Gd_6C_2I_{12})_2$ has been a challenge to make without making $Cs(Gd_6C_2I_{12})$ and $Cs(Gd_{10}C_4I_{18})$ as side products.

The magnetic susceptibility data of $Cs(Gd_6C_2I_{12})$ suggests that there is magnetic coupling between Gd atoms but not as much as expected if all 6 (or even 4) Gd atoms per cluster were ferromagnetically coupled and void of intercluster interactions. Based on the electronic structure calculations there should be stronger ferromagnetic coupling between the basal Gd atoms of the clusters and very weak coupling with the axial Gd atoms for clusters that have unpaired electrons in Gd bonding orbitals. The EH calculations on the molecular models of $Gd_6C_2I_{12}(OPH_3)_6^{n-}$ suggest that $Gd(Gd_6C_2I_{12})$ and $Cs(Gd_6C_2I_{12})$ should have stronger intracluster ferromagnetic coupling than $CsGd(Gd_6C_2I_{12})_2$ because of unpaired electrons in Gd-Gd bonding orbitals.

One of the goals in this area of transition metal centered Gd_6 clusters that has yet to be achieved is making and measuring the magnetic properties of a 15 e^- Gd_6M cluster. A 15 e^- cluster would have a half filled symmetric HOMO that might result in a larger degree of coupling within the cluster. Attempts to make a 15 e^- cluster consisted of

targeting $CaGd_6MnI_{12}$. Unfortunately evidence of only partial substitution of Ca in the noncluster Gd^{3+} site was obtained.

The structural distortion of the Gd_6 cluster of the dicarbide units might be beneficial for making magnetically anisotropic clusters. While Gd_6 clusters will not be candidates for magnetically anisotropic clusters because their lack of spin-orbit coupling, a Tb analog of these compounds might be more likely to exhibit properties of magnetic anisotropy than the transition metal centered clusters. Tb has a similar ionic radius to Gd (Tb^{3+} 9 coordinate, ionic radius = 1.095Å; Gd^{3+} 9 coordinate, ionic radius = 1.107 Å),[78] so it might form these dicarbide centered cluster also. Since there are two different Gd sites per cluster (basal and apical), a lanthanide atom of a different size might prefer to occupy one of the two sites. Mixed lanthanide clusters might result in magnetically anisotropic clusters and/or new structure types.

Isolating clusters either by dissolving them into solution or by decreasing the cross-linking between clusters will help disentangle the contribution of the inter- and intracluster coupling contributions to the magnetic susceptibility. Many attempts to decrease the number of intercluster iodine bridges by adding alkali metal iodide salts were unsuccessful. The use of ionic liquids to try to dissolve the clusters may be a better option for isolating clusters. The dicarbide centered cluster compounds might be more easily excised into individual cluster units than transition metal centered clusters based on what has been done with Zr cluster compounds.[57-59] The $Gd–I^a$ distances in the dicarbide centered clusters range from 3.332–3.516 Å for $Gd^b–I^a$ and 3.033–3.260 Å for $Gd^a–I^a$. The $Gd–I^a$ distance for $Gd(Gd_6CoI_{12})$ is 3.3041(8) Å. The longer the $Gd-I^a$ distance the more likely the $Gd–I^a$ bond could be broken in order to dissolve the clusters. If these types of clusters could be dissolved their molecular magnetic properties could be probed.

REFERENCES

1. Sessoli, R.; Tsai, H. L.; Schake, A. R.; Wang, S.; Vincent, J. B.; Folting, K.; Gatteschi, D.; Christou, G.; Hendrickson, D. N. *J. Am. Chem. Soc.* **1993**, *115*, 1804-16.

2. Murugesu, M.; Raftery, J.; Wernsdorfer, W.; Christou, G.; Brechin, E. K. *Inorg. Chem.* **2004**, *43*, 4203-4209.

3. Tasiopoulos, A. J.; Vinslava, A.; Werndorfer, W.; Abboud, K. A.; Christou, G. *Angew. Chem., Int. Ed.* **2004**, *43*, 2117-2121.

4. Sanudo, E. C.; Wernsdorfer, W.; Abboud, K. A.; Christou, G. *Inorg. Chem.* **2004**, *43*, 4137-4144.

5. Murugesu, M.; Habrych, M.; Wernsdorfer, W.; Abboud, K. A.; Christou, G. *J. Am. Chem. Soc.* **2004**, *126*, 4766-4767.

6. Oshio, H.; Hoshino, N.; Ito, T.; Nakano, M. *J. Am. Chem. Soc.* **2004**, *126*, 8805-8812.

7. Moragues-Canovas, M.; Helliwell, M.; Ricard, L.; Riviere, E.; Wernsdorfer, W.; Brechin, E.; Mallah, T. *Eur. J. Inorg. Chem.* **2004**, 2219-2222.

8. Takagami, N.; Ishida, T.; Nogami, T. *Bull. Chem. Soc. Jpn.* **2004**, *77*, 1125-1134.

9. Cornia, A.; Fabretti, A. C.; Garrisi, P.; Mortalo, C.; Bonacchi, D.; Sessoli, R.; Sorace, L.; Barra, A. L.; Wernsdorfer, W. *J. Magn. Magn. Mater.* **2004**, *272-276*, E749-E751.

10. Bian, G. Q.; Kuroda-Sowa, T.; Konaka, H.; Hatano, M.; Maekawa, M.; Munakata, M.; Miyasaka, H.; Yamashita, M. *Inorg. Chem.* **2004**, *43*, 4790-4792.

11. Zhao, H.; Berlinguette, C. P.; Bacsa, J.; Prosvirin, A. V.; Bera, J. K.; Tichy, S. E.; Schelter, E. J.; Dunbar, K. R. *Inorg. Chem.* **2004**, *43*, 1359-1369.

12. Schelter, E. J.; Prosvirin, A. V.; Dunbar, K. R. *J. Am. Chem. Soc.* **2004**, *126*, 15004-15005.

13. Ishikawa, N.; Sugita, M.; Ishikawa, T.; Koshihara, S.; Kaizu, Y. *J. Phys. Chem. B* **2004**, *108*, 11265-11271.

14. Ishikawa, N.; Sugita, M.; Okubo, T.; Tanaka, N.; Iino, T.; Kaizu, Y. *Inorg. Chem.* **2003**, *42*, 2440-2446.

15. Ishikawa, N.; Sugita, M.; Wernsdorfer, W. *J. Am. Chem. Soc.* **2005**, *127*, 3650-3651.

16. Ishikawa, N.; Otsuka, S.; Kaizu, Y. *Angew. Chem., Int. Ed.* **2005**, *44*, 731-733.

17. Ishikawa, N.; Sugita, M.; Tanaka, N.; Ishikawa, T.; Koshihara, S.-Y.; Kaizu, Y. *Inorg. Chem.* **2004**, *43*, 5498-5500.

18. Ishikawa, N.; Tanaka, N.; Kaizu, Y. *Inorg. Chim. Acta* **2004**, *357*, 2181-2184.

19. Ishikawa, N.; Sugita, M.; Ishikawa, T.; Koshihara, S.-Y.; Kaizu, Y. *J. Am. Chem. Soc.* **2003**, *125*, 8694-8695.

20. Takamatsu, S.; Ishikawa, T.; Koshihara, S.-y.; Ishikawa, N. *Inorg. Chem.* **2007**, *46*, 7250-7252.

21. Milios, C. J.; Vinslava, A.; Wernsdorfer, W.; Moggach, S.; Parsons, S.; Perlepes, S. P.; Christou, G.; Brechin, E. K. *J. Am. Chem. Soc.* **2007**, *129*, 2754-2755.

22. De Cian, A.; Moussavi, M.; Fischer, J.; Weiss, R. *Inorg. Chem.* **1985**, *24*, 3162-7.

23. Roy, L. E.; Hughbanks, T. *Mater. Res. Soc. Symp. Proc.* **2002**, *755*, 25-30.

24. Roy, L. E.; Hughbanks, T. *Abstracts of Papers, 226th ACS National Meeting, New York, NY, United States, September 7-11, 2003* **2003**, INOR-626.

25. Hughbanks, T.; Roy, L. E. *Abstracts of Papers, 226th ACS National Meeting, New York, NY, United States, September 7-11, 2003* **2003**, INOR-374.

26. Roy, L.; Hughbanks, T. *J. Solid State Chem.* **2003**, *176*, 294-305.

27. Martin, W. C.; Zalubas, R.; Hagan, L. *Atomic Energy Levels-The Rare-Earth Elements. The Spectra of Lanthanum, Cerium, Praseodymium, Neodymium, Promethium, Samarium, Europium, Gadolinium, Terbium, Dysprosium, Holmium, Erbium, Thulium, Ytterbium, and Lutetium*; National Bureau of Standards: Washington D.C., 1978; Vol. 60.

28. Schaefer, H.; Schnering, H. G. *Angew. Chem.* **1964**, *76*, 833-49.

29. Lulei, M.; Martin, J. D.; Corbett, J. D. *J. Solid State Chem.* **1996**, *125*, 249-254.

30. Park, Y.; Corbett, J. D. *Inorg. Chem.* **1994**, *33*, 1705-8.

31. Payne, M. W.; Corbett, J. D. *Inorg. Chem.* **1990**, *29*, 2246-51.

32.   Hughbanks, T.; Corbett, J. D. *Inorg. Chem.* **1989**, *28*, 631-5.

33.   Llusar, R.; Corbett, J. D. *Inorg. Chem.* **1994**, *33*, 849-53.

34.   Mattausch, H.; Hoch, C.; Simon, A. *Z. Anorg. Allg. Chem.* **2005**, *631*, 1423-1429.

35.   Lulei, M.; Corbett, J. D. *Z. Anorg. Allg. Chem.* **1996**, *622*, 1677-1684.

36.   Dudis, D. S.; Corbett, J. D. *Inorg. Chem.* **1987**, *26*, 1933-40.

37.   Jensen, E. A.; Corbett, J. D. *Inorg. Chem.* **2002**, *41*, 6199-6205.

38.   Hughbanks, T.; Corbett, J. D. *Inorg. Chem.* **1988**, *27*, 2022-6.

39.   Uma, S.; Corbett, J. D. *J. Solid State Chem.* **2001**, *161*, 161-165.

40.   Jensen, E. A.; Corbett, J. D. *J. Solid State Chem.* **2003**, *172*, 132-137.

41.   Palasyuk, A.; Pantenburg, I.; Meyer, G. *Z. Anorg. Allg. Chem.* **2006**, *632*, 1969-1971.

42.   Palasyuk, A.; Pantenburg, I.; Meyer, G. *Acta Crystallographica* **2006**, *E62*, i61-i63.

43.   Hughbanks, T.; Rosenthal, G.; Corbett, J. D. *J. Am. Chem. Soc.* **1986**, *108*, 8289-90.

44.   Sweet, L. E.; Roy, L. E.; Meng, F.; Hughbanks, T. *J. Am. Chem. Soc.* **2006**, *128*, 10193-10201.

45.   Simon, A.; Mattausch, H. J.; Miller, G. J.; Bauhofer, W.; Kremer, R. K.; Gschneidner, K. A.; Eyring, L. In *Handbook on the Physics and Chemistry of Rare Earths*; Elsevier: Amsterdam, 1991; Vol. 15, p 191-285.

46.   Dudis, D. S.; Corbett, J. D.; Hwu, S. J. *Inorg. Chem.* **1986**, *25*, 3434-8.

47.   Lukachuk, M.; Kienle, L.; Zheng, C.; Mattausch, H.; Simon, A. *Inorg. Chem.* **2008**, *47*, 4656-4660.

48.   Wiglusz, R.; Pantenburg, I.; Meyer, G. *Z. Anorg. Allg. Chem.* **2007**, *633*, 1317-1319.

49.   Artelt, H. M.; Schleid, T.; Meyer, G. *Z. Anorg. Allg. Chem.* **1992**, *618*, 18-25.

50.   Artelt, H. M.; Meyer, G. *J. Chem. Soc., Chem. Commun.* **1992**, *18*, 1320-1.

51.   Uma, S.; Corbett, J. D. *Inorg. Chem.* **1998**, *37*, 1944-1948.

52.   Artelt, H. M.; Meyer, G. *Z. Anorg. Allg. Chem.* **1993**, *619*, 1-6.

53.   Lulei, M.; Corbett, J. D. *Inorg. Chem.* **1996**, *35*, 4084-4086.

54.   Artelt, H. M.; Schleid, T.; Meyer, G. *Z. Anorg. Allg. Chem.* **1994**, *620*, 1521-6.

55.   Uma, S.; Corbett, J. D. *Inorg. Chem.* **1999**, *38*, 3831-3835.

56.   Uma, S.; Martin, J. D.; Corbett, J. D. *Inorg. Chem.* **1999**, *38*, 3825-3830.

57.   Runyan, C. E., Jr.; Hughbanks, T. *J. Am. Chem. Soc.* **1994**, *116*, 7909-10.

58.   Cotton, F. A.; Hughbanks, T.; Runyan, C. E., Jr.; Wojtczak, W. A. In *Early Transition Metal Clusters with p-Donor Ligands*; Chisholm, M. H., Ed.; VCH Publishers: New York, 1995, p 1-26.

59.   Xie, X.; Jones, J. N.; Hughbanks, T. *Inorg. Chem.* **2001**, *40*, 522-527.

60.   Berroth, K., Max-Planck-Institut, Stuttgart, 1980.

61.   Warkentin, E.; Berroth, K.; Simon, A. *unpublished result* **1981**.

62.   Corbett, J. D. *Inorg. Synth.* **1983**, *22*, 31-6.

63.   Corbett, J. D. *Inorg. Synth.* **1983**, *22*, 15-22.

64.   Kraus, W.; Nolze, G., *Powder Cell-V2.4, Program for viewing powder patterns*; Federal Institute for Materials Research and Testing: Berlin, Germany, 2000.

65.   *CrystalDiffract-V5.1.7, Program for viewing powder patterns*; CrystalMaker Software Ltd.: Oxfordshire, UK, 2008.

66.   Karlsruhe, F. F. *Inorganic Crystal Structure Database (ICSD)*, 2007, http://icsdweb.fiz-karlsruhe.de.

67.   *SMART-V5.625, Program for data collection on area detectors*; Bruker AXS Inc.: Madison, WI, 2001.

68.   *Apex2-V2.1-4, Program used to interface with an Bruker Apex diffractameter in addition to a variety of other data processing functions*; Bruker AXS Inc.: Madison, WI, 2007

69.   *SAINT-V6.63, Program for reduction of area detector data*; Bruker AXS Inc.: Madison, WI, 2001.

70. Sheldrick, G. M., *SADABS-V2.03, Program for absorption correction of area detector frames*; Bruker AXS Inc.: Madison, WI, 2001.

71. *SHELXTL-V6.12(PC-version)*, *Program for structure solution, refinement and presentation*; Bruker AXS Inc.: Madison, WI, 2000.

72. Sheldrick, G., *SHELXL-97, Program for crystal structure refinement*; Gottingen, Germany, 1997.

73. Funding for the Quantum Design SQUID magnetometer MPMSXL provided by the National Science Foundation (NSF-9974899).

74. Kahn, O. *Molecular magnetism*; VCH, New York, N. Y., 1993.

75. *GEMINI-V1.02*, *Program for twin deconvolution*; Bruker AXS Inc.: Madison, WI, 2000.

76. Sheldrick, G. M., *CELLNOW, Program for unit cell determination*; Institüt für Anorganische Chemie der Universität: Göttingen, Germany, 2003.

77. Spek, A. L. *J. Appl. Crystallogr.* **2003**, *36*, 7-13.

78. Shannon, R. D. *Acta Cryst.* **1976**, *A 32*, 751-767.

79. The following restraint was used in SHELX to refine the occupancy of the cavity: Occupancy of CeI units in cavity = x(1/6 this site multiplicity of the (Ce) general position) = x(the site multiplicity of the (I) central position); site multiplicity of the general position = 6, site multiplicity of the central position = 1.

80. Martin, W. C.; Zalubas, R.; Hagan, L. *Natl. Stand. Ref. Data Ser., Natl. Bur. Stand.* **1978**, *60*.

81. Hwu, S. J.; Corbett, J. D. *J. Solid State Chem.* **1986**, *64*, 331-46.

82. Sweet, L. E.; Hughbanks, T. *Inorg. Chem.* **2006**, *45*, 9696-9702.

83. Pauling, L. *J. Am. Chem. Soc.* **1947**, *69*, 542-553.

84. Dudis, D. S.; Corbett, J. D.; Hwu, S. J. *Inorg. Chem.* **1986**, *25*, 3434-3438.

85. Sweet, L. E.; Roy, L. E.; Meng, F.; Hughbanks, T. *J. Am. Chem. Soc.* **2006**, *128*, 10193-10201 Electronic structure calculations performed by Dr. Lindsay Roy.

86. *Cerius2-V4.10*, *A program for modeling compounds*; Accelrys Softwar Inc.: San Diego, CA, 2005.

87. Delley, B. *J. Chem. Phys.* **2000**, *113*, 7756-7764.

88. Delley, B. *Comput. Mater. Sci.* **2000**, *17*, 122-126.

89. Delley, B. *J. Chem. Phys.* **1990**, *92*, 508-517.

90. Becke, A. D. *Physical Review A* **1988**, *38*, 3098.

91. Lee, C.; Yang, W.; Parr, R. G. *Physical Review B* **1988**, *37*, 785.

92. Miehlich, B.; Savin, A.; Stoll, H.; Preuss, H. *Chem. Phys. Lett.* **1989**, *157*, 200-206.

93. Delley, B. *Int. J. Quantum Chem.* **1998**, *69*, 423-433.

94. Landrum, G. A., *YAeHMOP: Yet another extended huckel molecular orbital package-3.0.3;* 2004. Available on the web at: http://yaehmop.sourceforge.net/.

95. Roy, L. E.; Hughbanks, T. *J. Phys. Chem. B* **2006**, *110*, 20290-20296.

96. Cotton, S.; McCleverty, J. A.; Meyer, T. J. In *Comprehensive Coordination Chemistry II*; Pergamon: Oxford, 2003, p 93-188.

97. Sweet, L. E.; Hughbanks, T. *unpublished result* **2008**, Cs(Gd10C4I18) is isotypic to compounds that have been previously reported: Hinz, D. J.; Meyer, G. *Zeitschrift fur Kristallographie* **1995**, 210, 958-958., Uhrlandt, S.; Artelt, H. M.; Meyer, G. *Z. Anorg. Allg. Chem.* **1994**, 620, 1532-6. and Artelt, H. M.; Meyer, G. *J. Chem. Soc., Chem. Commun.* **1992**, 1320-1.

98. Hinz, D. J.; Meyer, G. *Zeitschrift fur Kristallographie* **1995**, *210*, 958-958.

99. Artelt, H. M.; Meyer, G. *Z. Anorg. Allg. Chem.* **1994**, *620*, 1527-31.

100. Liess, H.; Steffen, F.; Meyer, G. *J. Alloys Compd.* **1997**, *246*, 242-247.

101. Uhrlandt, S.; Artelt, H. M.; Meyer, G. *Z. Anorg. Allg. Chem.* **1994**, *620*, 1532-6.

102. Hinz, D. J.; Meyer, G. *Zeitschrift fur Kristallographie* **1995**, *210*, 957-957.

103. Warkentin, E.; Masse, R.; Simon, A. *Z. Anorg. Allg. Chem.* **1982**, *491*, 323-36.

104. Mattausch, H.; Warkentin, E.; Oeckler, O.; Simon, A. *Z. Anorg. Allg. Chem.* **2000**, *626*, 2117-2124.

VITA

Name: Lucas Edward Sweet

Address: Department of Chemistry
                Texas A&M University
                P.O. Box 30012
                College Station, TX 77842-3012

Education: B.A., Chemistry, Lake Forest College, 2002

Publications: Sweet, L. E.; Roy, L. E.; Meng, F.; Hughbanks, T. *J. Am. Chem. Soc.* **2006**, *128*, 10193-10201

                Sweet, L. E.; Hughbanks, T. *Inorg. Chem.* **2006**, *45*, 9696-9702.

                Dunn, A. R.; Sweet, L. E., Wiser, D. C.; LoCoco, M. D.; Jordan, R. F. *Organometallics* **2004**; 23(24); 5671-5680